MULTIMODE OPTOMECHANICAL SYSTEMS AND PHONONIC NETWORKS

by

MARK CHRISTOPHER KUZYK

A DISSERTATION

Presented to the Department of Physics
and the Graduate School of the University of Oregon
in partial fulfillment of the requirements
for the degree of
Doctor of Philosophy

September 2018

DISSERTATION APPROVAL PAGE

Student: Mark Christopher Kuzyk

Title: Multimode Optomechanical Systems and Phononic Networks

This dissertation has been accepted and approved in partial fulfillment of the requirements for the Doctor of Philosophy degree in the Department of Physics by:

Steven van Enk	Chair
Hailin Wang	Advisor
Benjamin McMorran	Core Member
Mark Lonergan	Institutional Representative

and

Janet Woodruff-Borden	Vice Provost and Dean of the Graduate School

Original approval signatures are on file with the University of Oregon Graduate School.

Degree awarded September 2018

DISSERTATION ABSTRACT

Mark Christopher Kuzyk

Doctor of Philosophy

Department of Physics

September 2018

Title: Multimode Optomechanical Systems and Phononic Networks

An optomechanical system consists of an optical cavity mode coupled to a mode of a mechanical oscillator. Depending on the configuration of the system, the optomechanical interaction can be used to drive or cool the mechanical mode, coherently swap the optical and mechanical states, or create entanglement.

A multimode optomechanical system consists of many optical (mechanical) modes coupled to a mechanical (optical) mode. With the tools of the optomechanical interaction, multimode optomechanical systems provide a rich platform to study new physics and technologies. A central challenge in optomechanical systems is to mitigate the effects of the thermal environment, which remains significant even at cryogenic temperatures, for mechanical oscillators typically used in optomechanical systems. The central theme of this thesis is to study how the properties of multimode optomechanical systems can be used for such mitigation of thermal noise.

The most straightforward extension of an optomechanical system to a multimode system is to have a single optical mode couple to two mechanical modes, or a single mechanical mode couple to two optical modes. In this thesis, we study both types

of multimode system. In each case, we study the formation of a dark mode, an eigenstate of the three-mode system that is of particular interest. When the system is in a dark state, the two modes of similar character (optical or mechanical) interact with each other through the mode of dissimilar character, but due to interference, the interaction becomes decoupled from the properties of the dissimilar mode.

Another interesting application of the three-mode system is two-mode optical entanglement, generated through mechanical motion. Such entanglement tends to be sensitive to thermal noise. We propose a new method for generating two-mode optical entanglement in the three-mode system that is robust against the thermal environment of the mechanical mode.

Finally, we propose a novel, scalable architecture for a quantum computer. The architecture makes use of the concepts developed earlier in the thesis, and applies them to a system that on the surface looks quite different from the standard optomechanical system, but is formally equivalent.

This dissertation includes previously published and unpublished coauthored material.

CURRICULUM VITAE

NAME OF AUTHOR: Mark Christopher Kuzyk

GRADUATE AND UNDERGRADUATE SCHOOLS ATTENDED:
University of Oregon, Eugene, OR
Washington State University, Pullman, WA

DEGREES AWARDED:
Doctor of Philosophy in Physics, 2018, University of Oregon
Bachelor of Science in Physics, 2009, Washington State University

AREAS OF SPECIAL INTEREST:
Optics, Quantum Optics, Optomechanics, Phononics

PROFESSIONAL EXPERIENCE:

Research Assistant, Hailin Wang, Department of Physics, University of Oregon, 2009 - present

Summer Undergraduate Research Fellow, Ivan Biaggio, Lehigh University, 2008

GRANTS, AWARDS AND HONORS:

Optical Society of America Technical Poster Award, CLEO, 2017

Weiser Sr Teaching Assistant Award, 2016

Marthe E. Smith Memorial Science Scholarship, 2014

PUBLICATIONS:

Mark C Kuzyk and Hailin Wang. Phononic quantum networks of solid-state spins with alternating and frequency-selective waveguides. *arXiv preprint arXiv:1804.07862*, 2018.

Mark C Kuzyk and Hailin Wang. Controlling multimode optomechanical interactions via interference. *Physical Review A*, 96(2):023860, 2017.

Xuefeng Jiang, Min Wang, Mark C Kuzyk, Thein Oo, Gui-Lu Long, and Hailin Wang. Chip-based silica microspheres for cavity optomechanics. *Optics express*, 23(21):27260–27265, 2015.

JunHwan Kim, Mark C Kuzyk, Kewen Han, Hailin Wang, and Gaurav Bahl. Non-reciprocal brillouin scattering induced transparency. *Nature Physics*, 11(3):275, 2015.

Chunhua Dong, Victor Fiore, Mark C Kuzyk, Lin Tian, and Hailin Wang. Optical wavelength conversion via optomechanical coupling in a silica resonator. *Annalen der Physik*, 527(1-2):100–106, 2015.

Chunhua Dong, Victor Fiore, Mark C Kuzyk, and Hailin Wang. Transient optomechanically induced transparency in a silica microsphere. *Physical Review A*, 87(5):055802, 2013.

Victor Fiore, Chunhua Dong, Mark C Kuzyk, and Hailin Wang. Optomechanical light storage in a silica microresonator. *Physical Review A*, 87(2):023812, 2013.

Mark C Kuzyk, Steven J van Enk, and Hailin Wang. Generating robust optical entanglement in weak-coupling optomechanical systems. *Physical Review A*, 88(6):062341, 2013.

Chunhua Dong, Victor Fiore, Mark C Kuzyk, and Hailin Wang. Optomechanical dark mode. *Science*, 338(6114):1609–1613, 2012.

Victor Fiore, Yong Yang, Mark C Kuzyk, Russell Barbour, Lin Tian, and Hailin Wang. Storing optical information as a mechanical excitation in a silica optomechanical resonator. *Physical review letters*, 107(13):133601, 2011.

Brian B Frank, Philip R Laporta, Benjamin Breiten, Mark C Kuzyk, Peter D Jarowski, W Bernd Schweizer, Paul Seiler, Ivan Biaggio, Corinne Boudon, Jean-Paul Gisselbrecht, et al. Comparison of cc triple and double bonds as spacers in push–pull chromophores. *European journal of organic chemistry*, 2011(23):4307–4317, 2011.

Shoresh Shafei, Mark C Kuzyk, and Mark G Kuzyk. Monte carlo studies of the intrinsic second hyperpolarizability. *JOSA B*, 27(9):1849–1856, 2010.

Mark C Kuzyk and Mark G Kuzyk. Monte carlo studies of the fundamental limits of the intrinsic hyperpolarizability. *JOSA B*, 25(1):103–110, 2008.

ACKNOWLEDGEMENTS

I would like to thank my advisor, Hailin Wang, for all that he has done for me. He always sets a high bar, and provides the necessary support to ensure my success. I'm also grateful to Dan Steck and Steven van Enk for valuable discussions. In just a few encounters that they probably don't remember, I've learned a great deal.

I've had the pleasure of working with many great labmates. I'm especially grateful to Tom Baldwin for his guidance in using Python in the lab, a gift that keeps on giving, to Nima Dinyari, who took time away from his dissertation writing to help me get started in the lab, and to Thein Oo, who was always more than willing to take time away from his own work to give me a hand.

Graduate school would not have been nearly as enjoyable or interesting without Chuck Warren and Peter Radloff.

Finally, I would like to express my deepest gratitude to my parents. Mom, I know everyone thinks their parents are great, but I genuinely believe your compassion and empathy are unmatched. I will always try to follow your example. Dad, you're not so bad either. You're a gifted physicist. The ease with which you provide deep insights into new problems and approach them in original ways still catches me off guard. I cherish our discussions, and look forward to many more.

DEDICATION

For Jack Conboy, whose desire to learn lives on in his daughter, and for Walter Kuzyk.

TABLE OF CONTENTS

LIST OF FIGURES

Figure Page

Figure Page

CHAPTER I

INTRODUCTION

In the last few years, the field of optomechanics has matured. The major milestones for optomechanical systems have been achieved. Several experimental architectures are now capable of probing the quantum regime of macroscopic oscillators, where the probability of preparing the oscillator in its ground state exceeds 80% [1, 2, 3]. The implementation of phononic crystal oscillators has become main stream. State-of-the-art devices have Q-factors that exceed 10^9 [1], and can undergo more than a thousand coherent oscillations at a few Kelvin before the oscillator experiences a single thermal kick. Measuring quantum correlations [4, 5], squeezing [6], and entanglement [7] in such systems is now possible.

On the horizon are multimode and hybrid optomechanical systems. In multimode optomechanical systems, multiple optical (mechanical) modes interact with a given mechanical (optical) mode. These multimode systems can provide a versatile experimental platform for a rich variety of physical phenomena, such as exceptional points and topological energy transfer [8], backaction evasion [9, 10], two-mode squeezing [11, 12], and optical or mechanical state transfer [13, 14, 15, 16, 17, 18, 19, 20, 21, 22].

Hybrid systems are made by incororating another quantum system into the basic optomechanical system. For example, solid-state-based quantum systems, like crystal lattice defects, can interact with vibrational modes through strain. Embedding such a defect into the mechanical component of an optomechanical system can provide a route for the defect to interact with an optical cavity mode through a shared coupling to the mechanical mode. In a multimode hybrid system, a quantum state can be

mapped from the defect to the optical cavity mode, and then through multimode optomechanics, the cavity mode can be converted to a wavelength suitable for long-distance communictation.

Hybrid systems can be interconnected to form networks, providing a potential route towards scalable quantum computers. One of the key challenges in hybrid and multimode quantum systems is to mitigate the deleterious effects of the environment on the fragile quantum states that are to be shuttled between the components of the network. In particular, the effects of the thermal environment are significant, even at cryogenic temperatures, for realistic mechanical oscillators which operate at sub-gigahertz frequencies.

Fortunately, multimode optomechanical systems provide ways for us to mitigate thermal effects. Interference in the multimode system, when arranged appropriately, can cancel out the effects of thermal noise. Systems in this configuration are said to be in a dark state, a recurring theme in our work. Another way to abate the effects of the thermal environment for coupled oscillators is to design the system in such a way that the thermally noisy component oscillates in conjunction with the completion of the desired operation. Such arrangements have a stroboscopic quality, where the system of interest sees the environment as stationary at the begining and end of the operation.

The use of dark modes and stroboscopic system evolution are the major topics of this thesis. To discuss them in a meaningful way in the context of multimode optomechanical systems requires a working knowledge of the basic linearized optomechanical system.

1.1. Linearized Optomechanical Systems

The canonical optomechanical system is a Fábrey Perot optical cavity with the end mirror connected to a spring, thus free to undergo simple harmonic motion. The intrinsic optomechanical coupling rate, denoted g_0, gives the frequency shift induced on the optical resonance frequency of the cavity when the end mirror undergoes zero-point fluctuations in its quantum ground state. In all current optomechanical systems, g_0 is small compared to the optical linewidth of the cavity, so the optomechanical system is unable to resolve such fluctuations. Instead, the optical cavity is driven by a strong laser drive, which leads to an effective optomechanical interaction with a coupling strength proportional to the driving laser power.

The effective optomechanical interaction describes the linear coupling between two harmonic oscillators, namely the optical fluctuations from the driving laser (usually denoted by field operator a), and the mechanical mode (denoted by field operator b). When the mechanical mode frequency ω_m is much greater than the optical linewidth (a situation known as the resolved sideband regime), the effective interaction between the mechanical and optical modes can be controlled by the detuning of the laser (summarized in Figure 1.1). When the laser is detuned near the red sideband ($\Delta \approx -\omega_m$), the interaction is approximately that of a beam-splitter. The process is akin to anti-Stokes scattering, where photons from the drive laser scatter to higher frequency at the expense of a quantum of the mechanical mode energy. This generation of the higher frequency photon at the expense of a mechanical quantum is a "state transfer" between the mechanical and optical mode. When the laser is detuned on or near the blue sideband ($\Delta \approx \omega_m$), the interaction behaves like a parametric down conversion through Stokes scattering. The drive laser can decay into an entangled photon-phonon pair.

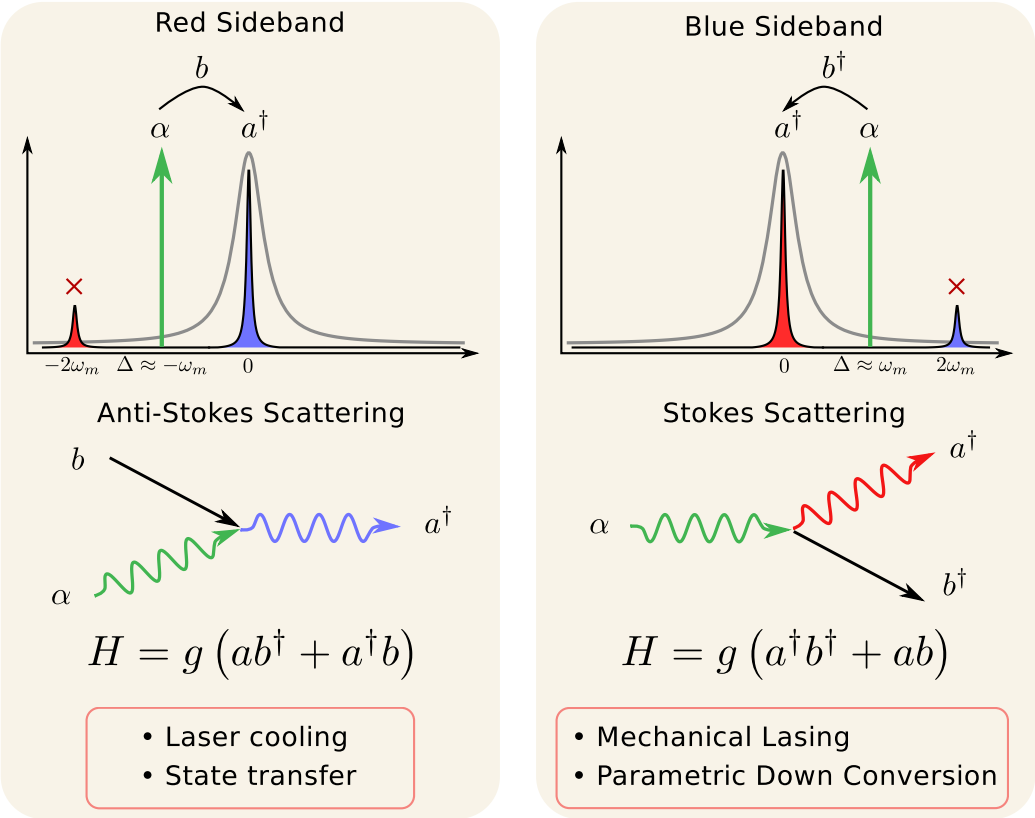

FIGURE 1.1. The linearized optomechanics toolbox. The left panel describes the interaction between the optical and mechanical mode when the laser is detuned near the red sideband, where the interaction Hamiltonian is effectively that of a beam-splitter. The interaction can be viewed as anti-Stokes scattering of the drive laser. The right panel shows the physics of blue sideband driving, which generates a parametric down conversion process. The interaction can be viewed as Stokes scattering of the drive laser.

The beam-splitter interaction of a red-sideband driven optomechanical system, and the parametric down conversion process of the blue-sideband, are the basic tools in the optomechanics toolbox. In multimode systems, the Stokes and anti-Stokes processes can be chained together in interesting ways to generate new types of interactions, as discussed in the following section.

To conclude this section, it is worth noting that the canonical system is useful for gaining intuition about the behavior of optomechanical systems. However, most

modern systems, including our own, have little in common with the canonical system (see Figure 1.2 for examples). Nonetheless, each system is accurately described by the linearized Hamiltonian, and can thus be mapped to the canonical system. The stunning diversity of physical architectures that are described by the linearized optomechanical Hamiltonian provide a variety of platforms for cultivating interesting new multimode, hybrid optomechanical systems, and quantum networks.

1.2. Multimode Systems and Networks

The optomechanics toolbox discussed in the previous section can easily be expanded upon in useful ways for multimode systems. In Chapters V and VII, we consider a multimode system where two optical modes couple to a shared mechanical mode. Making use of the optomechanical toolbox, this multimode system can be used to either transfer the optical state from one mode to the next (Chapter V), or to entangle the two optical modes (Chapter VII). To fully understand these processes requires an analysis of the coupled modes, but a brief consideration of the Stokes and anti-Stokes processes is adequate for understanding the net results of the experiments. These multimode processes are summarized in Figure 1.3.

Optomechanical systems can also be hybridized with other quantum systems. For example, Nitrogen vacancy (NV) centers in diamond are defects that behave like a single molecule trapped in the diamond lattice. The spin coherence of the NV center makes it a promising candidate for quantum computation and sensing. The energy level structure of the NV center is sensitive to strain in the lattice, which provides an avenue for coupling NV centers to mechanical motion. An interesting potential hybrid system is comprised of a diamond mechanical oscillator with embedded NV centers, a unit we refer to as a spin-mechanical resonator. A theoretical analysis of

such a unit reveals that it is highly analogous to a trapped ion chain. A series of spin-mechanical resonators can be daisy chained together to form a network, where each unit communicates to its nearest neighbors through vibrational modes. Designing such a network is the focus of Chapter VIII. An optical cavity placed near any node of the network will form an optomechanical transducer. The quantum state of the NV could then be mapped to the mechanical mode of the spin-mechanical resonator, which could in turn be mapped optomechanically into an optical field that can facilitate long-distance communication.

1.3. Thesis Overview

This thesis will present four major projects that involve multimode optomechanical interactions. First, Chapter II reviews the important features of optical and mechanical resonators, before introducing the optomechanical interaction and its relevant consequences. Chapter III discusses the experimental apparatus we use for optomechanics, the fused silica microsphere. In Chapter IV, the measurement techniques we use to carry out optomechanical experiments are reviewed. The remaining chapters present the results of the four projects.

Chapters V and VI both discuss experimental systems that make use of interference through the formation of dark modes - a mechanically dark optical mode in Chapter V, and an optically dark mechanical mode in Chapter VI. Chapters VII and VIII each make use of stroboscopic system evolution to mitigate the effects of a thermal environment. In Chapter VII, the goal is to entangle two optical modes through their interaction with a thermally driven mechanical mode. Chapter VIII is somewhat unique. While it also makes use of stroboscopic system evolution, the work describes a phononic network of spin-mechanical resonators, a deviation from

the typical optomechanical system of the previous chapters. Interestingly enough, however, when the mechanical modes couple to an ensemble of spins, the system looks identical to a red sideband-driven multimode optomechanical system.

Chapter V includes published material from [13], which was coauthored by Chunhua Dong, Victor Fiore, and Hailin Wang. Chapter VI includes published material from [23], coauthored by Hailin Wang. Chapter VII includes published material from [24], coauthored by Steven J. van Enk and Hailin Wang. Finally, chapter VIII includes material that is currently in the review process, and was coauthored by Hailin Wang. The manuscript is currently available through arXiv.org [25].

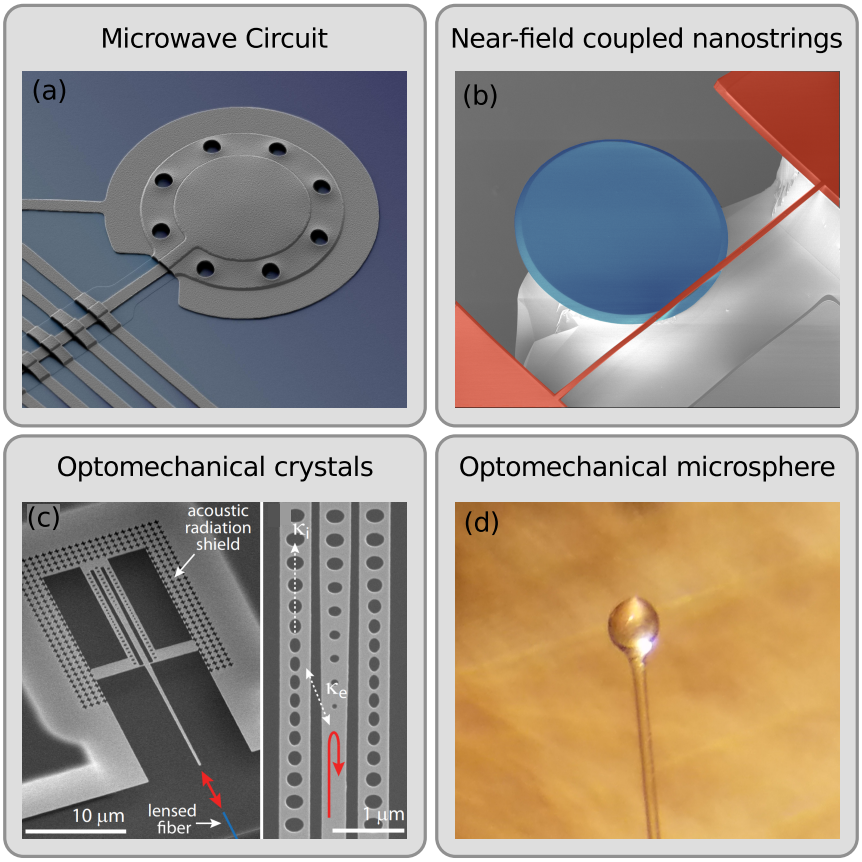

FIGURE 1.2. Examples of optomechanical systems used today, which bear little semblance to the canonical Fábrey Perot system. (a) A microwave LC circuit, where one face of the parallel plate capacitor is a drumhead. (Photo credit: Teufel/NIST `https://www.nist.gov/image/17pml001teufeldrumjpg`) (b) A nanostring mechanical oscillator (red) couples to a microdisk optical resonator (blue) through an evanescent field. (Photo credit: Tobias Kippenberg (c) An `https://www.flickr.com/photos/128145967@N04/15649177090/`) optomechanical crystal device consists of a silicon photonic crystal resonator beam. The beam also supports mechanical modes, which are localized and protected by a phononic crystal surrounding the device. (Photo credit: Oskar Painter `http://copilot.caltech.edu/documents/223-physreva_90_011803.pdf`) (d) A silica microsphere serves as both the optical and mechanical resonator, supporting optical and mechanical whispering gallery modes, as well as mechanical breathing modes.

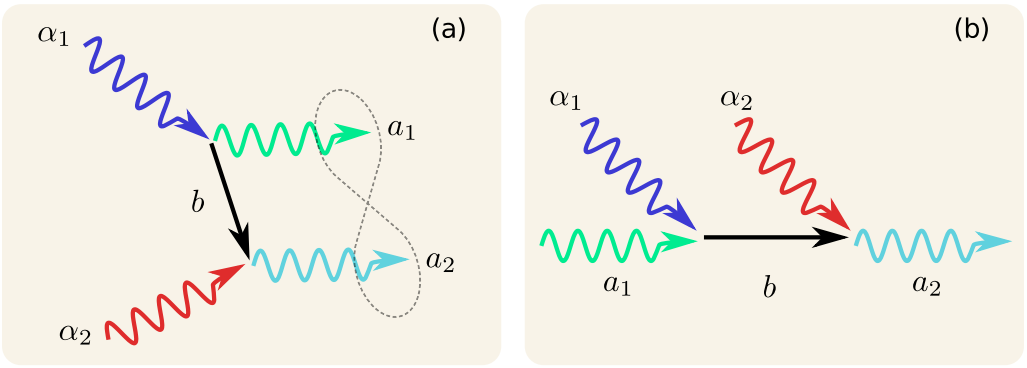

FIGURE 1.3. Multimode entanglement and state transfer (a) Entanglement between optical modes a_1 and a_2. First, a blue sideband pump α_1 undergoes Stokes scattering, producing a phonon (b) and cavity photon (a_1) that are entangled. Then, a red sideband pump α_2 on a second optical mode undergoes anti-Stokes scattering with the phonon, generating a cavity photon (a_2) that is entangled with the cavity photon of mode 1. (b) Photon state transfer. A photon a_1 is injected into the cavity. A red sideband pump (α_1) scatters with the photon to generate a phonon (b). Then, a second red sideband pump (α_2) on mode 2 undergoes anti-Stokes scattering with the phonon, generating a cavity photon in mode 2 in the state of the original injected photon.

CHAPTER II

THEORETICAL BACKGROUND

2.1. Introduction

The optomechanical system is composed of two parts: an optical cavity mode, and a mechanical mode. The mass and length scales of optomechanical systems varies over many orders of magnitude, from LIGO's gram mass and kilometer length scales, to trapped atoms systems with 10^{-21} gram mass scales and microcavities with micrometer length. The experimental architectures also vary immensely, from Fabrey-Pérot resonators with suspended mirrors to photonic and phononic crystal cavities manufactured on Silicon chips. As varied as these systems can be, the essential characteristics of all such systems are an optical cavity mode and a mechanical mode. In this chapter, the important properties of these building blocks are reviewed, before introducing their interaction.

2.2. Optical Resonators

An optical resonator is a device that confines an electromagnetic field. Due to interference, the confined field can only posses specific mode patterns and frequencies.

The simplest optical resonator is a Fabrey-Pérot cavity, consisting of two mirrors that face each other (Fig. 2.1). For perfect mirrors ($r_1 = r_2 = 1$), the field at each mirror must be zero. Imposing these boundary conditions on a cavity of length L gives the condition

$$\omega_n = n\pi c/L, \tag{2.1}$$

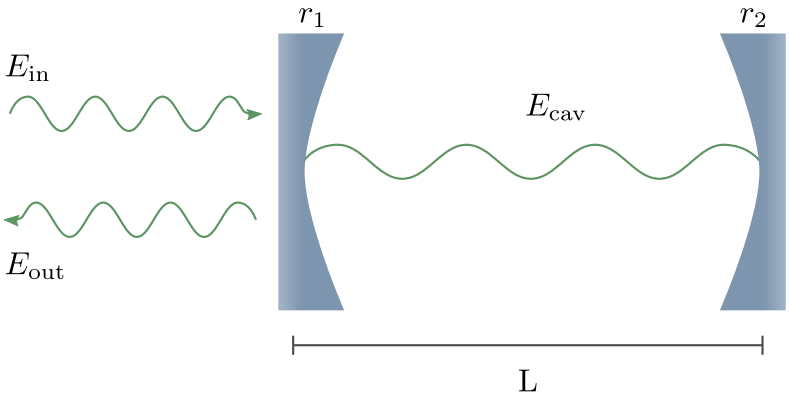

FIGURE 2.1. A Fabrey-Pérot optical cavity.

where ω_n is the angular frequency of the field, c is the speed of light, and n is a positive integer. The spacing between resonances is apparently

$$\Delta\omega_{\text{FSR}} = \pi c/L, \tag{2.2}$$

and is referred to as the free spectral range.

A single-sided cavity has one "port" through which light can couple into and out of the cavity. In this case we take $r_2 = 1$ and $r_1 < 1$. If the initial field that enters the cavity is $E_0 = \sqrt{1-r^2}E_{\text{in}}$, then the right-travelling field in the cavity after each successive round-trip is given by the series

$$\begin{aligned} E_{\text{cav}} &= E_0 + rE_0e^{-i\omega\tau_{\text{rt}}} + r^2E_0e^{-2i\omega\tau_{\text{rt}}} + ... \\ &= \frac{\sqrt{1-r^2}}{1-re^{-i\omega\tau_{\text{rt}}}}E_{\text{in}}. \end{aligned} \tag{2.3}$$

Here, $\tau_{\text{rt}} = 2L/c$ is the photon round-trip time. Interestingly, for a resonant frequency ($\omega\tau_{\text{rt}} = 2\pi n$), the intracavity field diverges as $r \to 1$, as can be seen from equation 2.3. This is one of the essential features of an optical resonator: the optical power circulating in the resonator can greatly exceed the power used to pump the resonator.

By the same procedure that was used to calculate equation 2.3, the field that leaks out of the cavity can be shown to be

$$\frac{(1-r^2)e^{-i\omega\tau_{\mathrm{rt}}}}{1-re^{-i\omega\tau_{\mathrm{rt}}}}E_{\mathrm{in}}. \tag{2.4}$$

The total field at the output of the cavity consists of two parts: the portion that leaks out of the cavity, and the portion that is promptly reflected from the input mirror. In accounting for the promptly reflected portion of the field, it is important to recall that the reflection coefficient from the left side of the mirror must have the opposite sign from the that of the right side. Thus the total output field is

$$E_{\mathrm{out}} = -rE_{\mathrm{in}} + \frac{(1-r^2)e^{-i\omega\tau_{\mathrm{rt}}}}{1-re^{-i\omega\tau_{\mathrm{rt}}}}E_{\mathrm{in}}. \tag{2.5}$$

The reflected power is equal to the input power, which can be seen by computing $|E_{\mathrm{out}}|$, but the phase of the output field is modified by the presence of the cavity. When the input is on resonance with the cavity, the output accumulates a π phase shift, as can be seen in Fig 2.2b.

2.2.1. Input-Output Formalism

In the previous section, the steady-state field inside of, and reflected from, an optical Fabrey-Pérot resonator were calculated by computing a series summation over the contribution to the total field from every possible number of round trips the intracavity field can make. This method for calculating properties of a resonator are cumbersome, and cannot be used to determine the response from a time-varying incident field. So long as the cavity has resonances that are very sharp compared to $\Delta\omega_{\mathrm{FSR}}$, and the incident field frequency is in the vicinity of a single resonance, the

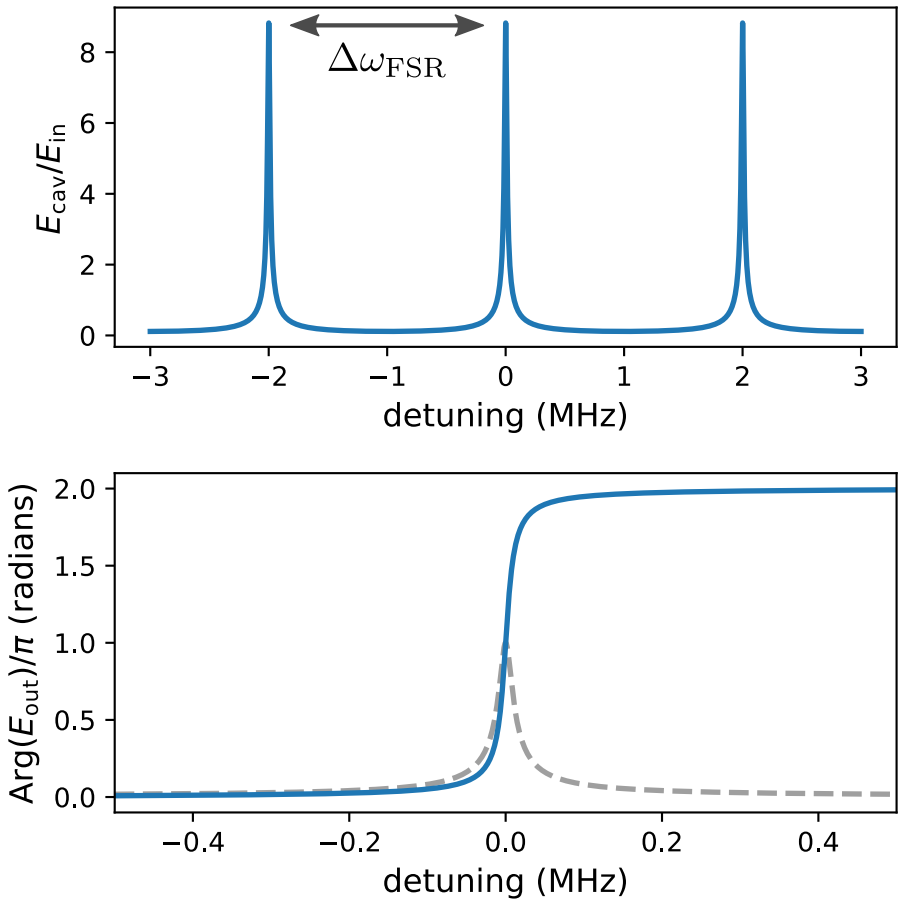

FIGURE 2.2. Cavity amplitude and phase. (a) Intracavity field as a function of optical input frequency. (b) Phase angle of the field reflected from the cavity. The dashed curve shows the normalized intracavity resonance as a guide for the eye.

input-output formalism is a very powerful framework for determining the intracavity and output fields for a given input (see figure 2.3 for a comparison to the exact expression).

In the input-output formalism, the time evolution of the intracavity field is governed by the differential equation

$$\dot{a} = -i\omega_0 a - \frac{\kappa}{2}a + \sqrt{\kappa_{\mathrm{ex}}}a_{\mathrm{in}}(t). \tag{2.6}$$

Here, a is the intracavity field amplitude, normalized such that $|a|^2 = N_{\mathrm{cav}}$ is the average intracavity photon number, κ is the photon lifetime for the cavity, which may include absorptive and scattering losses in addition to the reflectivity of the input mirror, ω_0 is the cavity resonance frequency of interest, $\kappa_{\mathrm{ex}} = t^2/\tau_{\mathrm{rt}}$ is the rate that photons couple to the cavity through the input mirror, and $a_{\mathrm{in}}(t)$ is the time-varying amplitude of the input field, normalized such that a monochromatic input field at frequency ω_L with power P gives an average photon number flux of $|a_{\mathrm{in}}|^2 = \dot{N} = P/\hbar\omega_L$.

The output from the cavity into the coupling channel (associated with coupling rate κ_{ex} and input a_{in}) is given by the input-output relation

$$a_{\mathrm{out}}(t) = a_{\mathrm{in}}(t) - \sqrt{\kappa_{\mathrm{ex}}}a(t). \tag{2.7}$$

Generally, we do not experimentally have access to the intracavity field, but are left to infer it via the output. In some cases, it is only the properties of the output field that we care about in the first place. The general strategy of the input-output formalism is to specify the form of the input $a_{in}(t)$, solve for the cavity dynamics according

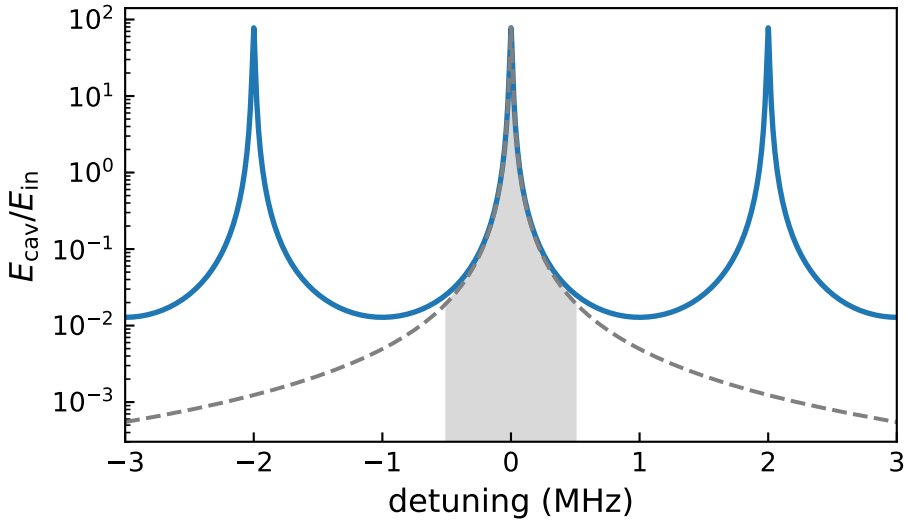

FIGURE 2.3. Comparison of exact solution and approximate solution from input-output formalism. Grey shaded area indicates ±1/4 of the free spectral range, showing very good agreement to the exact lineshape even very far from the resonance.

to equation 2.6, and solve for the output $a_{\text{out}}(t)$ using the input-output relation of equation 2.7.

Typically, the total loss rate κ is separated into two components: κ_{ex} denotes the coupling rate of the cavity to the mode of interest which will generally be driven by a laser field, and all other loss channels are lumped into a single number κ_0 (the total cavity loss rate is then $\kappa = \kappa_0 + \kappa_{\text{ex}}$). In writing the loss in such a manner, one finds the reflection coefficient from the cavity (via equations 2.6 and 2.7) for a monochromatic field $a_{\text{in}} = Ee^{-i\omega_L t}$ to be

$$r = \frac{a_{\text{out}}}{a_{\text{in}}} = \frac{(\kappa_0 - \kappa_{\text{ex}})/2 - i\Delta}{(\kappa_0 + \kappa_{\text{ex}})/2 - i\Delta}, \tag{2.8}$$

where $\Delta = \omega_L - \omega_0$. From equation 2.8, we identify three coupling regimes. When $\kappa_0 \gg \kappa_{ex}$, the system is said to be undercoupled. In this undesirable configuration, any photons that couple into the cavity through κ_{ex} are immediately lost through

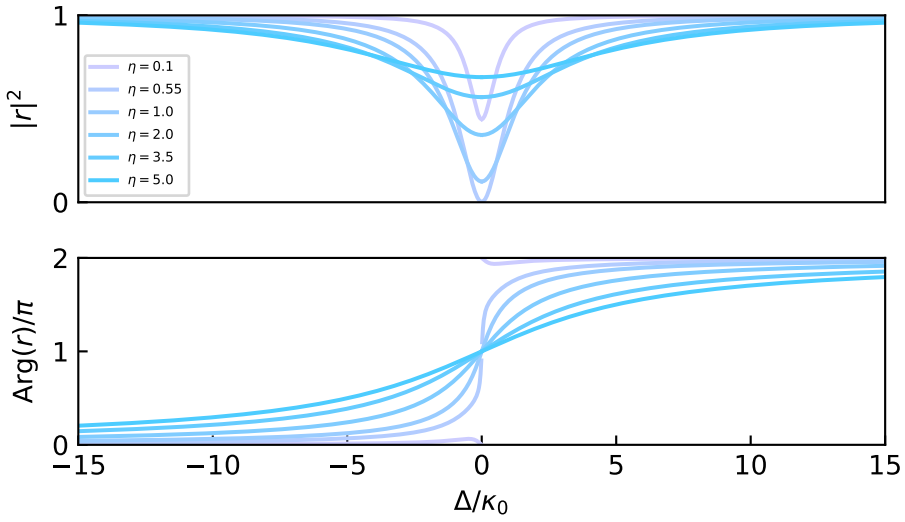

FIGURE 2.4. Normalized cavity reflection and reflected phase angle as a function of detuning for varying coupling parameter $\eta \equiv \kappa_{ex}/\kappa_0$.

the channels associated with κ_0. The reflection coefficient $r \approx 1$, meaning virtually all of the photons driving the cavity reflect off of it with no modification from the cavity. When $\kappa_0 = \kappa_{ex}$, the system is said to be critically coupled. When $\Delta = 0$, the reflection $r = 0$ for a critically coupled cavity. Finally, when $\kappa_{ex} \gg \kappa_0$, the system is overcoupled, and virtually all of the photons that enter the cavity return to the coupling channel modified by the presence of the cavity. In particular, for the overcoupled system, $|r| \approx 1$, and for fields near resonance, $r \approx -1$, meaning the output field picks up a π phase shift (consistent with equation 2.5). The properties of the reflection coefficient for various coupling parameters $\kappa_{\mathrm{ex}}/\kappa_0$ are depicted in figure 2.4.

Two useful values that characterize an optical cavity are the finesse $\mathcal{F}$ and the quality factor Q. The finesse gives the average number of round-trips a photon makes

in the cavity, and is given by the expression

$$\mathcal{F} = \frac{\Delta\omega_{\mathrm{FSR}}}{\kappa}. \tag{2.9}$$

A quick back of the envelope calculation shows that the finesse gives the enhancement of optical power circulating in the cavity over the power of the input source driving the cavity when the input is on resonance with the cavity. To see this, note that the power circulating in the cavity is $|a|^2\hbar\omega_L c/L$, and $|a|^2 = 4P_{in}/\hbar\omega_L\kappa$. The quality factor is defined in the same way as for any oscillator,

$$Q = \frac{\omega_0}{\kappa}, \tag{2.10}$$

and is a common way to quantify the system's damping.

A quantum description of the cavity is achieved by replacing the classical amplitude a with the annihilation operator for the discrete mode $\hat{a}$, and adding an additional quantum input term $\sqrt{\kappa_0}\hat{f}_{in}(t)$ for the driving of the cavity by the quantum vacuum. The quantum input operator $\hat{f}_{in}(t)$ satisfies the commutation relation $[\hat{f}_{in}(t), \hat{f}^{\dagger}_{in}(t')] = \delta(t - t')$, and ensures that the cavity mode operator $\hat{a}$ preserves its commutator $[\hat{a}(t), \hat{a}^{\dagger}(t)] = 1\ \forall t$.

In concluding this section, it should be stressed that the equations and properties of an optical cavity were derived here for a Fabrey-Pérot cavity to give a simple and concrete example, but everything generalizes for use with other types of cavity. In most cavities, the only physical change is the length of the cavity L. For example, in the context of our work, the optical modes are whispering gallery traveling waves in a spherical dielectric. The round-trip path length for the cavity is $2\pi Rn$ for a sphere of radius R and refractive index n, and thus we make the replacement $L \to \pi Rn$.

2.3. Mechanical Resonators

2.3.1. Linear Elastic Theory

The mechanical vibrational modes we consider in this work will always have wavelengths that are very large compared to the atomic spacing in the material. For such modes, the simplest description of the physics comes from a linear elastic theory, which considers the material to be continuous, with a vector displacement field $\mathbf{u}(\mathbf{r})$ at each point $\mathbf{r}$ in the material.

The fundamental quantities of interest are the strain tensor u_{ij}, and the stress tensor σ_{ij}. The strain is measure of the relative displacement of two nearby points in the material, and is given by

$$u_{ij} = \frac{1}{2}\left(\frac{\partial u_j}{\partial x_i} + \frac{\partial u_i}{\partial x_j}\right), \tag{2.11}$$

where u_i are the components of $\mathbf{u}$, and x_i are the Cartesian coordinates or $\mathbf{r}$. Note that the strain is unitless. The stress tensor gives the components of the force on each face of an infinitesimal volume element in the material, and is given by

$$\sigma_{ij} = 2\mu u_{ij} + \lambda \nabla \cdot \mathbf{u}\delta_{ij}, \tag{2.12}$$

where λ and μ are the Lamé constants, related to the Young's modulus E and Poisson ratio ν by

$$\lambda = \frac{\nu E}{(1+\nu)(1-2\nu)}, \quad \mu = \frac{E}{2(1+\nu)}. \tag{2.13}$$

In terms of the strain and stress tensors, the fundamental equations of motion are

$$\rho(\mathbf{r})\ddot{u}_i = \frac{\partial \sigma_{ik}}{\partial x_k}. \tag{2.14}$$

Substituting equations 2.11 and 2.12 gives

$$\rho(\mathbf{r})\partial_t^2 \mathbf{u}(\mathbf{r},t) = (\lambda+\mu)\nabla\left(\nabla\cdot\mathbf{u}(\mathbf{r},t)\right) + \mu\nabla^2\mathbf{u}(\mathbf{r},t). \tag{2.15}$$

Equation 2.15 can be cast as an eigenvalue problem, where the normal mode patterns of a harmonic mode $\mathbf{u}(\mathbf{r},t) = \mathrm{Re}\left[\mathbf{u}_j(\mathbf{r})e^{-i\omega_j t}\right]$ are determined by

$$\Theta\mathbf{u}_j(\mathbf{r}) = \omega_j^2\mathbf{u}_j(\mathbf{r}), \tag{2.16}$$

with the operator Θ given by

$$\Theta(\cdot) = -\frac{\lambda+\mu}{\rho}\nabla\left(\nabla\cdot(\cdot)\right) - \frac{\mu}{\rho}\nabla^2(\cdot). \tag{2.17}$$

2.3.2. Classical 1-dimensional oscillator

For a given normal mode of the resonator, it can be shown that the mode function can be decomposed as $\mathbf{u}(\mathbf{r},t) = x(t)\cdot\mathbf{u}(\mathbf{r})$, and that the equation of motion for $x(t)$ can be described by a simple 1-dimensional harmonic oscillator with effective mass m_{eff} and energy damping rate γ. The effective mass depends on the choice of normalization used. It will turn out, however, that the effective mass will appear in combination with other factors, and the combination is invariant under scaling of $x(t)$ (see section 2.4), so the particular choice of normalization does not change the physics describing

the optomechanical interaction. The equation of motion is written as

$$m_{\text{eff}}\ddot{x} + m_{\text{eff}}\gamma\dot{x} + m_{\text{eff}}\omega_m^2 x = F_{ext}(t). \tag{2.18}$$

The term $F_{ext}(t)$ includes all external forces acting on the system. At the very least, the fluctuation-dissipation theorem guarantees that if the oscillator is coupled to a dissipative bath causing energy damping γ, there must also be an associated stochastic driving term F_{th}, for if such a term did not exist, one could quite easily prepare any oscillator in the quantum ground state by simply allowing it to interact with a thermal bath and wait for the system to damp to zero!

In the Fourier domain, the response of the oscillator at a frequency ω is given by

$$x(\omega) = \chi(\omega)F_{ext}(\omega), \tag{2.19}$$

where the mechanical susceptibility is

$$\chi(\omega) = \left[m_{\text{eff}}\left(\omega_m^2 - \omega^2\right) - im_{\text{eff}}\gamma\omega\right]^{-1}. \tag{2.20}$$

For high-Q resonators, the susceptibility in the vicinity of ω_m is well approximated as Lorentzian, as depicted in figure 2.5. To see this, we write $\omega_m^2 - \omega^2 = (\omega_m + \omega)(\omega_m - \omega) \approx 2\omega_m(\omega_m - \omega)$, leading to

$$\chi(\omega) \approx \frac{1}{2m_{\text{eff}}\omega_m}\frac{1}{\omega_m - \omega - i\gamma/2}. \tag{2.21}$$

We will always use this approximation.

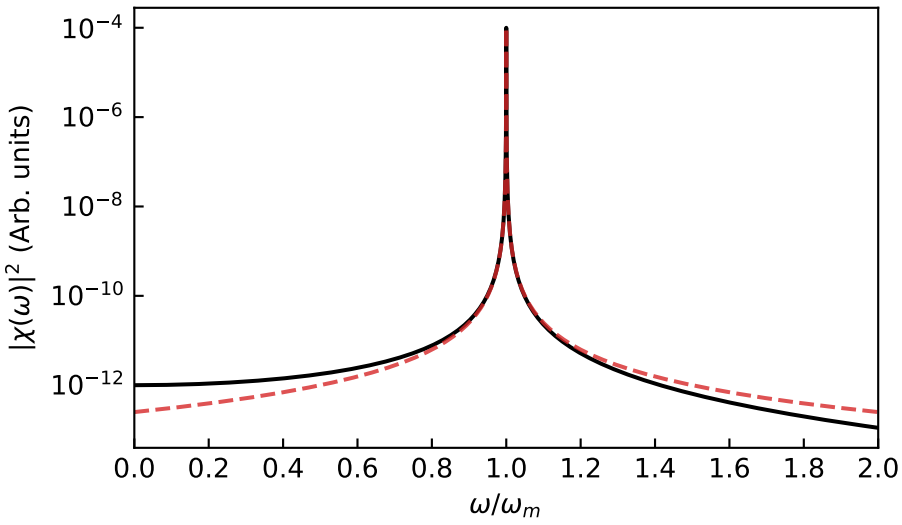

FIGURE 2.5. Mechanical susceptibility for an oscillator with $Q = 10000$. Solid black line shows the exact expression of equation 2.19, red dashed line the approximate Lorentzian of equation 2.21. The approximation has only a small deviation from the exact expression far away from resonance.

2.3.3. Oscillator coupled to thermal environment

An oscillator driven by a thermal environment has a time evolution that is statistical in nature. In this case, the properties of the system are characterized by correlation functions (see Appendix A). We will always consider the thermal noise to be white, zero-mean Gaussian noise. For such noise, $F_{th}(t)$ obeys the relations

$$\langle F_{th}(t) \rangle = 0 \tag{2.22}$$

$$G_{FF} = \langle F_{th}(t) F_{th}(t') \rangle = 2 m_{\text{eff}} \gamma k_B T \delta(t - t'). \tag{2.23}$$

The corresponding power spectral density (PSD) is white,

$$S_{FF}(\omega) = 2 m_{\text{eff}} \gamma k_B T. \tag{2.24}$$

Using equation A.7, the PSD for a thermally driven oscillator is

$$S_{xx}(\omega) = |\chi(\omega)|^2 S_{FF}^{th}(\omega). \tag{2.25}$$

Equation 2.25 has simple poles in the upper-half complex plane located at $2\gamma k_B T \omega_m e^{i\theta/2}$ and $-2\gamma k_B T \omega_m e^{-i\theta/2}$, with $\tan\theta = \gamma\sqrt{\omega_m^2 - \frac{\gamma^2}{4}}/(\omega_m^2 - \frac{\gamma^2}{2})$. Integration of equation 2.25 then gives, according to equation A.11,

$$\langle x^2 \rangle = \frac{k_B T}{m_{\text{eff}} \omega_m^2}, \tag{2.26}$$

consistent with the equipartition theorem. The effective temperature of a mode is defined by

$$k_B T_{\text{eff}} = m_{\text{eff}} \omega_m^2 \int_{-\infty}^{\infty} \mathrm{d}\omega S_{xx}(\omega)/2\pi, \tag{2.27}$$

which will deviate from the bath temperature T when the susceptibility is modified.

2.3.4. Quantum description

A quantum description of the mechanical modes is achieved by promoting x and the conjugate momentum $p = m\dot{x}$ to operators, which satisfy the commutation relation $[\hat{x}, \hat{p}] = i\hbar$. We define raising and lowering operators $\hat{b}^\dagger$ and $\hat{b}$ respectively for the mode, and they relate to $\hat{x}$ and $\hat{p}$ by

$$\hat{x} = x_{zpf}\left(\hat{b}^\dagger + \hat{b}\right) \tag{2.28a}$$

$$\hat{p} = i m_{\text{eff}} \omega_m x_{zpf}\left(\hat{b}^\dagger - \hat{b}\right), \tag{2.28b}$$

where

$$x_{zpf} = \sqrt{\frac{\hbar}{2m_{\text{eff}}\omega_m}} \tag{2.29}$$

is referred to as the zero-point fluctuation, and gives the root-mean-square displacement of the mechanical amplitude in the quantum ground state.

For the high Q mechanical modes of interest, the quantum Langevin equation corresponding to equation 2.18 (see Appendix B) is

$$\dot{\hat{b}} = \left(-i\omega_m - \frac{\gamma}{2}\right)\hat{b} + \sqrt{\gamma}\hat{b}_{in}(t), \tag{2.30}$$

where the thermal input noise $\hat{b}_{in}(t)$ has the properties

$$\langle \hat{b}_{in}(t) \rangle = 0 \tag{2.31a}$$

$$\langle \hat{b}_{in}(t)\hat{b}^{\dagger}_{in}(t') \rangle = (n_{th}+1)\delta(t-t') \tag{2.31b}$$

$$\langle \hat{b}^{\dagger}_{in}(t)\hat{b}_{in}(t') \rangle = n_{th}\delta(t-t'), \tag{2.31c}$$

and $n_{th} \approx k_B T/\hbar\omega_m$.

2.4. Optomechanical Interaction

The optomechanical interaction is most easily derived by considering the canonical system that consists of a Fabrey-Perot optical cavity where the back mirror is mechanically compliant. We will consider the coupling of a single, well resolved cavity mode described by annihilation operator $\hat{a}$ to a high Q mechanical mode of the mirror described by displacement $\hat{x}$. The Hamiltonian of the system is

$$H = \omega_c(\hat{x})\hat{a}^{\dagger}\hat{a} + \omega_m\hat{b}^{\dagger}\hat{b}, \tag{2.32}$$

where $\omega_c(\hat{x})$ is the cavity resonance frequency of mode $\hat{a}$, and ω_m is the resonance frequency of the mirror. Since the position of the mirror can change, we must keep track of how the optical resonance frequency changes with the mirror displacement. For displacements that are small enough, we can Taylor expand $\omega_c(\hat{x})$ to first order

$$\omega_c(\hat{x}) = \omega_c(0) + G\hat{x}, \tag{2.33}$$

where we have defined

$$G = \left.\frac{\partial\omega_c(x)}{\partial x}\right|_{x=0}. \tag{2.34}$$

Using equation 2.28a, we write the interaction Hamiltonian as

$$H_{int} = g_0(\hat{b} + \hat{b}^\dagger)\hat{a}^\dagger\hat{a}, \tag{2.35}$$

where

$$g_0 = x_{zpf}G \tag{2.36}$$

is referred to as the single-phonon coupling rate. g_0 gives the frequency shift induced on the optical resonance frequency by the presence of a single quantum of energy in the mechanical oscillator.

The quantum Langevin equations (QLEs) associated with the interaction are

$$\dot{\hat{a}} = (-i\omega_c - ig_0(\hat{b}(t) + \hat{b}^\dagger(t)) - \kappa/2)\hat{a}(t) + \sqrt{\kappa_{ex}}\hat{a}_{in}(t) + \sqrt{\kappa_0}\hat{f}_{in}(t) \tag{2.37a}$$

$$\dot{\hat{b}} = \left(-i\omega_m - \frac{\gamma}{2}\right)\hat{b} + ig_0\hat{a}^\dagger(t)\hat{a}(t) + \sqrt{\gamma}\hat{b}_{in}(t). \tag{2.37b}$$

The input channel is typically driven by a laser field, $a_{in}(t) = a_{in}e^{-i\omega_L t}$. We can at once explicitly factor out the fast oscillations of the dynamics and remove explicit

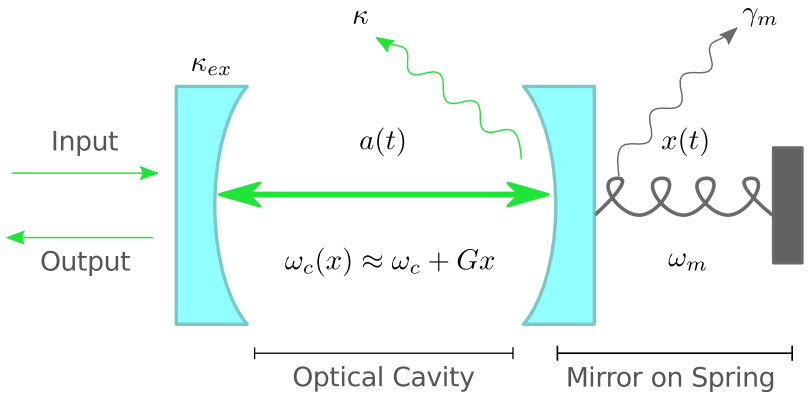

FIGURE 2.6. Canonical optomechanical system.

time-dependence in the equations of motion by making the replacements $\hat{a}_{in}(t) \rightarrow a_{in}(t)e^{-i\omega_L t}$, $\hat{f}_{in}(t) \rightarrow \hat{f}_{in}(t)e^{-i\omega_L t}$, and $\hat{a}(t) \rightarrow a(t)e^{-i\omega_L t}$. Doing so leaves the form of equation 2.37b unchanged, and equation 2.37a becomes

$$\dot{\hat{a}} = (i\Delta - ig_0(\hat{b}(t) + \hat{b}^\dagger(t)) - \kappa/2)\hat{a}(t) + \sqrt{\kappa_{ex}}a_{in}(t) + \sqrt{\kappa_0}\hat{f}_{in}(t), \tag{2.38}$$

where $\Delta = \omega_L - \omega_c$. Equation 2.38 describes the slowly changing envelope of the field that is experimentally measurable. The corresponding classical Langevin equations are

$$\dot{a} = (i\Delta - iGx(t) - \kappa/2)a(t) + \sqrt{\kappa_{ex}}a_{in}(t) \tag{2.39a}$$

$$m_{\text{eff}}\ddot{x}(t) + m_{\text{eff}}\gamma\dot{x}(t) + m_{\text{eff}}\omega_m^2 x(t) = -\hbar G|a|^2, \tag{2.39b}$$

where $a = \langle\hat{a}\rangle$, $b = \langle\hat{b}\rangle$, and $x = x_{zpf}(b + b^*)$.

As a final consideration of the optomechanical interaction, recall that the mechanical amplitude x requires some choice of normalization for the displacement field $\mathbf{u}(\mathbf{r}, t)$, and a corresponding effective mass m_{eff}. Since the optomechanical coupling rate g_0 depends on the effective mass through x_{zpf}, and x through G, it would seem that the choice of normalization is important, and that characterizing an

optomechanical system would require determining both m_{eff} and x. However, this turns out not to be so. Consider a change in the normalization such that $x \to \Gamma x$. Then, by equation 2.34, it must be that $G \to G/\Gamma$. Additionally, the effective mass will scale like $m_{eff} \to m_{eff}/\Gamma^2$, which is seen most easily by requiring the energy of the oscillator $U = \frac{1}{2} m_{eff} \omega_m^2 x^2$ to be invariant to the choice of normalization. Given these considerations, we find $g_0 = x_{zpf} G \to \Gamma x_{zpf} G/\Gamma$ is invariant. Thus, it is only the single number g_0 that completely characterizes the optomechanical system. In experiments, the value of g_0 can be measured without consideration of the effective mass and normalization of the displacement field, providing a very useful abstraction when we consider specific realizations of optomechanical systems.

2.5. Consequences of Optomechanical Interaction

2.5.1. Phase modulation

To gain a little bit of intuition about the optomechanical interaction, consider the very simplest case of a (classical) cavity mode a with a cavity length that is modulated like $x(t) = x_0 \cos(\omega_m t)$. The unitary evolution of the mode under the Hamiltonian is

$$\dot{a} = -i\omega_c a - iGx_0 \cos(\omega_m t) a. \tag{2.40}$$

Integration leads to the evolution $a(t) = ae^{-i\omega_c t - i\beta \sin(\omega_m t)}$. In other words, the field picks up a phase modulation $\phi(t) = \beta \sin(\omega_m t)$, with modulation depth $\beta = Gx_0/\omega_m$.

To add some more complexity, we first make a simplification. In all experimental systems, the phase modulation index $\beta \ll 1$. If we solve for the spectral components of the system driven by a laser $a_{in}(t) = a_{in} e^{-i\omega_L t}$ according to equations 2.39 under

the weak modulation condition, we find (Appendix C)

$$a(t) = \sqrt{\kappa} a_{in} \mathcal{L}(0) \left(1 - \frac{i\beta\omega_m \mathcal{L}(\omega_m)}{2} e^{-i\omega_m t} - \frac{i\beta\omega_m \mathcal{L}(-\omega_m)}{2} e^{i\omega_m t} \right), \tag{2.41}$$

with the lineshape function

$$\mathcal{L}(\omega) = \frac{1}{-i(\Delta + \omega) + \kappa/2}. \tag{2.42}$$

In other words, a monochromatic field in the cavity picks up sidebands at frequencies $\omega_L \pm \omega_m$ for the carrier at frequency ω_L. The amplitudes of the sidebands are proportional to the modulation depth β, and modified by their location with respect to the cavity lineshape $\mathcal{L}$. This is precisely the result we should expect. For a weak phase modulation, $e^{-i\omega_L t - i\beta \sin(\omega_m t)} \approx e^{-i\omega_L t}(1 - i\frac{\beta}{2}(e^{-i(\omega_L + \omega_m)t} - e^{-i(\omega_L - \omega_m)t}))$. Thus, a weak phase modulation is equivalent to adding sidebands to the carrier. In the presence of the cavity, the amplitude of the sidebands and carrier are modified by the cavity lineshape, and immediately we arrive at equation 2.41 (see figure 2.7). We refer to the lower frequency sideband as the red sideband, and the higher frequency as the blue sideband.

To summarize, the basic optomechanical interaction causes a monochromatic field in an oscillating cavity to become phase-modulated. A phase modulation is equivalent to an infinite number of sidebands on the carrier, and the higher order sidebands are increasingly weak. For a weak optomechanical interaction, we keep only the first-order sidebands, and find that the relative strengths of the sidebands are modified by the Lorentzian shape of the cavity. What we have essentially done in dropping the higher-order sidebands for an optomechanical cavity driven by a laser is to linearize the interaction. The details of the linearization are discussed below.

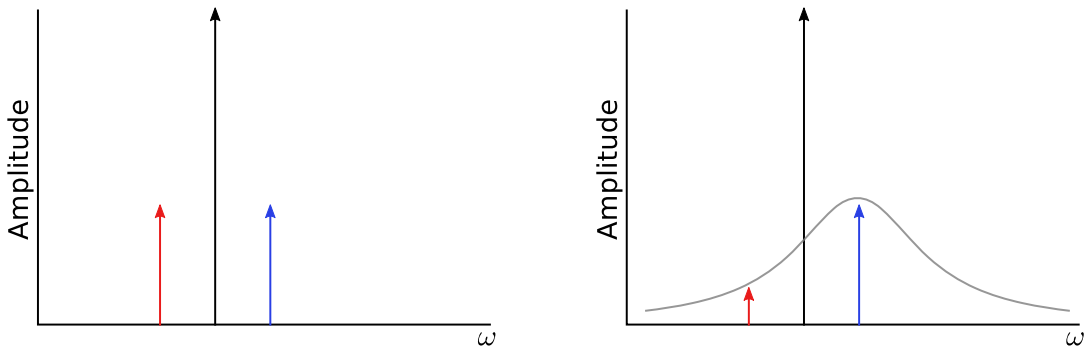

FIGURE 2.7. Modulation sidebands without (Left) and with (Right) a cavity. The carrier frequency is shown in black, while the red and blue sidebands are shown with their corresponding colors. The presence of the cavity Lorentzian lineshape in the right panel modifies the relative strengths of the red and blue sidebands according to equation 2.41

2.5.2. Linearization

The fact that in experimental systems, the modulation is small, allows us to linearize the dynamics of the system. To this end, we apply a unitary displacement to the optical field such that $\hat{a} \rightarrow \alpha + \delta\hat{a}$, where $\alpha = \langle \hat{a}(t \rightarrow \infty) \rangle$ is the classical steady-state amplitude of the laser-driven optomechanical cavity. For sufficiently small g_0, $\alpha \approx \sqrt{\kappa_{ex}} a_{in} / (\kappa/2 - i\Delta)$, in accordance with equation 2.6. The interaction Hamiltonian of equation 2.35 then becomes

$$\begin{aligned} H_{int} &= g_0 \left(|\alpha|^2 + \alpha^* \delta\hat{a} + \alpha \delta\hat{a}^\dagger + \delta\hat{a}^\dagger \delta\hat{a} \right) \left(\hat{b} + \hat{b}^\dagger \right) \\ &\approx g_0 \left(|\alpha|^2 + \alpha^* \delta\hat{a} + \alpha \delta\hat{a}^\dagger \right) \left(\hat{b} + \hat{b}^\dagger \right) \end{aligned} \tag{2.43}$$

The term $ig_0 \delta\hat{a}^\dagger \delta\hat{a}$ is assumed to be very small compared to the terms proportional to α, and are dropped. The first term in equation 2.43 is a DC offset of the amplitude $\hat{x}$ due to an average radiation pressure in the cavity, and can be eliminated by an

appropriate shift $\hat{x} \rightarrow \hat{x} - \hbar G|\alpha|^2/m_{\rm eff}\omega_m^2$. The remaining term is the linearized interaction Hamiltonian, usually written as

$$H_{int}^{lin} = g\left(\delta\hat{a} + \delta\hat{a}^\dagger\right)\left(\hat{b} + \hat{b}^\dagger\right), \tag{2.44}$$

where

$$g = \alpha g_0 \tag{2.45}$$

is the linearized optomechanical coupling rate. In writing equation 2.45, we have set the phase of the input laser $\mathrm{Im}[a_{in}]$ so that α is real, which can always be done in the single mode case without loss of generality. All of the physics we study is accurately described by the linearized form of the interaction. For the remainder of the work, we will refer to equation 2.44 as H_{int}, and will replace $\delta\hat{a}$ with $\hat{a}$. Finally, the mass of the mechanical oscillator will simply be written as m, and one must keep in mind that this is really the effective mass.

The full Hamiltonian of the linearized system is typically expressed in individual pieces as

$$H = H_{opt} + H_m + H_{int} + H_{drive} + H_{diss}. \tag{2.46}$$

The first two terms are the unperturbed optical cavity and mechanical resonator modes, $H_{opt} = -\Delta\hat{a}^\dagger\hat{a}$ (since the linearization takes place in a frame rotating at ω_L), and $H_m = \omega_m\hat{b}^\dagger\hat{b}$. The interaction terms is given by equation 2.44. The term H_{drive} describes additional weak laser probe fields that can be added to the system, and has the form $H_{drive} = \sqrt{\kappa}a_{in}\left(e^{i\omega_p t}\hat{a} + e^{-i\omega_p t}\hat{a}^\dagger\right)$ in the laboratory frame. Alternatively, one may omit the term H_{drive} from the Hamiltonian, and add the appropriate term from input-output theory when writing the equations of motion. Finally, the term H_{diss} describes the interaction of the system with the environment. It is typically used

a place holder, and one simply adds the appropriate damping terms to get QLEs with the form of equations 2.37.

With no additional drive, the classical, linearized equations of motion become

$$\dot{a} = \left(i\Delta - \frac{\kappa}{2}\right) a - i\frac{g}{x_{zpf}} x \tag{2.47a}$$

$$m\ddot{x} = -m\omega_m^2 x - m\gamma\dot{x} + \hbar\frac{g}{x_{zpf}}(a + a^*). \tag{2.47b}$$

The corresponding coupled first-order equations, which are valid for high Q mechanical modes, are

$$\dot{a} = \left(i\Delta - \frac{\kappa}{2}\right) a - ig(b + b^\dagger) \tag{2.48a}$$

$$\dot{b} = \left(-i\omega_m - \frac{\gamma}{2}\right) b - ig(a + a^\dagger). \tag{2.48b}$$

For completeness, the Fourier domain equations are

$$-i\omega a(\omega) = \left(i\Delta - \frac{\kappa}{2}\right) - i\frac{g}{x_{zpf}} x(\omega) \tag{2.49a}$$

$$-m\omega^2 x(\omega) = -m\omega_m^2 x(\omega) + im\omega\gamma x(\omega) + \hbar\frac{g}{x_{zpf}}\left(a(\omega) + a^*(\omega)\right). \tag{2.49b}$$

Note that $a^*(\omega) = [a(-\omega)]^*$.

On a final note, the linearization derived here only holds when there is a stable steady state. A slightly more general approach is to linearize around a time-varying field $\alpha(t)$, and gives the same linearized form. In both cases, there exist experimental configurations where $x \to \infty$, in which case the linearization breaks down. This situation arises when the laser is detuned near the blue sideband $\Delta \approx +\omega_m$, and is relevant in chapter VII.

2.5.3. Solving the linearized system

The linearized system can be solved exactly. The easiest approach is to consider the linearized equations of motion of equation 2.47 in the Fourier domain. The optical mode is easily solved in terms of $x(\omega)$, and gives

$$a(\omega) = \frac{-igx(\omega)/x_{zpf}}{\frac{\kappa}{2} - i(\Delta + \omega)}. \tag{2.50}$$

Equation 2.50 tells us that mechanical motion is transduced into an optical field, and the amount of transduction depends on the coupling rate g and the cavity lineshape.

We can determine how the optomechanical interaction modifies the mechanical susceptibility $\chi(\omega)$ (see equation 2.19) by adding a test force F_{test} to equation 2.47b, and writing the solution as

$$x(\omega) = \chi_{om}(\omega)F_{test}, \;\; \chi_{om}(\omega) = [\chi(\omega)^{-1} + \Sigma(\omega)]^{-1}. \tag{2.51}$$

Using the expression for $a(\omega)$ in equation 2.47b leads to

$$\Sigma(\omega) = 2m\omega_m g^2 \left\{ \frac{-\frac{i\kappa}{2} + (\Delta + \omega)}{\left(\frac{\kappa}{2}\right)^2 + (\Delta + \omega)^2} + \frac{\frac{i\kappa}{2} + (\Delta - \omega)}{\left(\frac{\kappa}{2}\right)^2 + (\Delta - \omega)^2} \right\}. \tag{2.52}$$

Under the condition $g \ll \kappa$ that is typical in our experiments, $\Sigma(\omega)$ can be replaced by $\Sigma(\omega_m)$. By comparing equation 2.21 to equation 2.51, we find that the optomechanical interaction leads to a shift in the resonance frequency of

$$\Omega_{opt} = g^2 \left\{ \frac{\Delta - \omega_m}{\left(\frac{\kappa}{2}\right)^2 + (\Delta - \omega_m)^2} + \frac{\Delta + \omega_m}{\left(\frac{\kappa}{2}\right)^2 + (\Delta + \omega_m)^2} \right\}, \tag{2.53}$$

and a modification to the linewidth by

$$\Gamma_{opt} = g^2\kappa \left\{ \frac{1}{\left(\frac{\kappa}{2}\right)^2 + (\Delta + \omega_m)^2} - \frac{1}{\left(\frac{\kappa}{2}\right)^2 + (\Delta - \omega_m)^2} \right\}. \tag{2.54}$$

In other words, the modified mechanical susceptibility is

$$\chi_{xx}(\omega)^{-1} \approx 2m\omega_m \left[\omega_m + \Omega_{opt} - \omega - \frac{i}{2}\left(\gamma + \Gamma_{opt}\right) \right]. \tag{2.55}$$

2.5.4. Resolved Sideband

Our work is done in the resolved sideband ($\omega_m \gg \kappa$) weak coupling ($g < \kappa$) regime. In this regime, when the laser is tuned exactly on the red ($\Delta = -\omega_m$) or blue ($\Delta = \omega_m$) sideband, there is no shift in the mechanical frequency. At the same time,

$$|\Gamma_{opt}| \approx \frac{4g^2}{\kappa}. \tag{2.56}$$

For blue sideband driving, $\Gamma_{opt} < 0$, leading to mechanical gain, and for red sideband driving, $\Gamma_{opt} > 0$, leading to an increased mechanical damping. The total mechanical linewidth $\Gamma = \gamma + \Gamma_{opt}$ is

$$\Gamma \approx \gamma\left(1 \pm C\right), \tag{2.57}$$

where the $+$ corresponds to red sideband driving, and the $-$ to blue, and we have defined the cooperativity C as

$$C = \frac{4g^2}{\kappa\gamma}. \tag{2.58}$$

The cooperativity is a useful number that comes up frequently in optomechanics. It is a unitless parameter that describes how strong the optomechanical coupling rate is compared to the rate that energy damps out of the system.

On the blue sideband, there is a threshold when $C = 1$, above which $\Gamma < 0$. Above $C = 1$, the oscillator has a net gain, and any displacement of the oscillator will grow exponentially. This is an unstable parameter regime for the system.

On the red sideband, as described above, the mechanical resonance frequency is unchanged, and the mechanical linewidth is broadened by a factor $1+C$. The effective temperature of the oscillator is determined by equation 2.27. Computing the integral of the modified susceptibility (equation 2.51) for a thermally driven oscillator, one finds

$$T_{eff} = \frac{T}{1+C}. \tag{2.59}$$

In other words, the temperature of the mechanical mode is effectively cooled below the temperature of the surrounding environment due to the presence of additional mechanical damping induced by the red sideband laser drive.

The resolved sideband regime can be understood physically by considering what happens to the relative strength of the optomechanically induced sidebands when the laser detuning is adjusted to satisfy $\Delta = -\omega_m$ while the oscillation frequency ω_m is increased. According to equation 2.42,

$$\left|\frac{\mathcal{L}(\omega_m)}{\mathcal{L}(-\omega_m)}\right| = \sqrt{1 + (4\omega_m/\kappa)^2}. \tag{2.60}$$

As $\omega_m/\kappa \to \infty$, the relative strength of the blue sideband to the red sideband goes to ∞. This tells us that the physics that comes from the red sideband becomes negligible when $\Delta \approx -\omega_m$ and $\omega_m \gg \kappa$. Similarly, if $\Delta \approx \omega_m$ in the limit, the blue sideband physics becomes negligible.

If we examine equation 2.52 in the limit $\omega_m/\kappa \to \infty$ and $\Delta \approx -\omega_m$, we find the second term becomes negligible compared to the first term. Tracing through the

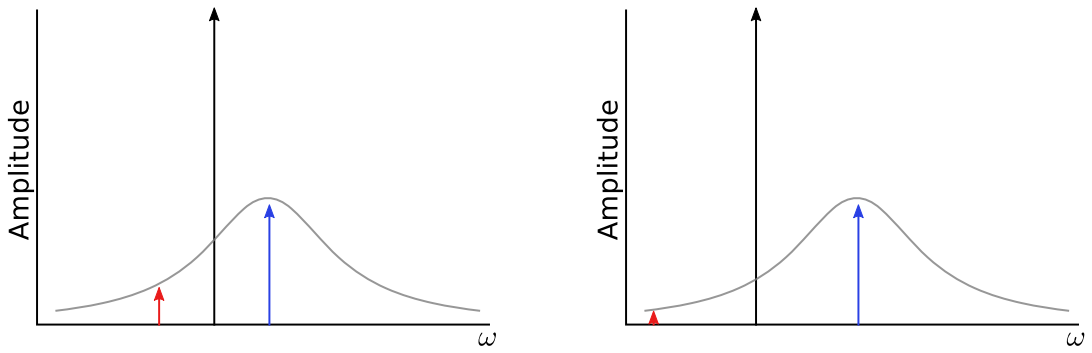

FIGURE 2.8. In the resolved sideband regime, where $\omega_m \gg \kappa$, a laser detuned near a sideband resonance ($\Delta = \pm\omega_m$) will generate only a single modulation sideband. As depicted, the laser is on the red sideband resonance. As ω_m increases, the red modulation sideband becomes increasingly suppressed by the cavity lineshape.

derivation of equation 2.52, one finds the term containing $(\Delta - \omega)$ (the second term) comes from a^* in equation 2.47b, and describes the physics of the red sideband, while the term containing $(\Delta + \omega)$ comes from a and describes the physics of the blue sideband.

The net result of the suppression of one sideband is that, depending on the laser detuning Δ, we can write an approximate form of the optomechanical interaction Hamiltonian. In particular, when $\Delta \approx -\omega_m$, the interaction is approximately a beam-splitter

$$H_{int} \approx g\left(ab^\dagger + a^\dagger b\right). \tag{2.61}$$

The beam-splitter Hamiltonian causes Rabi flopping between a and b, with the basic form

$$a(t) = a\cos(gt) - ib\sin(gt) \tag{2.62a}$$

$$b(t) = b\cos(gt) - ia\sin(gt). \tag{2.62b}$$

When the coupling rate is large compared to the cavity and mechanical damping rates, these oscillations can be observed. When the cavity decay is large compared to g (weak coupling regime), the net effect of the interaction is to convert mechanical excitations to cavity-resonant photons that promptly leak out of the cavity, and cause a net cooling of the mechanical mode, as was discussed above.

When $\Delta \approx \omega_m$, the interaction is approximately a two-mode squeezing interaction

$$H_{int} \approx g\left(ab + a^\dagger b^\dagger\right). \tag{2.63}$$

This interaction leads to exponential growth in a and b, and thus no steady-state solution exists. The time dependence is

$$a(t) = a\cosh(gt) - ib^\dagger \sinh(gt) \tag{2.64a}$$

$$b(t) = b\cosh(gt) - ia^\dagger \sinh(gt). \tag{2.64b}$$

When $\Delta \approx 0$, both sidebands contribute equally, and thus the interaction is

$$H_{int} \approx g\left(a + a^\dagger\right)\left(b + b^\dagger\right). \tag{2.65}$$

This interaction is important for quantum non-demolition measurements, but is not relevant for our work.

On a final note, for systems that satisfy the condition $g \ll \omega_m$, the approximate forms of the interaction discussed above come about with no consideration of the cavity linewidth via the rotating wave approximation. In the interaction picture

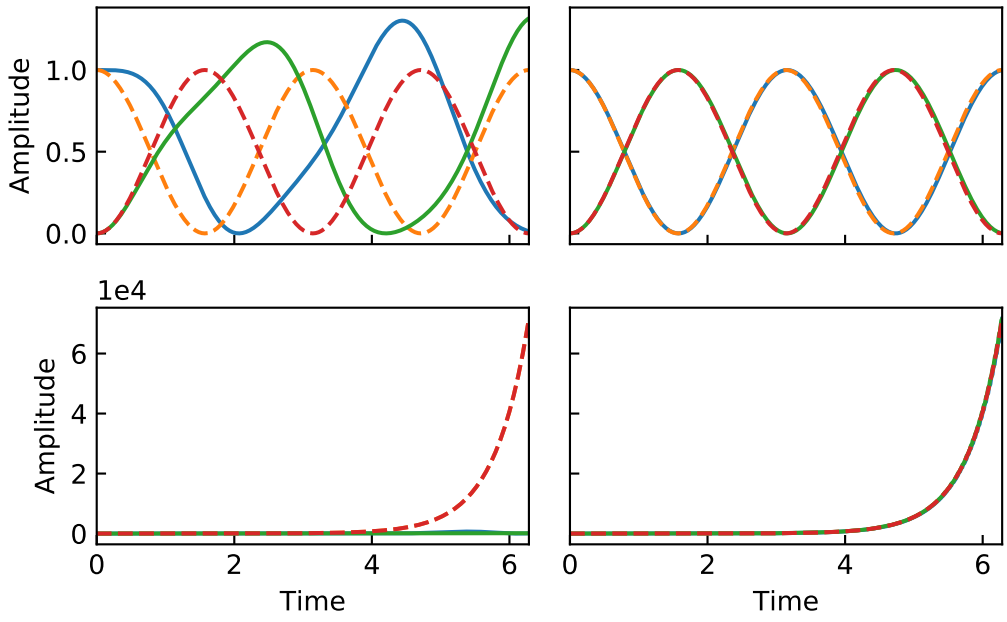

FIGURE 2.9. Comparison between the exact evolution of the linearized system (solid lines) to the approximate evolution under the rotating wave approximation (dashed lines) in the absence of any damping in the system, with initial conditions $a(0) = 0$, $b(0) = 1$. The left two panels have $g = \omega_m$, while the right panels have $g = \omega_m/100$. Upper panels have $\Delta = -\omega_m$, and so the Hamiltonian is approximately a beam-splitter. Lower panels have $\Delta = \omega_m$, giving a 2-mode squeezing Hamiltonian.

defined by $H_I = e^{-iH_0 t} H e^{iH_0 t}$, the Hamiltonian is

$$H_I = g\left(ab^\dagger e^{-i(\omega_m+\Delta)t} + abe^{-i(\omega_m+\Delta)t} + H.c.\right). \tag{2.66}$$

One readily arrives at the approximate forms discussed above by making a rotating wave approximation, dropping the terms that oscillate fast compared to g (see figure 2.9).

2.6. 3-Mode Optomechanical Systems

The basic optomechanical system described so far is a 2-mode system, comprised of a single optical cavity mode a coupled to a single mechanical mode b. The linearized

system can generate three distinct types of interaction, depending on the detuning of the driving laser with respect to the optical resonance frequency. The primary focus of the our work is to build on the basic optomechanical system, extending to multiple optical or mechanical modes. Here, the basic framework of 3-mode systems is described.

2.6.1. Mechanical Mode Coupled to Several Optical Modes

Coupling a mechanical mode to several optical modes is achieved by applying multiple laser drives that have appropriate detunings from the relevant optical modes. Since the optical modes are assumed to to be separated in frequency by much more than the mechanical mode frequency, an optical drive applied on the sideband of one optical mode can be treated as completely independent of the other optical mode.

To be concrete, consider two optical modes a_1 and a_2 with optical resonance frequencies ω_{c1} and ω_{c2}, that couple to a common mechanical mode b with frequency ω_m. The basic interaction Hamiltonian is

$$H_{int} = \left(b + b^\dagger\right)\left(g_{01}a_1^\dagger a_1 + g_{02}a_2^\dagger a_2\right). \tag{2.67}$$

Each optical mode can be linearized separately with the form $a_i(t) = (\bar{a}_i + \delta a_i)e^{-i\omega_{Li}t}$ for laser drives ω_{Li} in the vicinity of the modes a_i, leading to the Hamiltonian

$$H = H_0 + H_{int}^{(lin)} \tag{2.68}$$

with

$$H_0 = -\Delta_1\delta a_1^\dagger\delta a_1 - \Delta_2\delta a_2^\dagger\delta a_2 + \omega_m b^\dagger b \tag{2.69}$$

and

$$H_{int}^{(lin)} = g_1 \left(\delta a_1 + \delta a_1^\dagger\right)\left(b + b^\dagger\right) + g_2 \left(\delta a_2 + \delta a_2^\dagger\right)\left(b + b^\dagger\right). \tag{2.70}$$

The linearized optomechanical coupling rates are $g_i = g_{0i}\bar{a}_i$. In the same way as with the two mode system, we will relabel $\delta a_i \to a_i$, and drop the appropriate terms in a rotating wave approximation once the $\Delta_i = \omega_{Li} - \omega_{ci}$ are specified.

2.6.2. Optical Mode Coupled to Several Mechanical Modes

We consider two mechanical modes labeled b_1 and b_2, with resonance frequencies ω_{m1} and ω_{m2}, which can both couple to a single optical mode a with resonance frequency ω_c. The interaction between the modes is described by the Hamiltonian

$$H_{int} = g_{01} a^\dagger a \left(b_1 + b_1^\dagger\right) + g_{02} a^\dagger a \left(b_2 + b_2^\dagger\right). \tag{2.71}$$

The interaction can be linearized in a similar manner to the two-mode system. We consider the situation where the optical mode is driven by two laser frequencies, such that $a_{in} = \alpha_1 e^{-i\omega_{L1}t} + \alpha_2 e^{-i\omega_{L2}t}$. The mode $a(t)$ is now divided into three parts, $a(t) = \bar{a}_1 e^{-i\omega_{L1}t} + \bar{a}_2 e^{-i\omega_{L2}t} + \delta a$, where for weak couplings g_{0i}, $\bar{a}_i \approx \sqrt{\kappa_{ex}}\alpha_i / \left(i(\omega_{Li} - \omega_c) + \frac{\kappa}{2}\right)$. For strong laser drives, as in the two mode case, it is assumed that $\delta a \ll \bar{a}_i$. After appropriate shifts in b_i, and dropping the term δa^2, the linearized interaction (where we have hastily made the replacement $\delta a \to a$) is

$$H_{int} = g_{01}\left(\bar{a}_1^* e^{i\omega_{L1}t} + \bar{a}_2^* e^{i\omega_{L2}t}\right) a \left(b_1 + b_1^\dagger\right) + g_{02}\left(\bar{a}_1^* e^{i\omega_{L1}t} + \bar{a}_2^* e^{i\omega_{L2}t}\right) a \left(b_2 + b_2^\dagger\right) + \text{H.c.} \tag{2.72}$$

When $|\omega_{Li} - \omega_c| \approx \omega_{mi} \gg \kappa$, the expression simplifies to

$$H_{int} = g_1 \left(a e^{i\omega_{L1}t} + a^\dagger e^{-i\omega_{L1}t}\right)\left(b_1 + b_1^\dagger\right) + g_2 \left(a e^{i\omega_{L2}t} + a^\dagger e^{-i\omega_{L2}t}\right)\left(b_2 + b_2^\dagger\right), \quad (2.73)$$

where $g_i = g_{0i}\bar{a}_i$. Further simplification is possible once ω_{Li} are specified, by dropping the appropriate terms in a rotating wave approximation. For example, if $\omega_{L1} = \omega_c - \omega_{m1}$ and $\omega_{L2} = \omega_c + \omega_{m2}$, then the full Hamiltonian in the interaction picture is

$$H_I = g_1\left(a b_1^\dagger + a^\dagger b_1\right) + g_2\left(a b_2 + a^\dagger b_2^\dagger\right). \quad (2.74)$$

It is straightforward to generalize this approach to more than two mechanical modes.

2.6.3. Dark Modes

An important property of the 3-mode system is the existence of a dark mode. In the optomechanical system, the dark mode comes about most naturally in a system where two optical modes couple to a single mechanical mode. The Hamiltonian of the linearized system is

$$H = H_0 + H_{int} \quad (2.75)$$

where $H_0 = \omega_m b^\dagger b - \sum \Delta_i a_i^\dagger a_i$ is the unperturbed energy of the three oscillators, and the 3-mode interaction Hamiltonian couples each optical mode a_i to the mechanical mode b,

$$H_{int} = b^\dagger\left(g_1 a_1 + g_2 a_2\right) + b\left(g_1^* a_1^\dagger + g_2^* a_2^\dagger\right). \quad (2.76)$$

In writing equation 2.76, the phases of the coupling rates g_i are allowed to be complex.

The form of H_{int} motivates the definition of a new superposition mode (supermode)

$$a_B = \frac{g_1 a_1 + g_2 a_2}{\sqrt{|g_1|^2 + |g_2|^2}}, \tag{2.77}$$

so called the "bright" mode. The bright mode is normalized such that $[a_B, a_B^\dagger] = 1$. We define the corresponding "dark" mode such that $[a_B, a_D^\dagger] = 0$ and $[a_D, a_D^\dagger] = 1$. Enforcing these constraints leads to

$$a_D = \frac{g_2^* a_1 - g_1^* a_2}{\sqrt{|g_1|^2 + |g_2|^2}}. \tag{2.78}$$

If we specialize to the case $\Delta_i = \omega_m$, the full Hamiltonian can be rewritten as

$$H = \omega_m \left(b^\dagger b + a_B^\dagger a_B + a_D^\dagger a_D \right) + G \left(b^\dagger a_B + b a_B^\dagger \right), \tag{2.79}$$

where $G = \sqrt{|g_1|^2 + |g_2|^2}$. The mode a_B is "mechanically bright", meaning it couples to the mechanical mode (at rate G), while the mode a_D is mechanically dark. The Hamiltonian is diagonalized as

$$H = \sum_{i=+,-,D} \lambda_i c_i^\dagger c_i, \tag{2.80}$$

where the eigenergies are

$$\lambda_\pm = \pm G \tag{2.81}$$

$$\lambda_D = 0, \tag{2.82}$$

and the corresponding eigenstates are

$$c_{\pm} = \frac{1}{\sqrt{2}}(b \pm a_B) \tag{2.83}$$

$$c_D = a_D. \tag{2.84}$$

In the presence of damping, the dark mode remains uncoupled to the mechanical system under the condition $\kappa_1 = \kappa_2$. However, for unbalanced cavity linewidths, the dark mode begins to mix with the bright mode.

CHAPTER III

SILICA MICROSPHERES

The sole component of our optomechanical system is a fused silica microsphere. Microspheres behave as optical resonators, supporting whispering gallery modes (WGMs), modes that orbit the inner circumference of the sphere and reflect from the surface at glancing angles. The WGMs can couple either to the breathing motion of the sphere through radiation pressure in a manner analogous to the canonical system, or to whispering gallery acoustic waves through electrostriction. Below, the properties of the optical and mechanical modes of the system are reviewed.

3.1. Fabrication

All microspheres are fabricated from commercially purchased fused silica optical fiber. Depending on the experiment, the microspheres can be fabricated with diameters as small as ~ 15 μm, to as large as $\gtrsim 200$ μm.

Spheres with diameters less than ~ 50 μm are fabricated by focusing a Synrad G48 CO_2 laser onto a thin section of fiber. The ~ 10 μm wavelength field emitted from the CO_2 laser is strongly absorbed by the glass fiber, causing it to melt. Once the glass is molten, surface tension forms a spherical droplet. By feeding more fiber into the beam, the size of the sphere is increased. However, when the size of the sphere becomes too large, a temperature gradient occurs from the front of the sphere, where the laser impinges on the glass, to the back side. We have found, through experience, that acoustic whispering gallery modes are not supported in spheres made in this manner, which we believe to be a result of internal stresses in the sphere caused by

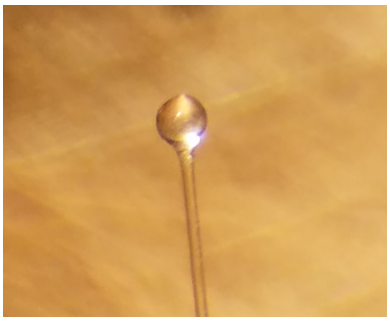

FIGURE 3.1. Image of a fused silica microsphere, approximately 75 μm in diameter. This sphere was fabricated by slowly feeding and rotating a thin fiber stem (produced by etching a Corning SMF-28e+ fiber in Hydrofluoric acid to $\approx 20\mu$m diameter) into the electrical arc of a fusion splicer.

the temperature gradient. For even larger spheres, the temperature gradient can lead the droplets that are aspherical.

Larger spheres are fabricated by feeding a section of fiber into a commercial Fujikura FSM-17s fusion splicer, a device designed to fuse two sections of fiber together through heating induced by an electrical arc. The electrical arc provides more even heating than the CO_2 laser, making it the ideal choice for large diameter spheres. Since the fusion splicer is being used for something other than its intended purpose, a small modification must be made. The fusion splicer fixes the fiber in place during its normal mode of operation, which prevents the fiber from being fed manually into the arc. To remedy this, the fiber is first fed through a protective fiber sleeve. The sleeve is fixed in place by the fusion splice, but the fiber is free to slide in the sleeve. Figure 3.1 shows a typical microsphere fabricated with the fusion splicer.

3.2. Optical Modes

Even the smallest spheres used in our experiments satisfy the condition $\lambda \ll 2\pi R$, and so we can can gain some insight into the optical modes of the microsphere through ray optics. For a sphere with refractive index n surrounded by air (refractive index

≈ 1), the critical angle for total internal reflection on the inner boundary of the sphere is given by the condition $\sin\theta_c = 1/n$. When the angle of incidence of a ray inside the sphere is greater than θ_c, it undergoes total internal reflection. Because of the symmetry of the sphere, the ray will approach the boundary at the same angle after each successive reflection. Therefore, a ray that is once totally internally reflected corresponds to a ray that will always be totally internally reflected. If the wavelength is an integer multiple of the round trip length of the cavity,

$$\lambda = 2\pi Rn/m \tag{3.1}$$

for integer m, the ray corresponds to an eigenmode of the cavity. The free spectral range for the modes is given by

$$\Delta\omega_{fsr} = \frac{c}{nR}. \tag{3.2}$$

The optical mode patterns of a dielectric sphere are not determined from ray optics, but instead are solutions to the wave equation derived from Maxwell's equations. The wave equation for the electric field is

$$\nabla^2\mathbf{E} + n^2k^2\mathbf{E} = 0, \tag{3.3}$$

where n is the refractive index, and $k = \omega/c$ is the wave number in vacuum. The vectorial wave equation is difficult to solve, but for a spherically symmetric systems can be reduced to a scalar wave equation

$$\nabla^2\psi + n^2k^2\psi = 0. \tag{3.4}$$

The electric field is decomposed into a transverse electric (TE) component with zero radial electric field, and a transverse magnetic (TM) mode with zero radial magnetic field. The TE and TM modes are decoupled, and are related to the scalar field ψ by

$$\mathbf{E}_{TE} = \nabla \times (\mathbf{r}\psi) \tag{3.5}$$

$$\mathbf{E}_{TM} = \nabla \times \nabla \times (\mathbf{r}\psi)\,. \tag{3.6}$$

Performing a separation of variables on equation 3.4 leads to solutions of the form

$$\psi_{lm}(r,\theta,\phi) = z_l(nkr)Y_{lm}(\theta,\phi), \tag{3.7}$$

where $z_l(nkr)$ are spherical Bessel functions, and $Y_{lm}(\theta,\phi)$ are the spherical harmonics. To have solutions that are finite at the origin and as $r \to \infty$, we seek solutions of the form

$$\psi(r,\theta,\phi) = \begin{cases} \sum_{lm} a_{lm} j_l(nkr)Y_{lm}(\theta,\phi) & r \le R \\ \sum_{lm} b_{lm} h_l^{(1)}(kr)Y_{lm}(\theta,\phi) & r > R, \end{cases} \tag{3.8}$$

where $j_l(x)$ is the spherical Bessel function and $h_l^{(1)}(x)$ is the spherical Hankel function of the first kind, and the radius of the sphere is R. Continuity of ψ at the boundary of the sphere leads to the condition

$$\frac{b_{lm}}{a_{lm}} = \frac{j_l(nx)}{h_l^{(1)}(kx)}, \tag{3.9}$$

where $x \equiv kR$. One must also require $\mathrm{d}\psi/\mathrm{d}r$ to be continuous at the boundary, which leads to the relation

$$f_{lm}(x) = nlj_{l-1}(nx) - n(l+1)j_{l+1}(nx) - \frac{j_l(nx)}{h_l^{(1)}(x)}\left[lh_{l-1}^{(1)}(x) - (l+1)h_{l+1}^{(1)}(x)\right] = 0 \tag{3.10}$$

The eigenmodes are typically denoted by the values (μ, l, m, ν), where μ denotes the polarization (TE or TM), and ν gives the solution corresponding to the ν^{th} root of f_{lm}. The mode number l corresponds to the total angular momentum of the field, while the z component is given by m, and can take on values $m = -l, ..., 0, ..., +l$. The $l = m$ modes are the fundamental modes, which are strongly localized on the equator, and have m equatorial nodes. In general, there are $l - |m| + 1$ lobes in the range $0 < \theta < \pi$. There are also ν radial maxima in the sphere, and the field extends further radially beyond the sphere as ν increases. The properties of $\psi_{\nu lm}$ are shown in figure 3.2.

The optical WGMs correspond to the situation where the optical field undergoes total internal reflection on the inner surface of the sphere. Clearly, one cannot couple to these modes by shining a laser directly at the sphere, since a ray that undergoes total internal reflection once in the sphere must always undergo total internal reflection by symmetry, or conversely, a ray that enters the sphere from the outside will never undergo total internal reflection. Instead, we use an adiabatically tapered single-mode optical fiber to achieve coupling. A single mode fiber is tapered by stretching the fiber while a section is heated with a Hydrogen flame. As the fiber thins, the core becomes so small as to become negligible, and the cladding becomes the new core, while the surrounding air becomes the new cladding. When the tapered section becomes sufficiently thin, it is again single-mode, and provided the diameter

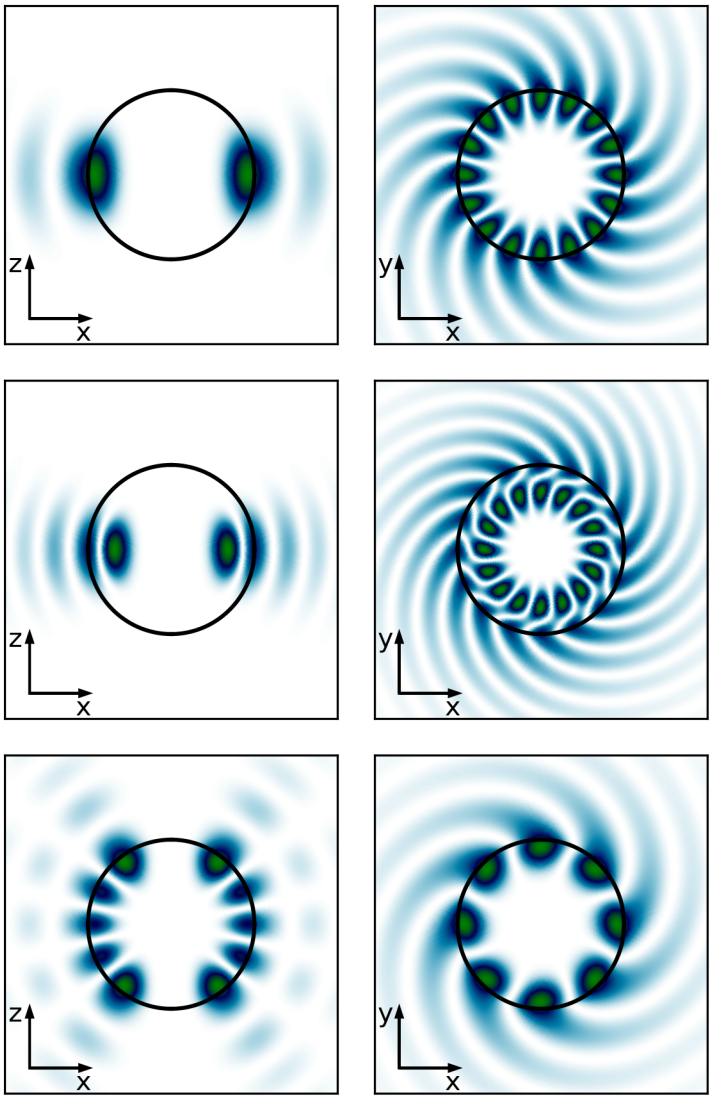

FIGURE 3.2. Field patterns for a fused silica sphere (n =1.44), surrounded by air. From top to bottom, $l = m = 8$, $\nu = 1$; $l = m = 8$, $\nu = 2$; $l = 8$, $m = 4$, $\nu = 1$.

of the fiber changes slowly compared to the wavelength, the single mode profile is adiabatically preserved across the multi-mode region over which the tapering occurs. For very thin tapered sections, a significant portion of the fiber mode is an evanescent field in air. If the evanescent field is made to overlap the evanescent field of a WGM, coupling between the fiber mode and WGM is achieved.

The modes that are excited by the tapered fiber have $|m| \approx l$, and the particular mode that is excited by a taper depends on the wavelength of the laser, as well as the position of the taper with respect to the sphere. In principle, all $2l$ values of m for a given l are degenerate, but in practice, small imperfections in the sphere, as well as the presence of the stem, break the perfect spherical symmetry, and one measures many optical modes across a single free spectral range. Because all the modes still have $|m| \approx l$, the field is weak near the stem, and so to a good approximation the supported modes match that of a perfect sphere. Since all modes are measured at the output of a single mode fiber, there is no good way to determine the exact mode numbers of the optical modes we excite. However, the important parameters of the optomechanical system are the coupling rates κ_{ex} and κ, and those values can be easily measured, as will be discussed later in the next chapter.

3.3. Mechanical Modes

There are two types of mechanical modes present in the sphere that can couple to optical WGMs. They are the radial breathing modes, and acoustic whispering gallery modes. The allowed modes are determined by solutions of the linear elastic wave equation (equation 2.15). In a manner very similar to the electromagnetic wave equation, equation 2.15 can be simplified by decomposing the displacement field $\mathbf{u}$

into a transverse component $\mathbf{u_t}$ and longitudinal component $\mathbf{u_l}$, which satisfy

$$\nabla \cdot \mathbf{u_t} = 0 \tag{3.11}$$

$$\nabla \times \mathbf{u_l} = 0. \tag{3.12}$$

Equation 2.15 leads to two independent wave equations with the form

$$\ddot{\mathbf{u}}_\mathbf{i} - c_i^2 \nabla^2 \mathbf{u_i} = 0, \tag{3.13}$$

where $i = l, t$ and

$$c_l = \sqrt{\frac{E(1-\nu)}{\rho(1+\nu)(1-2\nu)}}, \qquad c_t = \sqrt{\frac{E}{2\rho(1+\nu)}}. \tag{3.14}$$

We may then arrive at a scalar wave equation by writing the longitudinal component as the gradient of a scalar potential

$$\mathbf{u_l} = \nabla \phi, \tag{3.15}$$

and the transverse component in terms of the scalar potential

$$\mathbf{u_t} = \nabla \times \mathbf{A}. \tag{3.16}$$

Specifying $\mathbf{A} = (r\psi, 0, 0)$ leads to two orthogonal kinds of transverse displacement

$$\mathbf{u_{t1}} = \nabla \times \mathbf{A} \tag{3.17}$$

$$\mathbf{u_{t2}} = \nabla \times \nabla \times \mathbf{A}, \tag{3.18}$$

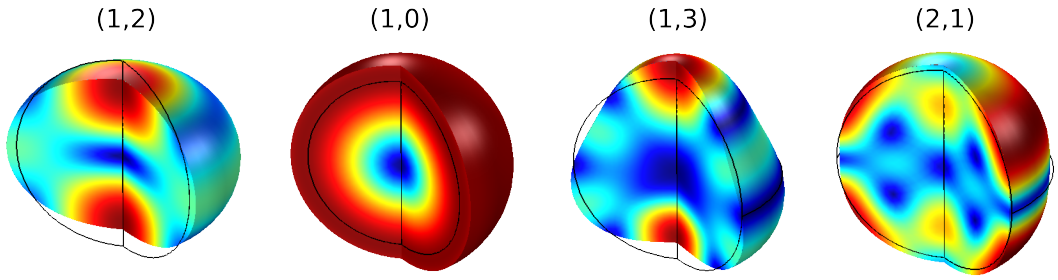

FIGURE 3.3. The first few breathing modes of an SiO_2 sphere. The modes shown have increasing frequency going from left to right, and are labeled by the mode numbers (n, l).

which looks identical to the treatment of the optical modes.

The radial breathing modes are solutions of the wave equation that have purely radial displacement. The modes are by labeled by a radial number n, corresponding to $n-1$ radial nodes, and angular mode number l. For a perfect sphere, the eigenmodes don't involve the mode number m, and there is a $2l+1$ degeneracy in the modes (n, l). The first few modes are shown in figure 3.3. It is interesting to note that the eigenfrequencies are not ordered by mode number.

The presence of the fiber stem will have an impact on the shapes of the modes, and in some cases will also break the degeneracy of the m modes. More importantly, modes that have a large displacement near the stem will cause vibrational energy in the mode to leak into the environment, resulting in low mechanical Q factors. This effect is known as clamping loss, and is mitigated by making the stem very thin where it meets the sphere, as well as by choosing the mechanical modes with the smallest displacements near the stem.

The acoustic WGM is a form of surface acoustic wave (SAW). SAWs are characterized by their localization near a surface. The mode amplitude typically decays into the bulk on a length scale comparable to the wavelength of the mode. These modes are very similar to the low order optical whispering gallery modes. An

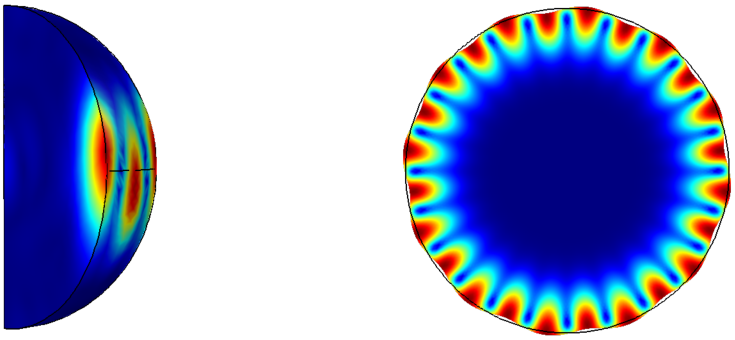

FIGURE 3.4. Acoustic whispering gallery mode field pattern. The mode is confined near the equator and the surface. Left: A wedge of the sphere shows the mode pattern along the polar angle as well as its decay away from the surface. Right: Equatorial plane shows the mode pattern along the circumference as well as the decay away from the surface.

example of the SAW WGM is shown in figure 3.4. One key difference for coupling SAW WGMs to optical modes in an optomechanical system is that the SAW WGM does not change the optical path length in the cavity, and so the canonical system is not a good representation of the interaction. Instead, the SAW WGM creates a periodic pressure modulation near the surface of the sphere, which modulates the refractive index, acting like a moving optical grating in much the same manner as an acousto optic modulator. A WGM optical mode can scatter off the SAW WGM into another optical mode. However, in order for the interaction to take place, the phase matching condition $l_2 = l_1 + l_m$ must be met, where l_1 is the pumped optical mode's angular momentum mode number, l_2 is the scattered optical mode's angular momentum mode number, and l_m is the SAW WGM angular momentum mode number. Clearly, this phase matching condition is a condition that the angular momentum be conserved in the scattering process.

Physically, the interaction between the pressure wave and the optical mode takes place through electrostriction, and is a Brillouin scattering process, as opposed to

the radiation pressure produced by optical reflection that serves as the basis for the canonical interaction. The fundamental interaction Hamiltonian for the Brillouin optomechanical system is

$$H_{int} = g_0 \left(a_1 a_2^\dagger b + a_1^\dagger a_2 b^\dagger \right), \tag{3.19}$$

where a_1 is the lower frequency (and lower l) mode. The linearization is done by replacing the pumped mode operator with its steady-state value for a laser drive. For example, driving the mode a_1 leads to the linearized Hamiltonian

$$H_{int}^{lin} = g \left(a_2^\dagger b + a_2 b^\dagger \right), \tag{3.20}$$

with $g = \langle a_1 \rangle g_0$, corresponding to the normal linearized Hamiltonian for red-sideband laser driving. Driving the mode a_2 leads to the proper form for a blue-sideband driven system. Since the Hamiltonian of the Brillouin system is to a good approximation identical to that of the canonical system, we will use the normal language of optomechanics, and refer to this as a 2-mode optomechanical system, ignoring the pumping optical mode. While the Hamiltonian for the interaction is the same for the two types of optomechanical system, the presence of the pump optical mode will change the functional form of the detected signals we use to measure the optomechanical properties of the system, and so while we ignore the presence of the pump mode to draw the analogy to the canonical system, we must be careful to consider the role it plays in the detection, which will be discussed in the next chapter.

CHAPTER IV

CHARACTERIZATION TECHNIQUES

Characterizing the optomechanical system can be broken down into three parts: characterizing the optical properties, mechanical properties, and optomechanical coupling. Typically, the optical modes are characterized first, as we can immediately measure optical modes even in microspheres that do not support high Q mechanical modes. Next, we search for mechanical modes if detected, measure the properties of those modes. Finally, once the optical mechanical modes have been characterized, the optomechanical coupling rate can be measured. Usually, we want to know the optomechanical cooperativity C, since the cooperativity alone is a good metric for the entire optomechanical system, and being a unitless parameter, provides a good comparison between different optomechanical systems. Since the cooperativity is given by $C = 4g^2/\kappa\gamma$, the optical and mechanical properties we are most interested in are the total loss rates.

4.1. Optical Mode Characterization

The optical mode parameters that are of primary importance to the optomechanical experiments are the total linewidth κ and the input coupling rate κ_{ex}. The total linewidth is determined by measuring the optical transmission spectrum, which has the functional form of equation 2.8, and is plotted in figure 2.4 for various ratios of κ_{ex}/κ_0.

Equation 2.8 is an inverted Lorentzian with a full width at half max (FWHM) of κ. The essential components of the measurement are shown in figure 4.1. A function generator is used to send a linear ramp voltage to the laser, which sweeps the optical

frequency. We use a New Focus TLB laser, and send the ramp voltage to the frequency modulation input of the controller, which can control the optical frequency in the range of $\sim$ 30 GHz. The laser passes through an electro-optic modulator (EOM) in order to phase-modulate the laser field. For a laser field $a_L(t) = a_L e^{-i\omega_L t}$, the output from the EOM is $a_{in} = a_L e^{-i(\omega_L t - \alpha V(t))}$, where $V(t)$ is the time varying voltage driving the EOM, and α is a proportionality constant that describes the phase delay per unit voltage. When the EOM is driven with a sinusoidal voltage $V(t) = V_0 \sin(\Omega_m t)$ with sufficiently small V_0, the output from the EOM can be Taylor expanded to give

$$a_{in} \approx a_L e^{-i\omega_L t} \left(1 - \beta e^{-i\Omega_m t} + \beta e^{i\Omega_m t}\right), \tag{4.1}$$

where $\beta = \alpha V_0/2$. From the input-output relations, the output from the cavity is

$$\frac{a_{out}}{a_{in}} = \mathcal{R}(0)e^{-i\omega_L t} - \beta\mathcal{R}(\Omega_m)e^{-i(\omega_L+\Omega_m)t} + \beta\mathcal{R}(-\Omega_m)e^{-i(\omega_L-\Omega_m)t}, \tag{4.2}$$

where the output function $\mathcal{R}$ is defined as

$$\mathcal{R}(\omega) = \frac{(\kappa_0 - \kappa_{ex})/2 - i(\Delta + \omega)}{(\kappa_0 + \kappa_{ex})/2 - i(\Delta + \omega)} \tag{4.3}$$

with Δ the detuning of the laser from the cavity ($\Delta = \omega_L - \omega_c$). The signal measured by the photodetector is converted to a voltage $v(t) \propto |a_{out}(t)|^2$. The signal $v(t)$ is comprised of a DC component and signals at Ω_m and $2\Omega_m$. The DC signal,

$$v_{DC} \propto |\mathcal{R}(0)|^2 + |\beta\mathcal{R}(\Omega_m)|^2 + |\beta\mathcal{R}(-\Omega_m)|^2, \tag{4.4}$$

consists of three inverted Lorentzians, equally spaced by Ω_m. The two outer Lorentzians are shallower than the central by an amount $|\beta|^2$, and all three have FWHM of κ.

To determine the optical linewidth, the output from the photodetector is sent through a low-pass filter to isolate v_{DC}. The dips in the Lorentzian triplet are individually fit using nonlinear least-squares curve fitting. The separation between the two outer dips, which are separated by $2\Omega_m$, is used to calibrate the x-axis to frequency. The linewidth κ may then be determined by the fit parameters (see figure 4.1).

In applications where the phase modulation depth β is too small, the sideband transmission dips cannot be seen. An alternative method is to use the portion of the detected voltage at frequency Ω_m, which is given by the expression

$$v_{\Omega_m} \propto \mathrm{Re}\left[\xi\right]\cos(\Omega_m t) + \mathrm{Im}\left[\xi\right]\sin(\Omega_m t) \tag{4.5}$$

with

$$\xi = \frac{\beta}{2}\left[\mathcal{R}^*(-\Omega_m)\mathcal{R}(0) - \mathcal{R}^*(0)\mathcal{R}(\Omega_m)\right], \tag{4.6}$$

detected on a lock-in amplifier. The quadrature signal is the Pound-Drever-Hall error signal, which can also be used for feedback control of the laser detuning from the cavity. It has zero-crossings at $\Delta = 0, \pm\Omega_m$, which provide an alternative signal that can be used to calibrate the x-axis to frequency and determine the linewidth of the optical mode (Figure 4.2).

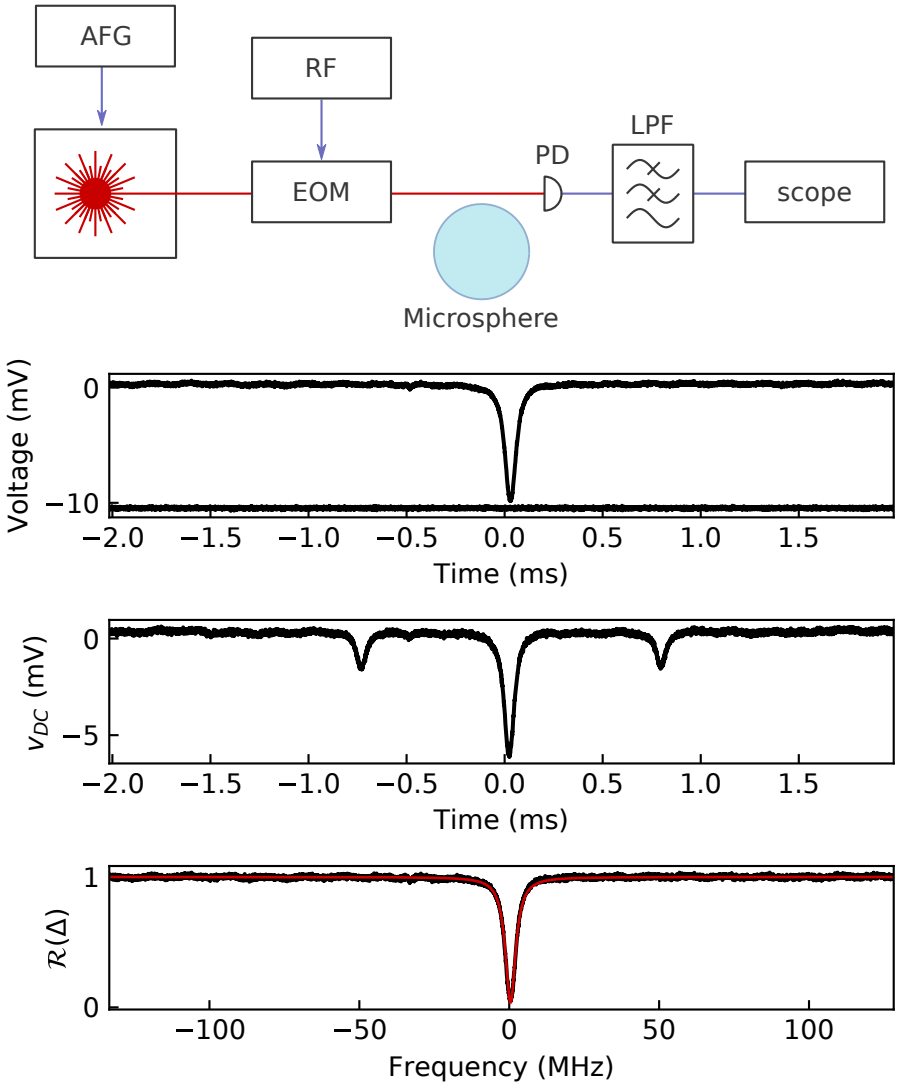

FIGURE 4.1. Optical mode characterization. Top: Essential components required to measure the linewidth of an optical mode. AFG: arbitrary function generator, RF: signal generator, EOM: electro-optic modulator, PD: photo-detector, LPF: low-pass filter, scope: oscilloscope. Bottom: Processing optical transmission data to determine the linewidth of an optical mode in a large (~ 150 μm diameter) microsphere is shown in the lower three panels. Top panel: Raw optical transmission data collected by sweeping the laser frequency through the optical resonance . The baseline is measured with the laser off. Middle panel: Raw optical transmission data collected in the same manner as upper panel, but with the RF signal generator on. The functional form of the waveform is given by equation 4.4. Lower panel: Waveform from the top panel, with the y-axis normalized from the baseline trace in the upper panel, and the x-axis calibrated from data fitting to the middle panel. The red line is a least squares fit to $|\mathcal{R}(\Delta)|^2$, giving $\kappa/2\pi = 4.1$ MHz.

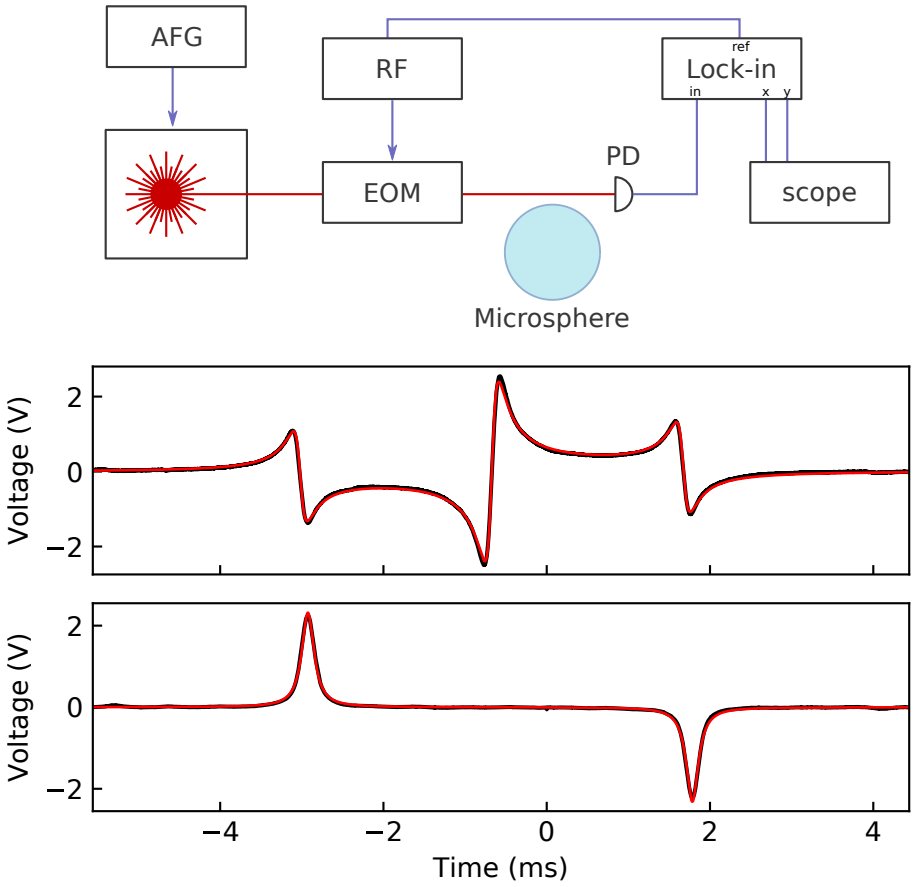

FIGURE 4.2. Pound-Drever-Hall error signal measurement. Top: Experimental setup for detecting the Pound-Drever-Hall signal with a weak phase modulated laser. Lower panels show the Pound-Drever-Hall signal (top panel) and its quadrature (lower panel) in black, with fits to equation 4.6 in red. The corresponding optical linewidth is 3.8 MHz.

4.2. Mechanical Mode Characterization

When solving the linearized optomechanical equations, we found from equation 2.50 that the mechanical displacement is transduced into an optical cavity field. Thus, the laser driven optomechanical system provides a natural way to measure the properties of the mechanical mode optically (figure 4.3). Because the Brillouin system requires the presence of two optical modes, the functional form of the measured signal differs from that of a single optical mode detection, as is used for the breathing mode. Both forms are discussed below.

There are several techniques one can use to measure the mechanical spectrum optically. The most commonly used in optomechanics are direct detection and homodyne spectroscopy. Direct detection is the simplest to implement experimentally, and is our preferred technique. To perform a direct detection measurement, the laser drive is tuned near the red sideband of the optical mode, and the output is detected on fast photodiode and sent to a real-time spectrum analyzer, which measures the frequency components of the signal (see figure 4.3).

Fluctuations in the mechanical displacement, described by a power spectral density $S_{xx}(\omega)$, will induce fluctuations on the cavity resonance frequency $S_{\omega\omega}(\omega) = G^2 S_{xx}(\omega)$. The fluctuations in the optical frequency at the output of the cavity will beat against the portion of the laser drive that passes by the optical cavity without interacting. It is the beating in the optical power detected on the photodiode that is used to infer $S_{xx}(\omega)$. In general, the power spectral density of the optical power depends on the properties of the optical cavity and detuning of the laser, and will have a functional form

$$S_{PP}(\omega) = \frac{P_{in}^2 G^2}{\omega^2} K_D(\omega) S_{xx}(\omega), \tag{4.7}$$

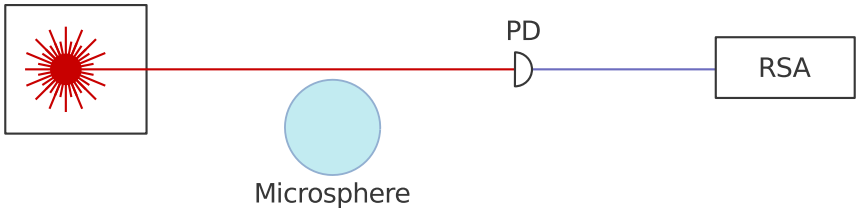

FIGURE 4.3. Essential components required to measure the mechanical motion. The mechanical spectrum is transduced onto the optical field, which is measured on an AC-coupled high speed photodiode. The signal from the photodiode is measured on a real-time spectrum analyzer (RSA).

where $K_D(\omega)$ will depend on the optical cavity parameters and detuning (for details see appendix D).

For the breathing mode case, where there is only one optical mode and the laser is detuned by Δ from the optical resonance, the transduction function is found to be

$$K_D(\omega) = \frac{4\kappa_{ex}^2\Delta^2\omega^2\left[\omega^2 + (\kappa - \kappa_{ex})^2\right]}{\left((\Delta+\omega)^2 + \frac{\kappa^2}{4}\right)\left((\Delta-\omega)^2 + \frac{\kappa^2}{4}\right)\left(\Delta^2 + \frac{\kappa^2}{4}\right)^2}. \tag{4.8}$$

The function K_D is maximum when $\Delta = \pm\kappa/2$ or $\Delta = \pm\omega_m$.

For Brillouin scattering, the transduction function is

$$K_B(\omega) = 4\omega^2\kappa_{\text{ext}}\kappa_{\text{ex,L}}|\mathcal{R}_L(0)\mathcal{L}_L(0)\mathcal{L}(\omega)|^2, \tag{4.9}$$

or, expanding $\mathcal{R}$ and $\mathcal{L}$,

$$K_B(\omega) = \frac{4\kappa_{\text{ext}}\kappa_{\text{ex,L}}\omega^2\left[\Delta_L^2 + \left(\frac{\kappa_L}{2} - \kappa_{\text{ex,L}}\right)^2\right]}{\left(\left(\frac{\kappa_L}{2}\right)^2 + \Delta_L^2\right)^2\left(\left(\frac{\kappa}{2}\right)^2 + (\Delta+\omega)^2\right)}, \tag{4.10}$$

where Δ is the detuning from the scattered optical mode, and Δ_L is the detuning of the laser from the pump mode. With this notation, driving the red sideband corresponds to $\Delta = -\omega_m$ (see figure 4.4), consistent with the detuning defined for

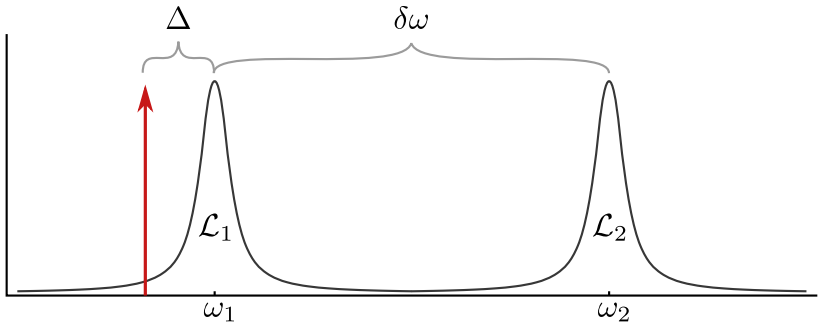

FIGURE 4.4. Laser drive configuration for detecting Brillouin mechanical modes. The laser drives the pump mode (in this case mode 1 but the expressions are the same for driving mode 2) with detuning Δ_L. Brillouin scattering off a SAW WGM at frequency ω will generate an optical field at $\Delta_L + \omega$, which will have a detuning $\Delta_L + \omega - \delta\omega$ from the scattered mode.

the canonical system. The frequency spacing between the pump and scattered optical modes is denoted $\delta\omega$, so that the laser detuning Δ_L can be related to the sideband detuning Δ as $\Delta_L = \Delta + \delta\omega$. When the distance between the optical modes is the mechanical frequency ($\delta\omega = \omega_m$), then $\Delta_L = 0$ when $\Delta = -\omega_m$. When the two modes have equal coupling rates κ_{ex} and linewidths κ, the transduction function in terms of the sideband detuning becomes

$$K_B(\omega) = \frac{4\kappa_{ex}^2\omega^2\left[(\Delta+\delta\omega)^2 + \left(\frac{\kappa}{2} - \kappa_{ex}\right)^2\right]}{\left(\frac{\kappa^2}{4} + (\Delta+\delta\omega)^2\right)^2\left(\frac{\kappa^2}{4} + (\Delta+\omega)^2\right)}. \tag{4.11}$$

An important difference between K_D and K_B is that K_D is maximum when the laser is driven on a sideband, independent of the coupling parameter κ_{ex}/κ, which also gives the maximum optomechanical interaction (Figure 4.5). On the other hand, for critical coupling ($\kappa_{ex} = \kappa/2$), $K_B = 0$ when the laser is tuned exactly on the pump resonance ($\Delta_L = 0$). To have simultaneously a strong Brillouin scattering interaction and detection then requires overcoupling the pump optical mode. The reason the signal goes to zero when the pump laser is on resonance with the pump mode is

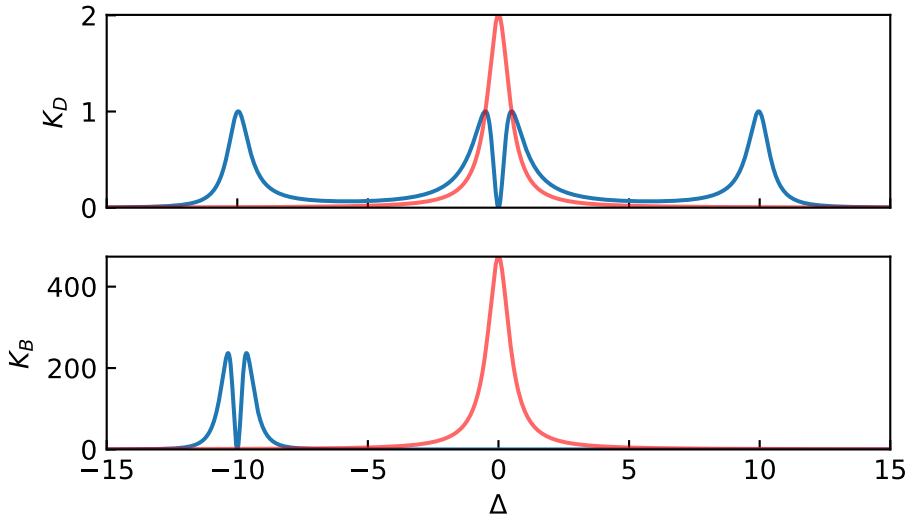

FIGURE 4.5. Transduction functions for direct detection of mechanical motion, with $\omega_m/\kappa = 10$, and $\kappa_{ex}/\kappa = 0.5$. Upper panel: transduction function for breathing mode systems is shown in blue. The optical cavity lineshape is shown in red as a guide. It can be seen clearly that K_D has maxima at $\pm\kappa/2$ and $\pm\omega_m$. Lower panel: transduction function for the Brillouin system, with $\delta\omega = \omega_m$. The scattered mode lineshape is shown in red, and the pump mode lineshape is not shown, to make clear the analogy to the canonical optomechanical system.

obvious. At critical coupling on resonance, $a_{out} = 0$. It is also worth noting that for identical system parameters, the Brillouin system has a much stronger transduction, a result of the fact that the pump field is on resonance with a cavity mode.

4.3. Optomechanical Measurements

The optomechanical measurements we perform fall broadly into two classes: steady-state frequency domain measurements, and transient time domain measurements. The simplest optomechanical measurement is identical to the mechanical mode measurement, and is a frequency domain measurement. As the power of the laser pump increases, so does the optomechanical coupling, which modifies the mechanical susceptibility, in accordance with equation 2.55. Measuring the modification of $S_{xx}(\omega)$

as the laser power is increased gives information about the optomechanical interaction, specifically the cooperativity C, as the linewidth of the thermally driven mechanical mode is $\Gamma_m = \gamma(1 + C)$ (equation 2.57).

4.3.1. Optomechanically Induced Transparency

A more sophisticated frequency domain optomechanical measurement is a form of pump-probe interference spectroscopy that is highly analogous to electromagnetically induced transparency (EIT), and is referred to as optomechanically induced transparency (OMIT), or in the case of Brillouin scattering, Brillouin scattering induced transparency (BSIT). The OMIT and BSIT signatures can measure the detuning of the laser from the sideband and optical linewidth in addition to the cooperativity C.

The pump-probe configuration for an OMIT measurement is shown in figure 4.6. The pump laser, with frequency ω_L, is tuned near the red sideband of the optical mode, $\Delta \approx -\omega_m$. A weak probe laser with frequency ω_p is then swept across the optical resonance. The linearized optomechanical equations of motion that describe the experiment are

$$\dot{a} = \left(i\Delta - \frac{\kappa}{2}\right) a - igb + \sqrt{\kappa_{ex}} a_{in} e^{-i(\omega_p - \omega_L)t} \tag{4.12}$$

$$\dot{b} = \left(-i\omega_m - \frac{\gamma}{2}\right) b - iga. \tag{4.13}$$

If the driving term looks funny, recall that the linearized equations are written in a frame where a rotates at frequency ω_L. It is perhaps also easy to confuse at this point that the term Δ in this equation refers to the pump detuning $\Delta = \omega_L - \omega_c$, **not** the detuning of the probe. We can eliminate the explicit time dependence in the coupled

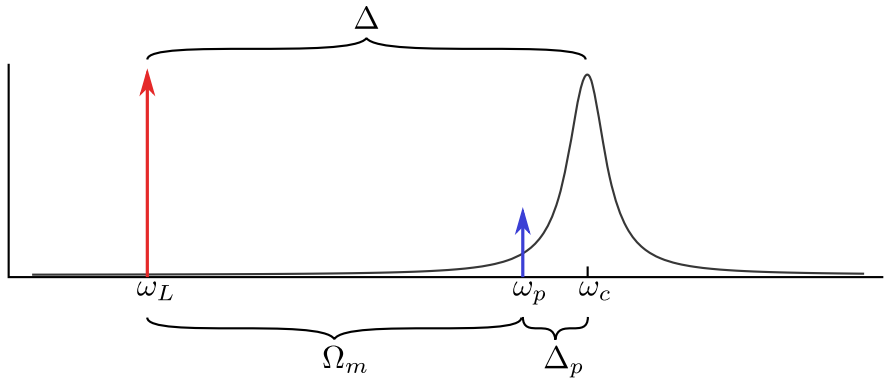

FIGURE 4.6. Optical pump and probe for OMIT experiment. The pump is tuned to the red sideband, and the probe signal is swept through the optical resonance. When $\omega_p - \omega_s = \omega_m$, the optical probe field transmission goes to 1, even when the system is critically coupled and the probe should be absorbed by the cavity.

equations by making the replacements $a \to ae^{-i(\omega_p-\omega_L)t}$ and $b \to be^{-i(\omega_p-\omega_L)t}$, leading to the equations

$$\dot{a} = \left(i\Delta_p - \frac{\kappa}{2}\right) a - igb + \sqrt{\kappa_{ex}} a_{in} \tag{4.14}$$

$$\dot{b} = \left(i\Delta' - \frac{\gamma}{2}\right) b - iga, \tag{4.15}$$

where $\Delta_p = \omega_p - \omega_c$ and $\Delta' = \Delta_p - \omega_m - \Delta$. The steady-state values of the system are determined by setting all time derivatives to zero. The steady-state optical field is found to be

$$\bar{a} = \frac{\sqrt{\kappa_{ex}} a_{in}}{\frac{\kappa}{2} - i\Delta_p + \frac{g^2}{\frac{\gamma}{2} - i\Delta'}}. \tag{4.16}$$

To make some headway on this expression, we consider the situation where the probe is near the optical resonance, by making the approximation $\kappa/2 - i\Delta_p \approx \kappa/2$, and assuming that the pump is near the red sideband, so that $\Delta_p' \approx \Delta_p$. In order to examine how the optomechanical interaction modifies the probe field, we define the

normalized field

$$\bar{a}_n = \frac{\bar{a}}{\bar{a}_0}, \tag{4.17}$$

where

$$\bar{a}_0 = 2\sqrt{\kappa_{ex}} a_{in}/\kappa \tag{4.18}$$

is the steady-state field on resonance when there is no optomechanical interaction ($g = 0$). The normalized field is found to be

$$\bar{a}_n = \frac{\frac{\gamma}{2} - i\Delta_p'}{\frac{\gamma}{2}(1+C) - i\Delta_p'} \tag{4.19}$$

which corresponds to a Lorentzian dip with linewidth

$$\Gamma_{omit} = \frac{\gamma}{2}(1+C) \tag{4.20}$$

and dip depth

$$|a_n(\Delta_p' = 0)|^2 = \left(\frac{1}{1+C}\right)^2. \tag{4.21}$$

Figure 4.7 shows the functional form of $\bar{a}_n$.

We use a phase modulation technique to measure the OMIT signal. The probe field is generated from the pump by phase modulating the pump laser with an EOM, and the phase modulation frequency is swept. While only the upper modulation sideband is swept through the optical resonance, one must keep track of the lower sideband as well to understand the measured signal. The total input field at the optical cavity is

$$a_{tot} = a_{pump} - a_{in}e^{-i\Omega_m t} + a_{in}e^{i\Omega_m t}, \tag{4.22}$$

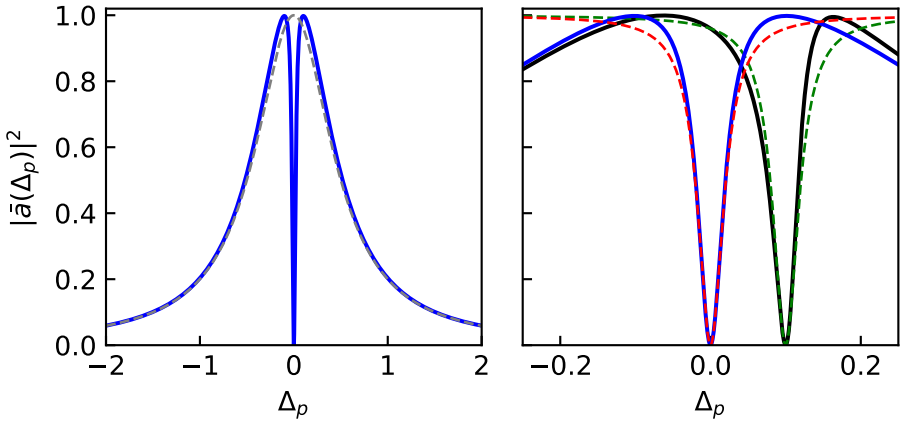

FIGURE 4.7. Lineshape for optomechanically induced transparency with a cooperativity of $C = 10$. The sideband resolution is $\omega_m/\kappa = 10$. Left panel: OMIT signal for $\Delta = \omega_m$ in blue, and the optical lineshape (OMIT signal with $g = 0$) in dashed grey. Right panel: Blue is a zoom-in of the left panel. Black is the OMIT signal with $\Delta + \omega_m = .1\kappa$. The dashed lines are the approximate forms of equation 4.19.

where Ω_m is the modulation frequency, and the field is written in a frame rotating at the pump frequency. In the resolved sideband regime, and for $\Delta \approx \omega_m$, the terms a_{pump} and $a_{in}e^{i\Omega_m t}$ are far from the optical resonance, and are therefore not modified by the cavity. The total output field is then

$$a_{out} = a_{pump} + a_{in}e^{i\Omega_m t} - (a_{in} - \sqrt{\kappa_{ex}}\bar{a})e^{-i\Omega_m t}. \tag{4.23}$$

The output is measured on a photodetector and sent to the spectrum analyzer. The signal measured by the analyzer at frequency Ω_m is

$$v_{omit} = G_D\kappa_{ex}|a_{pump}|^2|\bar{a}(\Delta_p = \Delta + \Omega_m)|^2, \tag{4.24}$$

where G_D is the photodetector gain. The phase modulation measurement is therefore directly proportional to the intracavity probe intensity $|\bar{a}|^2$.

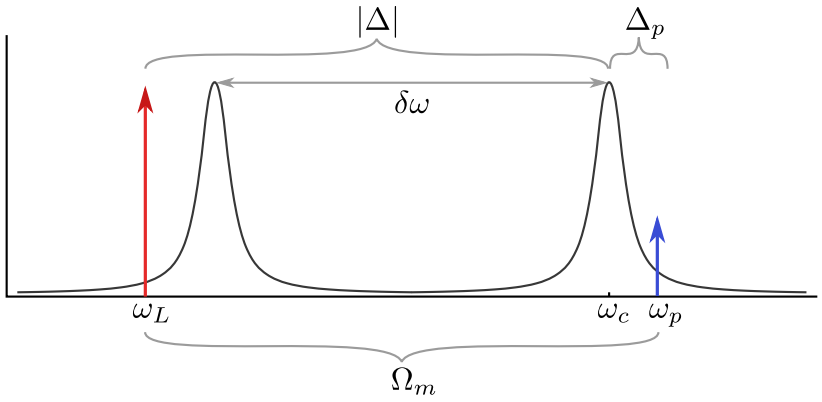

FIGURE 4.8. Definitions of the parameters for the BSIT experiment. The probe field ω_p is a distance Ω_m away from the pump ω_L. The sideband detuning of the laser from the scattered mode is Δ, and the detuning of the probe from the scattered mode is Δ_p. The detuning of the pump laser from the pump mode is $\Delta_L = \Delta + \delta\omega$.

The procedure for characterizing the optomechanical system is then to perform the OMIT measurement, and normalize the resulting signal to values between 0 and 1. A measurement of the dip width or depth determine C, and the offset of the dip with respect to the peak of the broader Lorentzian peak gives the detuning of the pump from the sideband resonance (the dip is centered at $\Delta_p' = \Delta_p - (\Delta + \omega_m) = 0$, where $\Delta + \omega_m$ is the sideband detuning, while the broad Lorentzian peak is centered at $\Delta_p = 0$). Finally, the broad Lorentzian gives an independent measure of the optical linewidth κ, as can be seen from equation 4.16 for $\Delta_p \gg \gamma$, or by simply taking $g = 0$.

One must proceed with caution when considering the corresponding BSIT measurement. The linearized optomechanical equations are the same, and therefore the expression for $\bar{a}$ is identical. The problem arises when performing the phase modulation measurement, where now the phase of a_{pump} at the output of the cavity is strongly modified by the presence of the pump optical mode. A schematic of the pump probe setup with relation to the two optical modes is depicted in figure 4.8.

If we again denote the total input field as in equation 4.22, the output field is now

$$a_{out} = (a_{pump} - \sqrt{\kappa_{ex,L}}\alpha) + a_{in}e^{i\Omega_m t} - (a_{in} - \sqrt{\kappa_{ex}}\bar{a})e^{-i\Omega_m t}, \tag{4.25}$$

where $\kappa_{ex,L}$ is the coupling rate of the pump laser into the pump mode, and α is the intracavity pump field

$$\alpha = \frac{\sqrt{\kappa_{ex,L}}a_{pump}}{\frac{\kappa_L}{2} - i\Delta_L}, \tag{4.26}$$

where κ_L is the linewidth of the pump mode, and $\Delta_L = \Delta + \delta\omega$ is the detuning of the pump laser from the pump mode (see figure 4.8). The signal measured by the spectrum analyzer at frequency Ω_m becomes

$$v_{bsit} = G_D\kappa_{ex_L}\left\{4\mathrm{Im}[\alpha]^2 + \kappa_{ex}|\alpha|^2|\bar{a}|^2 + 4\mathrm{Im}[\alpha]\sqrt{\kappa_{ex}}\mathrm{Re}[\alpha^*\bar{a}]\right\}, \tag{4.27}$$

which reduces to equation 4.24 when α is real, as is the case when the pump mode doesn't exist (or when the detuning $\Delta_L \to \infty$). In general, however, the presence of the pump mode has a significant impact on the functional form of the detected signal, as shown in figure 4.9. Figure 4.10 provides an exemplary BSIT spectrum, including least-squares fitting to the data, and the spectrum of $\bar{a}$ that is extracted from the fit parameters.

4.3.2. Transient Light Storage

The time-domain optomechanical measurement we use is a two-step process. In the first step, the mechanical mode is prepared in a coherent state through the optomechanical interaction. In the second step, after a time delay, the remaining energy in the mechanical coherent state is measured. We refer to the first step as the excitation (since we are optomechanically exciting a mechanical oscillation), and

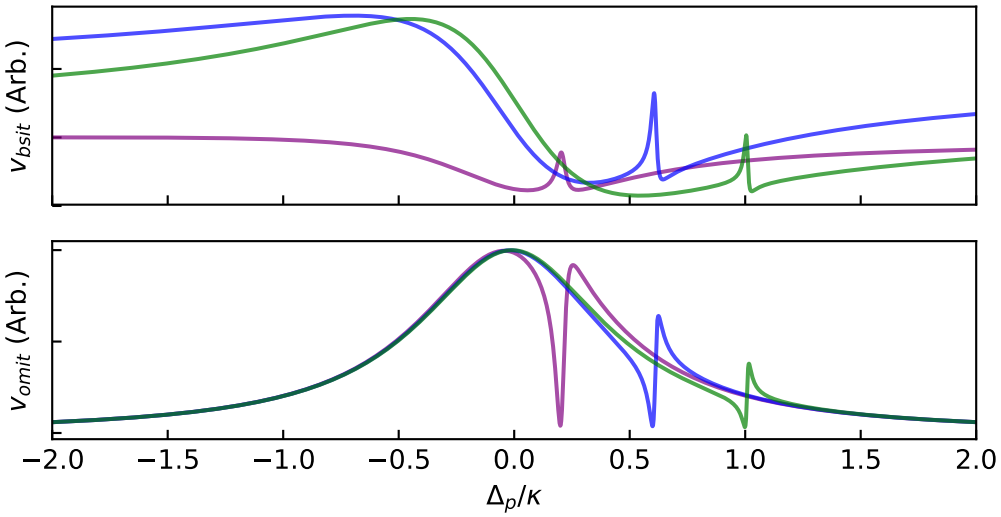

FIGURE 4.9. Comparison of OMIT and BSIT detection. Top: The BSIT phase modulation detection signal for $\Delta/\kappa = .2$ (purple), .6 (blue), and 1 (green). Both cavities have the same linewidth and are critically coupled. Bottom: the OMIT phase modulation detection signal with the same parameters.

the second step as the coupling (corresponding to the situation where the system is allowed to freely evolve under the optomechanical coupling). Each step of the process is easily understood in terms of the basic optomechanical interaction.

In the first step, the mechanical mode is prepared in a coherent state by driving the cavity with a strong red sideband pump, and a weak probe tuned on the optical resonance. This is exactly the same configuration as was used for the OMIT and BSIT measurements. The steady-state mechanical amplitude can by calculated from 4.15, and is given by

$$\bar{b} = \frac{-ig\bar{a}}{\frac{\gamma}{2} - i\Delta'}, \tag{4.28}$$

where $\bar{a}$ is given by 4.16. Plugging in $\bar{a}$ and simplifying gives

$$\bar{b} = \frac{-i\sqrt{\kappa_{ex}}a_{in}}{g}\frac{C}{1+C}, \tag{4.29}$$

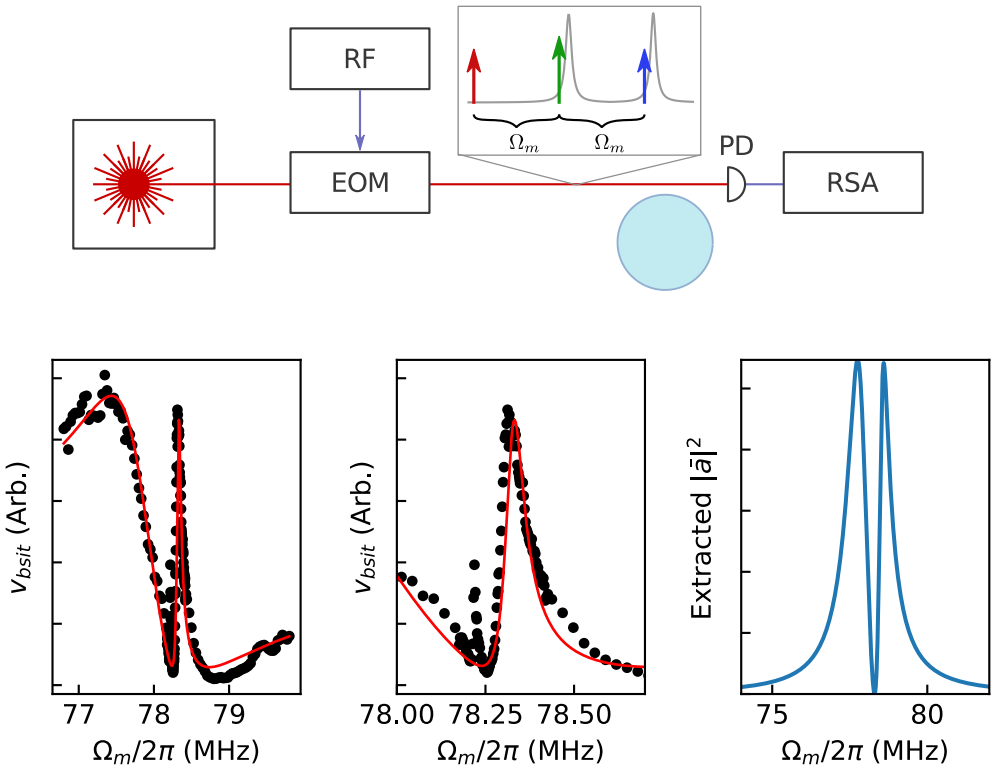

FIGURE 4.10. BSIT spectroscopy experimental setup and data. Top: Experimental setup for OMIT and BSIT measurements. Bottom: Exemplary data from a BSIT measurement. Left: Broad spectrum shows the distorted lineshape of the optical mode, with a sharp peak in the middle corresponding to the BSIT interaction. Data fit is shown in red, with best-fit parameters $C = 15$, $\Delta_L/2\pi = .42$ MHz, $\Delta_L/\kappa_L = .33$, $\kappa/2\pi = 1.33$ MHz, and $\delta\omega/2\pi = 78.22$ MHz. The mechanical mode has a frequency $\omega_m/2\pi = 78.30$ MHz and linewidth $\gamma/2\pi = 4$ kHz, corresponding to $Q = 18700$. Middle: A zoom-in of the left spectrum, showing in detail the sharp BSIT spike. Right: A plot of $\bar{a}$ using the best-fit parameters from the data.

where a_{in} is the probe, and we assume the probe is on resonance $\Delta_p = 0$ and the pump is on the red sideband $\Delta' = 0$. Equation 4.29 shows that under the optomechanical interaction, the mechanical mode is driven into a coherent state proportional to the amplitude of the probe. The process can be understood physically as a competition between the direct beating of the pump and probe at frequency ω_m which tends to excite the mechanical mode proportional to a_{in}, and the tendency for the pump laser to optomechanically damp out the mechanical motion, resulting in the $1/g$ dependence. When the pump and probe are turned off, the mechanical motion decays at rate γ. In the second step, when the optomechanical interaction is turned on again at a later time without the probe, the mechanical motion is damped at rate $\Gamma = \gamma(1 + C)$. Thus, a measurement of the damping can be used to determine C.

The time evolution of a and b in the light storage measurement are depicted in figure 4.11. The optically detected signal is sent to the spectrum analyzer, which is set to measure the optical beat frequency at ω_m as a function of time. This detected signal is a homodyne of the portion of the pump that doesn't undergo optomechanical scattering with the portion that does, and so the detected signal is directly proportional to the intracavity optical field. The energy stored in the mechanical mode at the beginning of the interaction is proportional to the area under the optically detected signal, which is highlighted in blue in the figure. Note that the decay rate of the optical field is identical to that of the mechanical mode. A fit of the optical decay provides a measurement of the total mechanical damping rate $\Gamma = \gamma(1 + C)$, as shown in figure 4.12.

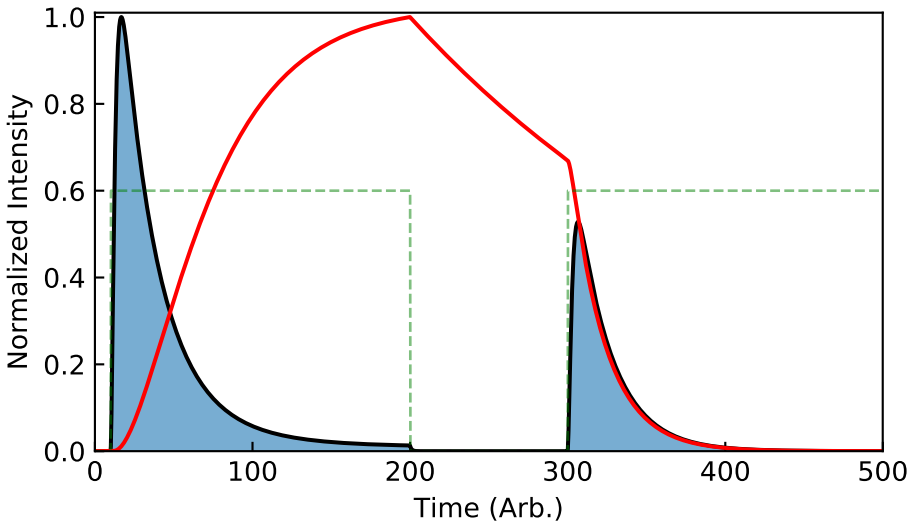

FIGURE 4.11. Light storage system evolution. The time evolution of $|a|^2$ (black) and $|b|^2$ (red) in the light storage measurement with $C = 10$. The curves are generated by integrating equations 4.14 and 4.15, and are normalized to 1 for readability. The homodyne detected signal is directly proportional to the optical field, and the energy of the mechanical mode is proportional to the area under the detected signal, highlighted in blue. The dashed green line indicates the optomechanical coupling.

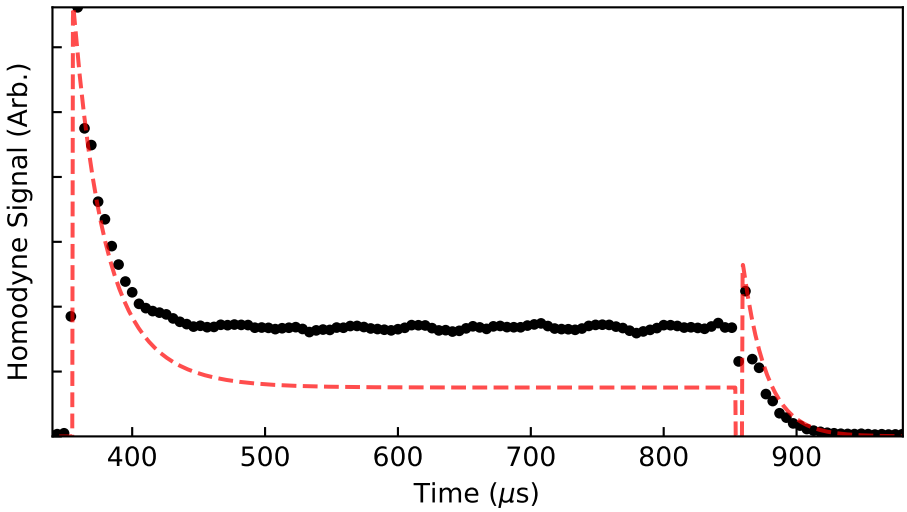

FIGURE 4.12. Light storage data (black dots) and numerical model using fit parameters from the data (red dashes). The total damping rate Γ is measured by fitting the coupling decay to a single exponential, and found to have a value $\Gamma/2\pi = 9$kHz. An independent measurement of the mechanical linewidth gave $\gamma/2\pi = 3$kHz, leading to a cooperativity of $C = 2$, the value used in the integration of the coupled optomechanical equations leading to the dashed curve. The dashed curve is normalized to the maximum value of the detected signal, and no other fit parameters are used.

CHAPTER V

MECHANICALLY DARK MODE

This chapter is based on work coauthored by Chunhua Dong, Victor Fiore, and Hailin Wang. The manuscript was published in Science [13].

5.1. Introduction

Thermal mechanical motion hinders the use of a mechanical system in applications such as quantum information processing. Whereas the thermal motion can be overcome by cooling a mechanical oscillator to its motional ground state, an alternative approach is to exploit the use of a mechanically dark mode that can protect the system from mechanical dissipation. We have realized such a mechanically dark mode by coupling two optical modes in a silica resonator to one of its mechanical breathing modes in the regime of weak optomechanical coupling. The dark mode, which is a superposition of the two optical modes and is decoupled from the mechanical oscillator, can still mediate an effective optomechanical coupling between the two optical modes. We show that the formation of the dark mode enables the transfer of optical fields between the two optical modes. Optomechanical dark mode opens the possibility of using mechanically mediated coupling in quantum applications without cooling the mechanical oscillator to its motional ground state.

The dark mode considered in this chapter is a mechanically dark mode, as discussed in Section 2.6. In terms of the bright mode (a_B) and dark mode (a_D), the system Hamiltonian is

$$H = \omega_m \left(b^\dagger b + a_B^\dagger a_B + a_D^\dagger a_D \right) + \tilde{G} \left(a_B^\dagger b + a_B b^\dagger \right), \tag{5.1}$$

where $\tilde{G} = \sqrt{g_1^2 + g_2^2}$ is the bright mode coupling rate, and the bright and dark modes are defined by Equations 2.77 and 2.78 respectively. In the limit of ultrastrong optomechanical coupling, for which g_1 and g_2 far exceed the optical loss rates κ_1 and κ_2, the dark mode becomes spectrally separated from the bright mode. In this limit, the coupling between the bright mode and the mechanical oscillator leads to the formation of two normal modes with frequencies given by $\omega_m \pm \tilde{G}$.

In the limit of weak optomechanical coupling, the dark mode can no longer be spectrally separated from the bright mode. The system, however, can still be driven optically into the dark mode via suppression of the bright-mode excitation. In contrast to the dark mode, an optical excitation of the bright mode induces a mechanical excitation. Anti-Stokes scattering of the strong driving field off this mechanical excitation in turn generates an optical field that interferes destructively with the optical excitation field in the bright mode. This OMIT process can effectively prevent the excitation of the bright mode. Specifically, when the optomechanical system shown in Fig. 5.1 is excited by a signal field resonant with mode 1, the OMIT suppresses the bright-mode amplitude by a factor of $1 + \tilde{C}$, where $\tilde{C} = C_1 + C_2$, with $C_i = 4g_i^2/\kappa_i\gamma_m$ $(i = 1, 2)$ being the optomechanical cooperativity. For simplicity,$\kappa_1 = \kappa_2$ is also assumed.The ratio of dark- to bright-mode population in the steady state is then given by $(g_2/g_1)^2(1 + \tilde{C})^2$. Hence, a large cooperativity is sufficient in preventing the excitation of the bright mode via OMIT,effectively driving the system into the dark mode. Similar results can also be obtained when $\kappa_1 \neq \kappa_2$, with the dark-to-bright-population ratio modified as $(g_2/g_1)^2 \left[1 + C_2 + C_1(\kappa_1/\kappa_2)\right]^2$. In a typical optomechanical system, the optical linewidth is orders of magnitude greater than the mechanical linewidth. It is thus more practical to realize large cooperativity than ultrastrong coupling.

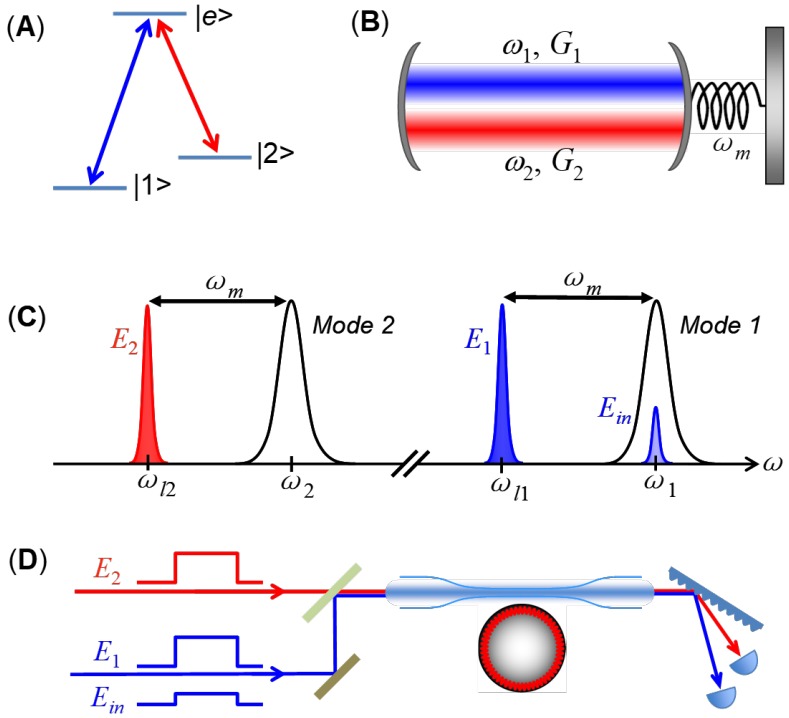

FIGURE 5.1. Concept of the experiment. (A) A Λ-type three-level system that can lead to the formation of a dark state. (B) An optomechanical system in which two optical modes couple to a machanical oscillator via radiation pressure, with respective optomechanical coupling rates G_1 and G_2. (C) Two optical fields, E_1 and E_2, at the red side band of the respective optical resonance drive the respective optomechanical coupling. (D) A simplified shematic of the experimental setup, with $E_{\rm in}$ exciting mode 1 in a silica microsphere.

The dark mode can be probed through the excitation of the two individual optical modes. In the above case, the intracavity field amplitudes of mode 1 and mode 2 are, respectively,

$$a_1 = a_0 \left[C_1/(1+\tilde{C}) + C_2 \right] /\tilde{C} \tag{5.2a}$$

$$a_2 = a_0 \sqrt{C_1 C_2} \left[1/(1+\tilde{C}) - 1 \right] /\tilde{C} \tag{5.2b}$$

where a_0 is the field amplitude in mode 1 in the absence of optomechanical coupling. In both equations, the first term in the bracket is due to the bright mode,and the second term is due to the dark mode. As expected from the suppression of the bright-mode amplitude by OMIT, the bright-mode term scales with $1/(1+\tilde{C})$. Equation 5.2B also shows that the bright- and dark- mode contributions interfere destructively in mode 2. In this context, the excitation of mode 2 results directly from the suppression of the bright-mode amplitude.

5.2. System

We used silica microspheres with a diameter near 30 μm as a model optomechanical resonator [26]. Two WGMs, with mode 1 near 637 nm and mode 2 near 800 nm, coupled to the (1, 0) mechanical breathing mode of a silica microsphere. Two samples were used, with $(\kappa_1, \kappa_2, \omega_m, \gamma_m)/2\pi \approx 19, 16, 150, 0.055$ MHz and $(\kappa_1, \kappa_2, \omega_m, \gamma_m)/2\pi \approx 15, 15, 154, 0.06$ MHz for sample A (used for Fig. 5.2) and B (used for Fig. 5.3), respectively. All experiments were carried out at room temperature.

For the demonstration of the dark mode, E_{in} with frequency ω_{in} excited mode 1 resonantly or near-resonantly. Optical emissions from mode 1 and mode 2, which are directly proportional to the respective intracavity intensity, were measured as a

function of detuning, $\Delta = \omega_{\text{in}} - \omega_{Li}$, with the phase modulation detection described in Section 4.3.1. For simplicity, we refer to these spectra as emission spectra. To avoid heating induced by the strong driving fields and to enable measurements on the bahvior or the mechanical mode, we used 8-μs-long optical pulses for E_1, E_2, and E_{in}, eacch with the same timimng and with a duty cycle below 5%. Figure 5.1D shows a simplified schematic of the experimental setup. In order to probe the steady-state behavior, emission spectra were obtained with time-gated etection, with a 1-μs detection gate positioned between 6 and 7 μs of the incident optical pulses (Fig. 5.2E inset). At relatively high optical powers, spectral shifts of WGM resonances resulting from Kerr effects become substantial. For experiments in Fig. 5.2, care was taken to keep the frequencies of the two driving fields at ω_m below the respective WGM resonances.

5.3. Results

Figure 5.2A shows emission spectra from mode 1,obtained with $C_1 = 1.4$ and $C_2 = 0$. In this case, the mechanical oscillator couples only to mode 1. The resulting OMIT process prevents the excitation of mode 1, inducing a sharp dip at the anti-Stokes resonance, $\Delta = \omega_m$, with a width determined by $\gamma_m(1 + C_1)$ (6, 7). For our studies, C_1 was determined from theoretical fitting of OMIT dips obtained with $C_2 = 0$, whereas C_2 was similarly determined from theoretical fitting of OMIT dips obtained with $C_1 = 0$ and with mode 2 excited resonantly by an input signal field.

By turning on both E_1 and E_2, we coupled both optical modes to the mechanical oscillator. With increasing C_2, the excitation of the dark mode should lead to an increasing excitation of mode 1 and thus the vanishing of the OMIT dip for mode 1 (see also Eq. 5.2a). Figure 5.2B shows emission spectra from mode 1 obtained with

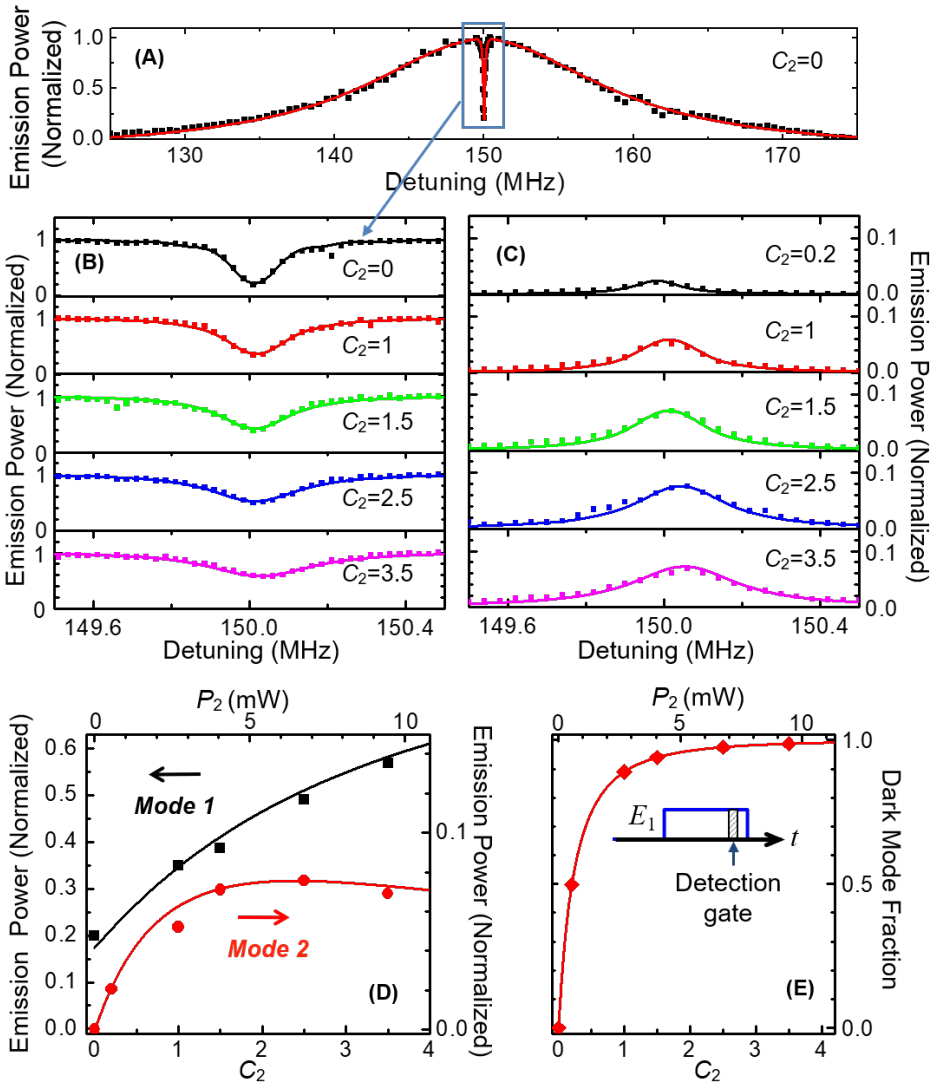

FIGURE 5.2. Excitation of the dark mode. (A and B) Optical emission from mode 1 as a function of detuning, $\Delta = \omega_{\rm in} - \omega_{L1}$, with $C_1 = 1.4$ ($P_1 = 2.5$ mW) and $P_{\rm in} = 10$ μW. The emission power is normalized to that obtained at the cavity resonance with $C_1 = C_2 = 0$. (C) Optical emission from mode 2 as a function of Δ with $C_1 = 1.4$ and $P_{\rm in} = 20$ μW. Care was taken in normalizing the emission power to the input signal power. (D) Emission powers from mode 1 (squares) and mode 2 (circles) at $\Delta = \omega_m$ as a function of C_2, derived from (B) and (C). Solid lines in (A) to (D) are the theoretical calculations discussed in the text. (E) Calculated dark-mode fraction. The diamonds correspond to the experimental results shown in (D). (Inset) The timing of the detection gate used for the experiment. $P_{\rm in}$, P_1, and P_2 are incident optical powers for $E_{\rm in}$, E_1, and E_2, respectively.

$C_1 = 1.4$ and with increasing C_2. The depth of the dip at $\Delta = \omega_m$ decreases with increasing C_2, accompanied by a spectral broadening of the dip. Figure 5.2B also shows a slight spectral shift of the emission dip at relatively high C_2. The shift is due to the optical spring effect, for which radiation pressure induces a shift in ω_m.

The dark-mode formation necessitates the conversion of optical fields from mode 1 to mode 2, because E_{in} couples directly only to mode 1. Figure 5.2C shows the emission spectra from mode 2 obtained under nearly the same condition as that for Fig. 5.2B. At $\Delta = \omega_m$, the emission from mode 2 increases simultaneously with the emission from mode 1 with increasing, but still relatively small C_2 (Fig. 5.2D), which is a signature that the system is driven toward a dark mode.

For energy conservation, the optical mode conversion should induce a dip in the emission spectrum of mode 1. A pronounced dip in the emission spectra of mode 1 persists even at the highest C_2 used (Fig. 5.2B). Under these conditions the system is nearly completely in the dark mode. With increasing C_2, the dip in the emission spectra of mode 1 evolves from an OMIT dip (at $C_2 = 0$) into a dip that reflects the process of optical mode conversion.

For a quantitative analysis, we used the coupled oscillator model to describe the coupling between the mechanical oscillator and the two optical modes (24). The solid curves in Fig. 5.2, A to C, show the calculated emission spectra from mode 1 and mode 2, with all parameters determined directly ($\kappa_1, \kappa_2, \omega_m, \gamma_m$) or indirectly ($C_1, \eta_1\eta_2 = 0.16$) from experiments, with η_1 and η_2 being the output coupling ratio for the two optical modes. Figure 5.2D plots the calculated emission power at $\Delta = \omega_m$ for the two optical modes. Additional theoretical calculations also confirm that the experimental results shown in Fig. 5.2 reflect the steady-state behavior of the optomechanical system (24).

The agreement between experiment and theory shown in Fig. 5.2, A to D, enables us to determine the dark-mode fraction (the ratio of the dark-mode population over the total bright- and dark-mode population) by using the coupled oscillator model. The steady-state dark-mode fraction corresponding to the experimental results in Fig. 5.2D is calculated and plotted (Fig. 5.2E). With $C_1 = 1.4$ and $C_2 = 3.5$, the dark-mode fraction reaches 99%.

The excitation of the dark mode not only leads to the simultaneous rise of optical emissions from mode 1 and mode 2 with increasing (but relatively small) C_2, as discussed earlier, but also accounts for the saturation of the optical mode conversion observed at relatively large C_2. As shown in Fig. 5.2D, after the system is driven into a predominantly dark mode, a further increase in C_2 leads to a saturation and then decrease in the emission from mode 2, whereas the emission from mode 1 continues to rise.

Dark-mode formation can enable efficient transfer of optical fields between the two optical modes. The overall photon-conversion efficiency, defined as the ratio of the output-signal photon flux for mode 2 over the input-signal photon flux for mode 1, is given by $\chi = 4\eta_1\eta_2 C_1 C_2/(1 + C_1 + C_2)^2$ [27, 28]. Near-unity photon conversion can thus be achieved in the limit that $C_1 = C_2 \gg 1$ and $\eta_1 = \eta_2 = 1$. With $C_1 = C_2 \gg 1$, the dark mode features nearly equal photon populations in the two optical modes. Unity photon conversion can occur because a destructive interference prevents the escape of photons from mode 1 [27]. The small output-coupling ratio ($\eta_1\eta_2 = 0.16$), along with the modest cooperativity used in our experiment, leads to the relatively small mode-conversion efficiency observed in Fig. 5.2.

The optical-mode conversion can also be described theoretically and completely with a scattering matrix approach and without resorting to the dark-mode concept

[29, 30]. In this approach, the condition of $C_1 = C_2 \gg 1$ can be understood simply in terms of impedance matching [29]. By establishing a close connection between the weak and strong coupling regime, the dark-mode description provides important insights on why the mode-conversion process can be robust against thermal mechanical noise even in a weak coupling regime.

We further characterized the emission from mode 2 by measuring directly in the time domain the heterodyne signal that mixes the emission from mode 2 with a driving field E_2. Figure 5.3 shows the transient heterodyne signal obtained with $C_1 = 0.25$ and $C_2 = 0.4$. The rise of the heterodyne signal with a rise time of order $1/\left[(1 + C_1 + C_2)\gamma_m\right]$ in good agreement with the theoretical calvulation based on the coupled oscillator model and on the use of the experimentally determined C_1, C_2, and γ_m. The heterodyne signal features a periodic oscillation with a frequency given by ω_m (Fig. 5.3 inset), demonstrating the coherent nature of the optical mode conversion. Specifically, there is a well-defined relative phase between E_2 and the converted optical field in mode 2.

We now turn to the behavior of the mechanical oscillator, which can serve as a probe for the OMIT process for the bright mode when the optical excitation is dominated by the dark mode. As discussed earlier, the OMIT arises from anti-Stokes scattering of the driving fields off the mechanical excitation induced by the bright mode excitation. To probe the mechanical excitation, we added a weak 3-ms probe pulse, which arrives 1 ms after E_1 and is also at the same frequency as E_1 (Fig. 5.4 inset). We used the probe pulse and time-gated detection, with the 1-ms gate positioned at the center of the probe pulse, to measure the displacement power density spectrum of the mechanical mode. The spectrally integrated area of the power density spectrum determines the average phonon number, $\langle N \rangle$ of the mechanical mode. For

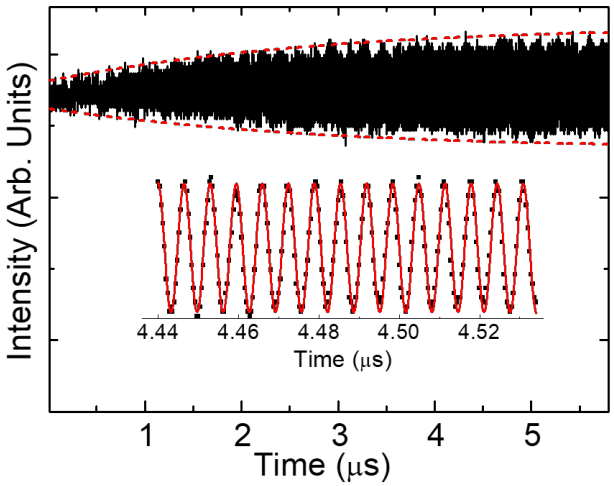

FIGURE 5.3. Heterodyne-detected optical emission from mode 2 obtained with $P_{\text{in}} = 0.1$ mW, $C_1 = 0.25$, and $C_2 = 0.4$. A driving field at the red side band of mode 2 served as the local oscillator. The dashed oine plots the calculated envelope for the heterodyne signal, with an adjustable offset. (Inset) The beat signal (squares) with an expanded time scale. Solid red line shows for reference a periodic oscillation with $\omega_m/2\pi = 154$ MHz.

the experiment, a relatively strong input signal was used such that $\langle N_0 \rangle$, the average phonon number obtained with $C_2 = 0$, is two orders of magnitude greater than the average thermal phonon number.

$\langle N \rangle / \langle N_0 \rangle$ obtained with $C_1 = 0.7$ were plotted (Fig. 5.4) as a function of C_2, for which sample A was used, and ω_{L1} and ω_{L2} were fixed and were near the respective red sideband.Other experimental conditions are the same as those for Fig. 5.2D. The experimental results are in good agreement with the theoretical calculation based on the coupled oscillator model. The calculation also includes corrections due to the Kerr effect with $\epsilon_i = \xi_i P_2$ $(i = 1, 2)$, where ϵ_1 and ϵ_2 are the Kerr shift for mode 1 and mode 2 induced by E_2, respectively, and $(\xi_1, \xi_2) =$ (-0.1, -0.46) MHz/mW. The observation of the induced mechanical excitation when the system is predominantly in the dark mode confirms the underlying OMIT process for the bright mode. Figure

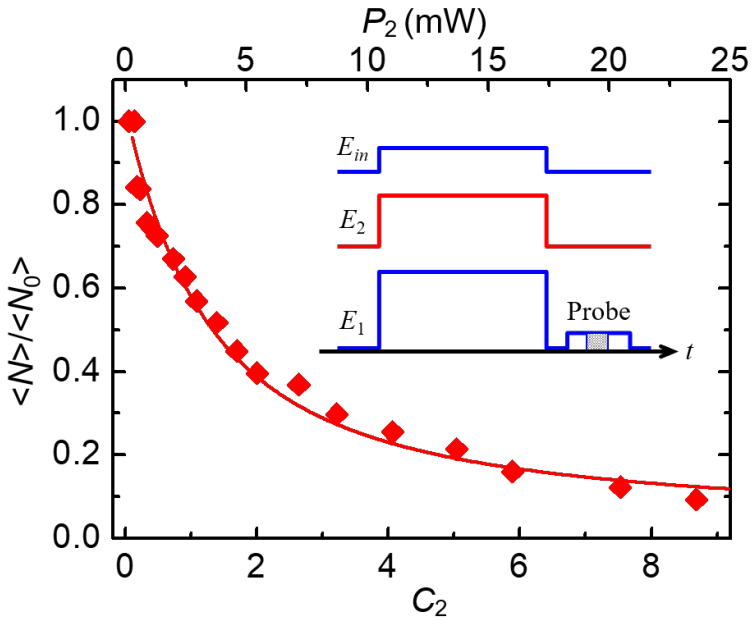

FIGURE 5.4. Induced mechanical excitation underlying the OMIT for the bright mode, obtained as a function of C_2 and with $C_1 = 0.7$ ($P_1 = 1.25$ mW) and $P_{\rm in} = 10$ μW. At $C_2 \ll 1$, $(\omega_1 - \omega_{L1})/2\pi$ and $(\omega_2 - \omega_{L2})/2\pi$ are estimated to be 150 and 145 MHz, respectively. The solid line shows the result of the theoretical calculation, as discussed in the text. (Inset) The pulse sequence used, with the shaded area indicating the timing of th edetection gate.

5.4 also shows that the anti-Stokes scattering of E_2 damps the mechanical oscillation when the system is driven to the dark mode with increasing C_2.

Although silica WGM resonators feature modest optomechanical cooperativity, much greater cooperativity (10^3 or greater) can be attained with membrane- or nanobeam-based optomechanical systems that feature ultrahigh mechanical Q factors [31, 32]. With these systems, mechanically mediated processes, such as the optical mode conversion, can be pursued in a quantum regime at an elevated temperature. The concept of the dark mode can also be extended to other hybrid mechanical systems [33, 34], including the recently developed system of a mechanical resonator coupling to a single-electron spin in a diamond NV center [35].

CHAPTER VI

OPTOMECHANICAL INTERFERENCE

This chapter is based on work coauthored by Hailin Wang. The manuscript was published in Physical Review A [23].

6.1. Introduction

Interference plays a pivotal role in quantum control of multilevel or multiqubit systems. The advances on multimode systems have thus stimulated strong interest in exploring optomechanical interference processes and in using these processes for applications such as optomechanically mediated interfaces, entanglement, and ground state cooling [27, 28, 36, 37, 38, 39]. For example, when two mechanical modes couple to a common optical mode [8, 10, 11, 12, 18, 22, 40, 41, 42], destructive interference between the respective optomechanical processes can prevent the coupling of the mechanical system to the optical mode, leading to the formation of an optically dark mechanical superposition mode [38, 41]. Similarly, a mechanically dark optical superposition mode can be formed when two optical modes couple to a common mechanical mode [27, 28]. These dark modes can be used for the realization of state transfer as well as two-mode squeezing. The dark optical mode can also be exploited to circumvent the effects of thermal mechanical noise [27, 28, 37, 38]. Evidence for dark optical and dark mechanical modes has been reported in earlier studies [13, 41], though there has been no direct experimental probe on the underlying optomechanical interference processes.

In this chapter, we report experimental demonstration of optomechanical interference in a multimode system, in which an optical mode couples to two

mechanical modes. A phase-dependent excitation-coupling approach is developed for the realization of constructive and destructive interferences. With a phase shift of π, these interference processes can effectively switch the mechanical system from an optically active to an optically dark superposition mode. Further experiments on the decay of the dark mode demonstrate directly the suppression of optically induced mechanical damping and thus the decoupling of the mechanical superposition mode from the optical mode due to the destructive interference in dynamical backactions. The interference experiments have been carried out at room temperature and above the thermal background. They can also be extended to the quantum regime. Overall, these studies establish that interference is an effective tool for controlling the interactions between light and mechanical oscillators. For the three-mode system shown in Fig. 6.1, two mechanical modes with frequencies ω_{m1} and ω_{m2} couple to an optical mode with frequency ω_0, with the optomechanical coupling driven by two strong external laser fields, E_1 and E_2, which are, respectively, ω_{m1} and ω_{m2} below the optical resonance. The interaction Hamiltonian including only resonant processes is given by

$$V_R = a^\dagger \left(e^{i\phi_1} G_1 b_1 + e^{i\phi_2} G_2 b_2\right) e^{i(\omega_s - \omega_0)t} + \text{H.c.}, \tag{6.1}$$

where b_1 and b_2 are the mechanical annihilation operators in their respective rotating frames, a is the annihilation operator for the optical mode in the rotating frame of a signal field with frequency ω_s, ϕ_1 and ϕ_2 are the initial phases of E_1 and E_2, and G_1 and G_2 are the optomechanical-coupling rates for the individual mechanical modes. Under these conditions, the mechanical system features bright and dark mechanical modes, described, respectively, by their annihilation operators,

$$b_B = \left(e^{i\phi_1} G_1 b_1 + e^{i\phi_2} G_2 b_2\right) / \sqrt{G_1^2 + G_2^2}, \tag{6.2a}$$

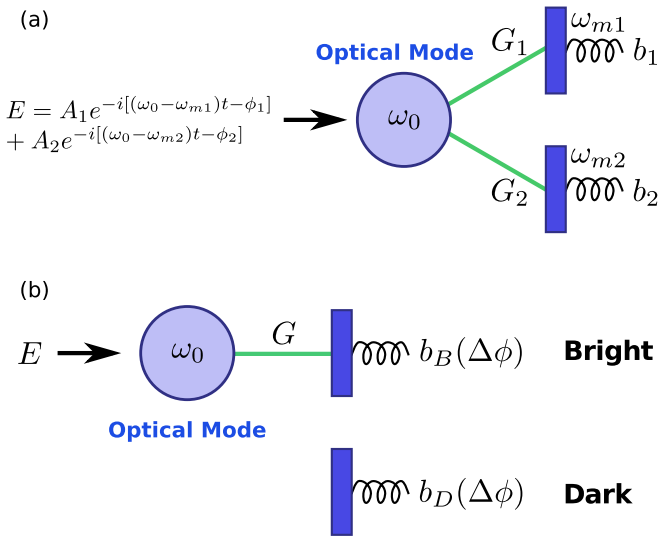

FIGURE 6.1. (a) Schematic of a multimode optomechanical system driven by two optical fields via respective red sideband couplings. (b) Interference between the two optomechanical-coupling precesses leads to the formation of dark and bright mechanical modes that depend on the relative phase of the optical driving fields, $\Delta\phi = \phi_2 - \phi_1$, with the dark mode decoupled from the optical mode.

$$b_D = \left(e^{-i\phi_1} G_1 b_1 - e^{-i\phi_2} G_2 b_2\right) / \sqrt{G_1^2 + G_2^2}. \tag{6.2b}$$

With $G_1 = G_2$, the two superposition modes in Eq. (6.2) are completely controlled by the relative optical phase, $\Delta\phi = \phi_2 - \phi_1$. In particular, by making a π phase shift in ϕ, we can turn a bright mechanical mode into a dark mechanical mode.

6.2. Experimental Setup

A silica microsphere with a diameter near 200 μm is used as a model multimode system. For our experiments, two mechanical whispering gallery (WG) modes, with frequencies $\omega_{m1}/2\pi = 69.48$ MHz and $\omega_{m2}/2\pi = 69.66$ MHz and damping rates $\gamma_1/2\pi = 3.5$ kHz and $\gamma_2/2\pi = 3.6$ kHz, are coupled to a WG optical resonance with a wavelength near 1.55 μm and with damping rate $\kappa/2\pi = 1.6$ MHz. The optomechanical interactions take place via anti-Stokes Brillouin scattering of the

optical driving fields from the mechanical modes [43, 44, 45]. The input optical power used for the weak signal field near the optical resonance is less than 0.01 mW. For the optical driving fields, the input optical powers used a range from 0.6 to 1.2 mW.

Figure 6.2 shows the experimental setup. The two optical driving fields, E_1 and E_2, are derived from a Newport velocity tunable diode laser with a wavelength near 1.55 μm. Two acoustic optical modulators (AOMs) are used to set the relative frequency and phase of the two driving fields. The weak signal field, E_s, is generated with an electro-optic modulator (EOM) from the driving field E_1 . Two rf signal generators (RF 1a and RF 1b) are used to drive the AOM that generates E_1. The outputs from RF 1a and RF 1b are first gated and then combined to generate a rf field with a phase slip at specified times. All rf generators except for RF 1b have their external references connected to the same 10 MHz clock (master clock). A second 10 MHz signal generator is also locked to the master and sends a reference signal to RF 1b. We vary the phase of the second 10 MHz generator to generate a phase slip in E_1.

Optical fields are coupled into and out of whispering gallery optical modes of the silica microsphere via a tapered optical fiber and then detected together in a silicon photodiode, whose output is sent to a real-time spectrum analyzer (SA). This detection scheme can be viewed as heterodyne detection of the emissions from the optical mode, with the two optical driving fields serving as the local oscillators. A relatively small spectral detection window (100 kHz) is used for the SA such that only a single beat frequency is measured in transient measurements. The spectral detection window limits the time resolution of the experiments to 6 μs.

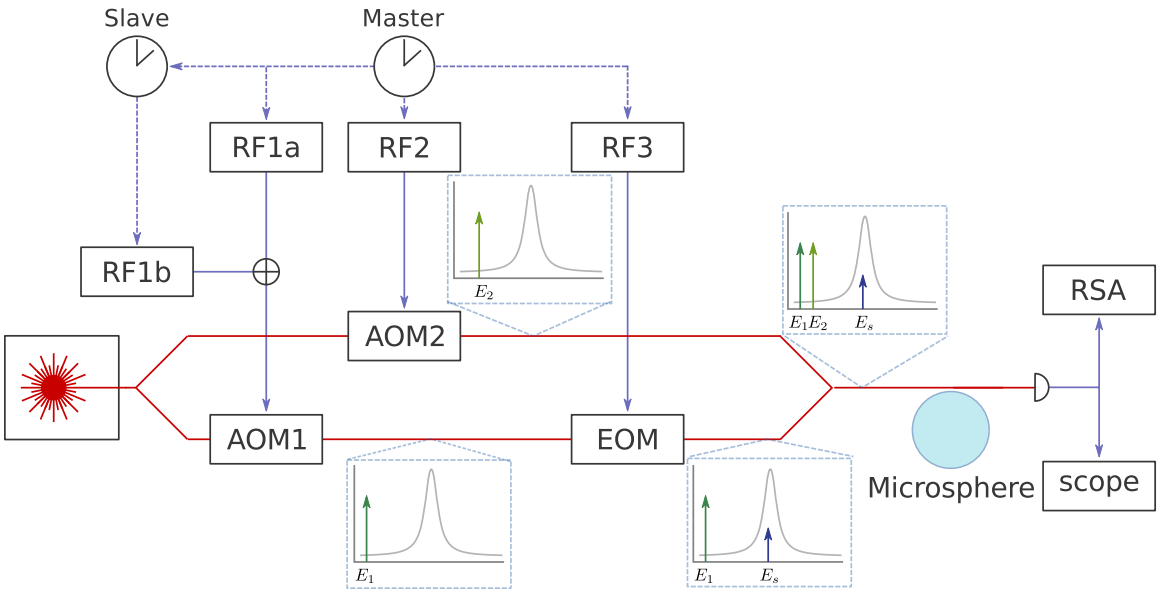

FIGURE 6.2. Optomechanical interference experimental setup. Optical fields are coupled into and out of the relevant whispering gallery optical modes in the microsphere through a tapered fiber.

6.3. Experimental Results

We have developed a phase-dependent excitation-coupling approach to probe optomechanical interactions and especially interference processes. We first illustrate this approach using a two-mode system. As shown in the inset of Fig. 6.3, a weak optical signal field, E_s, with frequency $\omega_s = \omega_0$, and an optical driving field, E_1, with frequency $\omega_1 = \omega_s - \omega_{m1}$, couple to the mechanical mode, converting the signal field in the optical mode to a mechanical excitation [46, 47, 48]. After E_s is switched off, E_1 couples to the induced mechanical excitation, converting the mechanical excitation back to optical fields. We introduce a phase slip in E_1 right after E_s is switched off. The initial phase of E_1 in the excitation stage is θ_1. The phase is then changed to ϕ_1 in the coupling stage (see Fig. 6.3).

Heterodyne-detected emissions from the optical mode, with E_1 as the local oscillator, are plotted in Fig. 6.3 as a function of time. The exponential decay

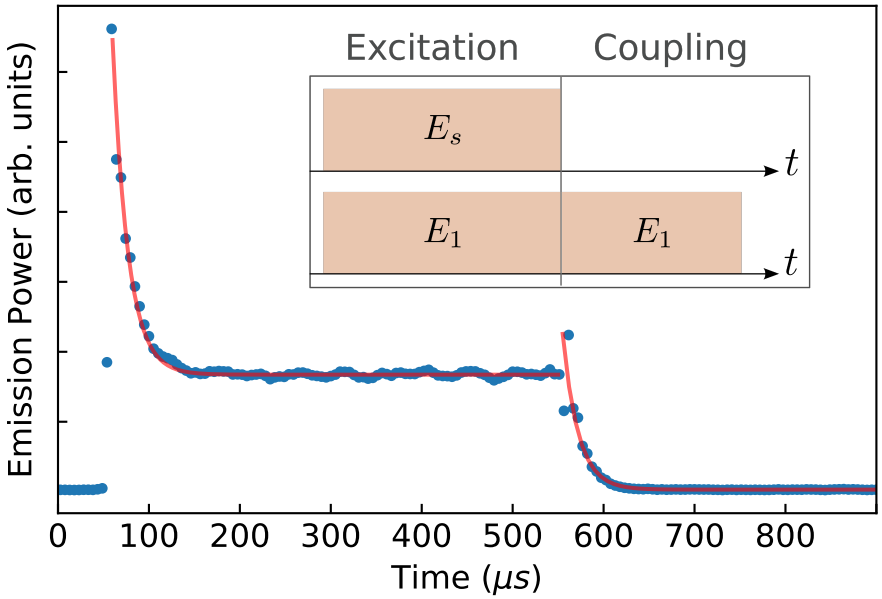

FIGURE 6.3. Characterization of 2 mode components with heterodyne detection. Heterodyne-detected emissions (blue dots) from the optical mode as a function of time in the two-mode system. Solid lines are numerical fits to single exponential decays with a decay rate of $\gamma/2\pi = 9.1$ kHz. The first decay corresponds to the increasing conversion of E_s to a mechanical excitation. The second decay corresponds to the conversion of the mechanical excitation to optical fields and the resulting mechanical damping, after E_s is switched off. The inset shows the optical pulse sequence used, with E_s (0.5 ms in duration) at ω_0 and E_1 at the red sideband of E_s.

of the emission following the leading edge of the signal pulse corresponds to the increasing conversion of the signal field in the optical mode into the mechanical excitation. The decay time, which sets the time scale for the excitation to reach steady state, is given by $1/[(1 + C_1)\gamma_1]$, where $C_1 = 4G_1^2/\gamma_1\kappa = 1.6$ is the cooperativity for the optomechanical coupling. The decrease in the emission from the optical mode in the steady state shown in Fig. 6.3 corresponds to the dip in the spectral domain optomechanically induced transparency (OMIT) experiment [48]. The exponential decay after E_s is switched off corresponds to the conversion of the induced mechanical excitation back into optical fields. With $\kappa \gg (\gamma_1, G_1)$, the dynamical backaction underlying this conversion process leads to optically induced damping of the mechanical excitation, with the total damping rate given by $(1+C_1)\gamma_1$, as confirmed in Fig. 6.3. Note that interference also plays an important role in two-mode systems through OMIT [49]. However, the underlying optomechanical coupling cannot be controlled via a phase shift in the optical or mechanical excitations. The experimental result for the two-mode system shown in Fig. 6.3 is independent of θ_1 as well as the phase slip $\phi_1 - \theta_1$.

We now extend this approach to the three-mode system, for which two optical driving fields, E_1 and E_2, with frequencies $\omega_1 = \omega_s - \omega_{m1}$ and $\omega_2 = \omega_s - \omega_{m2}$, couple the two mechanical modes to the same optical mode. The pulse sequence of the experiment is shown in Fig. 6.3(a). For simplicity, no phase slip is introduced for E_2, (i.e., $\theta_2 = \phi_2$). In the coupling stage, the induced mechanical excitation is in a bright mechanical mode when $\phi_1 = \theta_1$. The same excitation, however, is expected to be in a dark mechanical mode when $G_1 = G_2$ and θ_1 is π out of phase with ϕ_1 . In general, the mechanical excitation can be a combination of both bright and dark modes.

Heterodyne-detected emissions from the optical mode are shown in Figs. 6.3(b) and 4(c) as a function of time. A spectral filter is used such that only the heterodyne beat at frequency ω_{m1}, with either E_1 or E_2 as the local oscillator, is detected. The emissions in Fig. 6.3(b) are detected during the excitation stage of the experiment. Similar to Fig. 6.3, the decay of the emission in Fig. 6.3(b) corresponds to the increasing conversion of the signal field in the optical mode into the mechanical excitations and shows an effective cooperativity of $C = 1.4$. The emissions in Fig. 6.3(c) are obtained when E_s is switched off. In this case, the optical driving fields convert the mechanical excitations back to optical fields, leading to optically induced mechanical damping. As revealed in Fig. 6.3(c), the optomechanical-coupling process depends strongly on the phase slip $\phi_1 - \theta_1$.

The heterodyne-detected optical emission energy obtained in a time span of 0.4 ms after E_s is switched off is plotted in Fig. 6.4(d) as a function of ϕ_1. These data are derived from experiments similar to those in Fig. 6.4(c). The interference fringes observed in Fig. 6.4(d) are sinusoidal with a period of 2π . The minima and maxima in the oscillations correspond, respectively, to the dark and bright mechanical modes. The sinusoidal oscillations correspond to the switching of the mechanical system between the dark and bright modes as ϕ_1 is varied. Similar oscillations are also observed when the heterodyne beat at frequency ω_{m2} is detected.

The optomechanical interference underlying the oscillations shown in Fig. 6.4(d) occurs in a self-consistent two-step process. For the first step, E_1 and E_2 scatter from the relevant mechanical excitations, generating induced signal fields in the optical mode. Under the condition of two-photon resonance, $\omega_1 + \omega_{m1} = \omega_2 + \omega_{m2}$, the two induced signal fields are at the same frequency. For the second step, the overall induced signal field and the relevant pump field couple to an individual

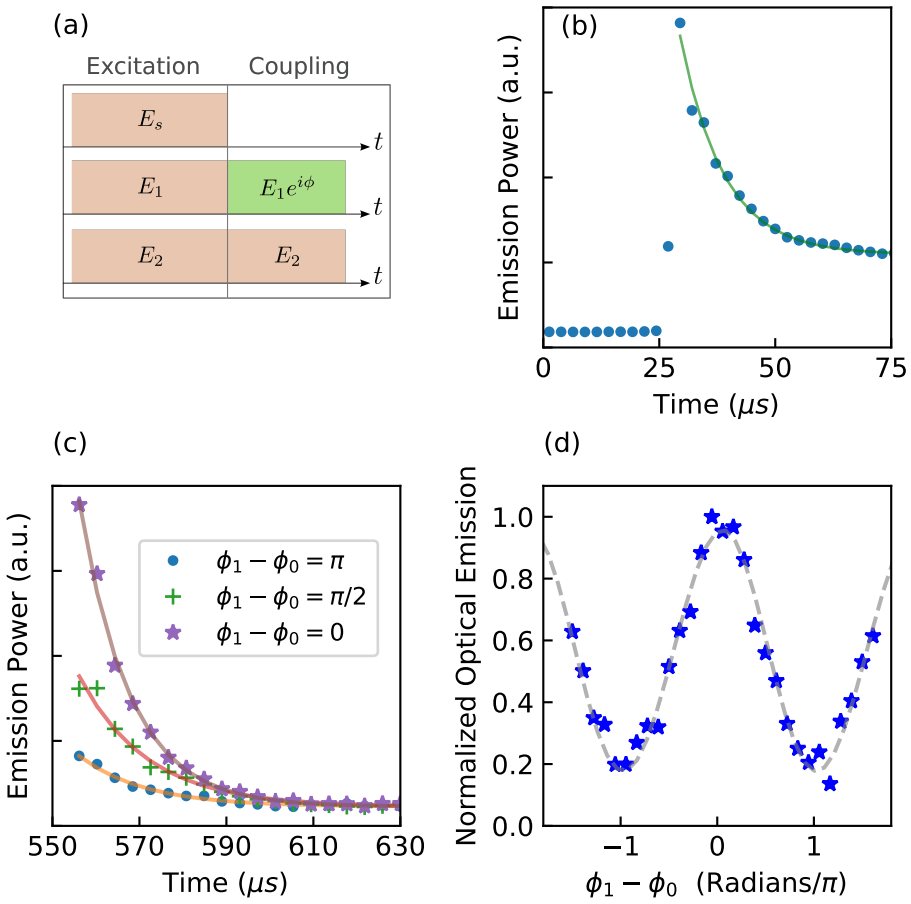

FIGURE 6.4. Demonstration of optomechanical interference. (a) Optical pulse sequence used for optomechanical interference, with E_s (0.5 ms in duration) at ω_0 and E_1 and E_2 at the respective red sidebands of E_s. (b) Heterodyne-detected emissions from the optical mode as a function of time with $\theta_2 = \phi_2$, when E_s is on. (c) Heterodyne-detected emissions from the optical mode as a function of time at various ϕ_1 with $\theta_2 = \phi_2$, $C_1 = 1.3$, and $C_2 = 1$, when E_s is off. Solid lines in (b) and (c) are numerical fits to single exponential decays. (d) The emission energy from the optical mode as a function of ϕ_1, obtained in a time span of 0.4 ms after E_s is switched off. The dashed line shows the theoretical calculation discussed in the test. ϕ_0 is an offset such that the dark mode occurs when $\phi_1 - \phi_0 = \pi$.

mechanical mode, leading to dynamical backactions, more specifically optically induced mechanical damping [50]. Optomechanical interference takes place through the interference of the induced signal fields in the dynamical backaction. Destructive and constructive interferences in the backaction lead, respectively, to the formation of dark and bright mechanical modes.

The destructive optomechanical interference effectively decouples the mechanical system from the optical mode, suppressing the optically induced mechanical damping. For a direct demonstration of the destructive interference in the dynamical backaction, we have measured the damping rate of the dark mode. For this experiment, we append a measurement stage to the pulse sequence in Fig. 6.4(a). As shown in Fig. 6.5(a), after keeping the mechanical system in the dark mode for a duration of τ, we switch the initial phase of E_1 back to θ_1. Correspondingly, the mechanical system is switched back to the bright mode. Heterodyne-detected optical emissions occurring in the measurement stage probe directly the amplitude of the dark mode at the end of the coupling stage. The emission energy obtained for a time span of 0.4 ms in the measurement stage is plotted in Fig. 6.5(b) as function of τ . Similar to Fig. 6.4, only the heterodyne beat at frequency ω_{m1} is detected. Note that the damping rate of the bright mechanical mode can be derived from experiments similar to those in Fig. 6.4(c), in which we measure directly the heterodyne-detected optical emission as a function of time after E_s is switched off.

The damping rate for the dark mechanical mode, derived from Fig. 6.5(b), is $\gamma_D/2\pi = 7.8kHz$. In comparison, the damping rate for the bright mechanical mode obtained under otherwise the same experimental condition is $\gamma_B/2\pi = 11kHz$ [see the inset of Fig. 6.5(b)], corresponding to $C = 2.1$. The relative reduction in the optically induced mechanical damping rate due to the destructive interference is

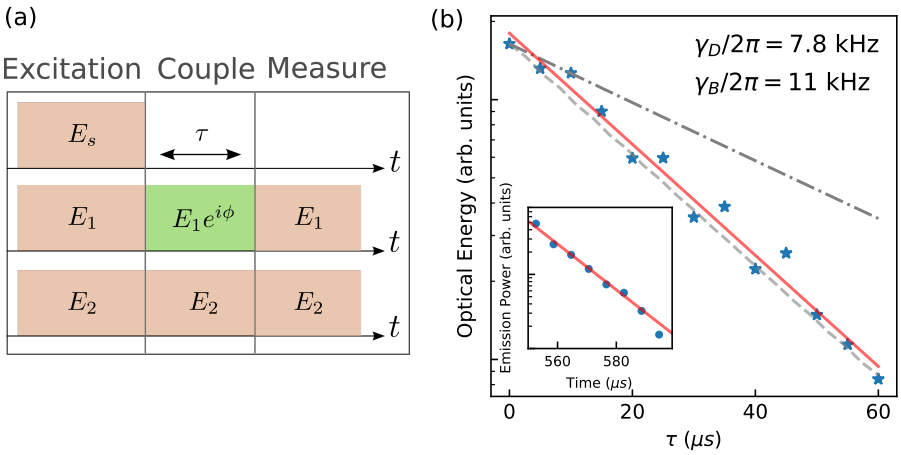

FIGURE 6.5. Protection against optically induced damping for dark modes. (a) Optical pulse sequence used to probe suppression of optically inudced mechanical damping due to destructive interference. (b) Heterodyne-detected optical imissions (the stars) from the optical mode obtained in the measurement stage as a function of τ, with $\theta_2 = \phi_2$ and $G_1 = G_2$ and with ϕ_1 adjusted such that the mechanical system is in the dark mode in the coupling stage. The dashed line shows the corresponding theoretical calculation discussed in the text. The dash-dotted line shows the theoretical calculation that includes only two-photon resonant optomechanical coupling, yielding a damping rate, $\gamma/2\pi = 3.6$ kHz. The inset shows the measurement of the bright mode decay in the coupling stage. The solid lines are numerical fits of the experimental data to single exponential decays.

$(\gamma_B - \gamma_D)/(\gamma_B - \bar{\gamma}) = 43\%$, where $\bar{\gamma} = (\gamma_1 + \gamma_2)/2$. The suppression is not complete, in part due to the slightly unequal damping rates of the two mechanical modes, and to a larger part due to optomechanical coupling processes that are not two-photon resonant. These processes include the coupling of E_1 to mechanical mode 2 and the coupling of E_2 to mechanical mode 1. These two processes do not experience destructive interference, leading to effective damping of the mechanical modes.

6.4. Theoretical Analysis

For a theoretical analysis of the experimental results, we have used the semiclassical coupled-oscillator equations, with the equations of motion given by

$$\dot{\beta}_1 = -\frac{\gamma_1}{2}\beta_1 - ie^{-i\delta t - i\phi_1}G_1\alpha, \tag{6.3a}$$

$$\dot{\beta}_2 = -\frac{\gamma_2}{2}\beta_2 - ie^{-i\delta t - i\phi_2}G_2\alpha, \tag{6.3b}$$

$$\dot{\alpha} = -\left(i\Delta + \frac{\kappa}{2}\right)\alpha - i\left(e^{i\phi_1}G_1\beta_1 + e^{i\phi_2}G_2\beta_2\right)e^{i\delta t} + \sqrt{\kappa^{ext}}A_s, \tag{6.3c}$$

where $\beta_1 = \langle\hat{b}_1\rangle$, $\beta_2 = \langle\hat{b}_2\rangle$, $\alpha = \langle\hat{a}\rangle$, $\Delta = \omega_0 - \omega_s$, and κ^{ext} is the cavity decay rate due to input-output coupling. The amplitude of the input signal field, A_s, is normalized such that $I_s = |A_s|^2$ is the photon flux. For simplicity, the above equations have assumed that the two-photon resonant con- dition is satisfied, with $\delta = \omega_s - \omega_1 - \omega_{m1} = \omega_s - \omega_2 - \omega_{m1}$, and have omitted coupling terms that are not two-photon resonant (the general equations are given in the Appendix). It is straightforward to show from Eq. (6.3) that with $\gamma_1 = \gamma_2$, the amplitude of the dark mode, $\beta_D = \langle\hat{b}_D\rangle$, is completely decoupled from the field in the optical mode.

Theoretical calculations, which include both two-photon resonant and nonresonant optomechanical couplings and use experimentally determined parameters,

are in good agreement with the experimental results on the fringe visibility shown in Fig. 6.4(d) and on the damping rate of the dark mode shown in Fig. 6.5(b). As shown in Fig. 6.5(b), the theoretical calculation that includes only two-photon resonant optomechanical coupling yields a damping rate for the dark mode, $\gamma/2\pi =$ 3.6 kHz, nearly the same as $\gamma_1/2\pi$ and $\gamma_2/2\pi$. In this regard, the residual optically induced mechanical damping for the dark mode is almost entirely due to the two-photon nonresonant couplings, which can be suppressed if the frequency separation between the two mechanical modes far exceeds the optical linewidth.

6.4.1. Two-photon Nonresonant Couplings

We consider the optomechanical coupling between two mechanical modes with frequencies ω_{m1} and ω_{m2}, and one optical mode with frequency ω_0, driven by two strong external laser fields, E_1 and E_2, which are nearly ω_{m1} and ω_{m2} below the optical resonance, respectively. In the resolved-sideband limit, the linearized optomechanical Hamiltonian that can satisfy the two-photon resonance condition, $\omega_2+\omega_{m2} = \omega_{m1}+\omega_1$, is given by

$$H_R = \Delta a^\dagger a + \left[G_1 e^{i(\omega_s-\omega_1-\omega_{m1})t+i\phi_1} a^\dagger b_1 + \text{H.c.}\right] + \left[G_2 e^{i(\omega_s-\omega_2-\omega_{m2})t+i\phi_2} a^\dagger b_2 + \text{H.c.}\right], \tag{6.4}$$

where $\hat{b}_1$ and $\hat{b}_2$ are the annihilation operators for the mechanical modes in their respective rotating frames, $\hat{a}$ is the annihilation operator for the optical mode in the rotating frame of the signal field with $\Delta = \omega_0 - \omega_s$, ϕ_1 and ϕ_2 are the initial phase for E_1 and E_2, and G_1 and G_2 are the effective optomechanical-coupling rates for E_1 coupling to mechanical mode 1 and E_2 coupling to mechanical mode 2, respectively. The above Hamiltonian does not contain optomechanical coupling terms that cannot

satisfy the two-photon resonant condition. These terms are given by

$$V_{NR} = \left[G_{12} e^{i(\omega_s - \omega_1 - \omega_{ms})t + i\phi_1} a^\dagger b_2 + \text{H.c.}\right] \tag{6.5}$$

where G_{12} and G_{21} are the effective optomechanical-coupling rates for E_1 coupling to mechanical mode 2 and E_2 coupling to mechanical mode 1. Note that the nonresonant-coupling terms become negligible if the frequency separation between the two mechanical modes far exceeds the optical cavity linewidth.

The semiclassical equations of motion including both two-photon resonant and nonresonant optomechanical interactions are given by

$$\dot{\beta}_1 = -\frac{\gamma_1}{2}\beta_1 - i\left[G_1 e^{-i(\omega_s - \omega_1 - \omega_{m1})t - i\phi_1} + G_{21} e^{-i(\omega_s - \omega_2 - \omega_{m1})t - i\phi_2}\right]\alpha, \tag{6.6a}$$

$$\dot{\beta}_2 = -\frac{\gamma_2}{2}\beta_1 - i\left[G_2 e^{-i(\omega_s - \omega_2 - \omega_{m2})t - i\phi_2} + G_{12} e^{-i(\omega_s - \omega_1 - \omega_{m2})t - i\phi_1}\right]\alpha, \tag{6.6b}$$

$$\begin{aligned}\dot{\alpha} = &-\left(i\Delta + \frac{\kappa}{2}\right)\alpha - ie^{i(\omega_s - \omega_{m1})t}\left[G_1 e^{i(\phi_1 - \omega_1 t)} + G_{21} e^{i(\phi_2 - \omega_2 t)}\right]\beta_1 \\ &- ie^{i(\omega_s - \omega_{m2})t}\left[G_2 e^{i(\phi_2 - \omega_2 t)} + G_{12} e^{i(\phi_1 - \omega_1 t)}\right]\beta_2 + \sqrt{\kappa^{ext}} A_s.\end{aligned} \tag{6.6c}$$

For a qualitative discussion, we note that the four optomechanical-coupling terms in Eq. (6.6c) generate optical fields at frequencies of $\omega_1 + \omega_{m1}$, $\omega_2 + \omega_{m2}$, $\omega_1 + \omega_{m2}$, and $\omega_2 + \omega_{m1}$ through anti-Stokes scattering. Only the two processes corresponding to $\omega_1 + \omega_{m1}$ and $\omega_2 + \omega_{m2}$ can satisfy the two-photon resonant condition. All four processes contribute to the optically induced mechanical damping, as verified by observing optically induced damping and BSIT on both modes simultaneously with only a single pump laser (Figure 6.6). For the interference experiments shown in Fig. 6.4, only the beat frequency at ω_{m1} is measured in the heterodyne detection, with either E_1 or E_2 serving as the local oscillator. Under the two-photon resonant condition, optical

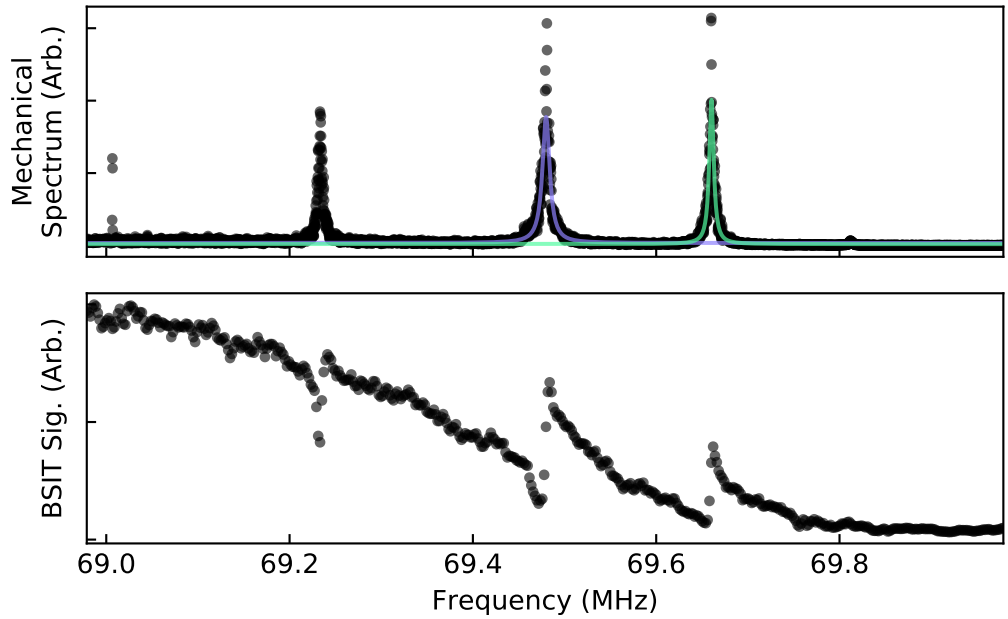

FIGURE 6.6. Mechanical mode and BSIT spectra. Top: Mechanical mode spectrum measured on the spectrum analyzer. The driving laser is tuned to maximize the optomechanical broadening of the center mode. The least-squares fits to the center mode (purple) and upper mode (green) are used to estimate the coopertivities $C_1 = 1.7$ for the middle mode, and $C_2 = .65$ for the upper mode. Bottom: A BSIT spectrum was collected to verify that all three mechanical modes are optomechanically interacting, even though the laser is detuned on the resonance of only the center mode. Three BSIT signals are clearly visible at the three mechanical mode frequencies.

fields generated by the optomechanical coupling at frequencies $\omega_1 + \omega_{m1}$, $\omega_2 + \omega_{m2}$, and $\omega_2 + \omega_{m1}$, contribute to the experiments. The field at $\omega_1 + \omega_{m2}$ does not contribute to the experiments in Fig. 6.4.

For the theoretical calculations shown in Figs. 6.4 and 6.5, we have solved Eq. (6.6) numerically using the experimentally determined parameters. To determine the relative contribution of two-photon nonresonant processes to residual optically induced mechanical damping of the dark mechanical mode, we have also calculated the dark mode decay including only contributions that are two-photon resonant.

6.5. Conclusion

In conclusion, we have successfully exploited optomechan- ical interference processes to control optomechanical inter- actions, in particular, dynamical backactions, in multimode optomechanical systems. Like its counterpart in multilevel or multiqubit systems, optomechanical interferences will play an essential role in the exploration and application of interactions between light and mechanical systems.

CHAPTER VII

TWO MODE OPTICAL ENTANGLEMENT

This work was coauthored by Steven J. van Enk and Hailin Wang. The manuscript was published in Physical Review A [24].

7.1. Introduction

Entanglement generation is often hampered by dissipation and decoherence induced by the unavoidable coupling to the environment. For generation of optical entanglement via an optomechanical process, a major obstacle is the coupling of the mechanical oscillator to the thermal reservoir. A recently proposed scheme has exploited the coherent dynamics of the Bogoliubov modes to circumvent thermal mechanical noise [37]. The thermal robustness of the Bogoliubov-mode based schemes hinges on the achievement of a large multi-photon optomechanical coupling rate that far exceeds the damping rates of the relevant optical and mechanical modes. Other entanglement schemes have also specified that optomechanical systems are deep in the strong coupling regime [38, 51, 52]. Although strong optomechanical coupling has been achieved for individual optomechanical systems in both optical and microwave regimes [53, 54, 55], it is exceedingly difficult to have the multi-photon optomechanical coupling rate to be much greater than the cavity decay rate in the optical regime, especially in a setting that is suitable for generating entanglement between optical and microwave modes. A large number of photons in an optical cavity can lead to experimental difficulties such as bistability and two-photon absorption.

In this chapter, we propose and analyze an optomechanical scheme for optical entanglement generation, which takes advantage of a special class of multi-mode

interaction Hamiltonian, instead of Bogoliubov modes, to circumvent thermal mechanical noise. This scheme is inspired by earlier theoretical and experimental studies on entangling trapped ions in a thermal environment [56, 57, 58]. In these studies, the entanglement operation takes place via the mechanical degrees of freedom of the ions. As shown by Sørensen and Mølmer, robust entanglement can be achieved in a thermal environment with a class of Hamiltonian that returns the motion of the ions to their initial state upon the completion of the entanglement operation [57, 58]. Here, we outline a pulsed entanglement scheme using an optomechanical interaction Hamiltonian that has the features of the Sørensen-Mølmer (S-M) mechanism. The entanglement scheme, which will be referred to as the Sørensen-Mølmer scheme, can function in the weak as well as strong coupling regime. In comparison with the Bogoliubov-mode based schemes, the Sørensen-Mølmer scheme can remain robust against the thermal mechanical noise even in the weak coupling regime. Our theoretical analysis shows that significant optical entanglement can be generated in the weak coupling regime, even in the presence of a large thermal phonon occupation ($n_{th} \sim 1000$).

7.2. Three-mode Optomechanical System

We consider an optomechanical system, in which two optical modes with resonance frequencies $\omega_{c,i}$ $(i = 1, 2)$ and cavity linewidths κ_i, couple to a mechanical oscillator of frequency ω_m and mechanical linewidth γ (see Fig. 7.1a). The optomechanical coupling is driven by strong laser fields of frequency $\omega_{L,i}$ near the mechanical sideband of the respective cavity resonance. This type of three-mode optomechanical systems has already been used for the experimental demonstration of optomechanics-based optical wavelength conversion [13, 14, 59] and for the realization

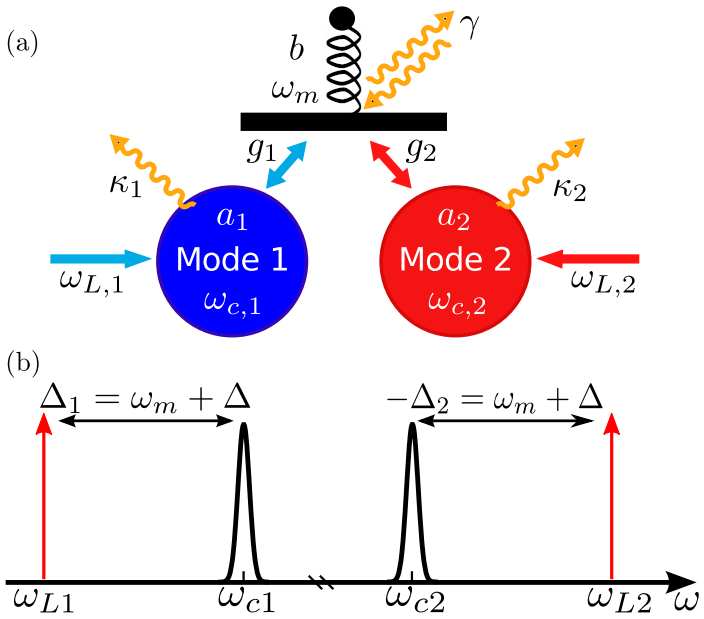

FIGURE 7.1. Schematic of three-mode system and laser drives. (a) Schematic of the three-mode optomechanical system. (b) Spectral position of the optical driving fields.

of an optomechanical dark mode [13, 41]. In a frame where each optical mode rotates at its driving frequency $\omega_{L,i}$, and after the standard linearization process, the effective Hamiltonian of the system is

$$H = \omega_m b^\dagger b + \sum_{i=1}^{2} \left(\delta_i a_i^\dagger a_i + g_i (a_i + a_i^\dagger)(b + b^\dagger) \right), \tag{7.1}$$

where b and a_i are the annihilation operators for the mechanical and optical modes, respectively, and $\delta_i = \omega_{c,i} - \omega_{L,i}$ is the detuning of the driving field from the respective cavity resonance. The effective multi-photon coupling rate g_i is controlled by the strength of the driving field according to $g_i = \sqrt{N_i} g_{0,i}$, where N_i is the intra-cavity photon number for the driving field and $g_{0,i}$ is the single-photon optomechanical coupling rate.

The linearized interaction Hamiltonian couples each optical mode to the mechanical oscillator with two types of interaction. A beam-splitter interaction,

associated with the term $g_i(a_i^\dagger b + a_i b^\dagger)$, is an anti-Stokes scattering process that can enable state transfer between optical and the mechanical systems. A two-mode squeezing interaction, of the form $g_i(a_i b + a_i^\dagger b^\dagger)$, is a Stokes scattering process that generates correlated phonon-photon pairs. The beam-splitter interaction has been used for the experimental realization of coherent inter-conversion between optical and mechanical excitations [60, 61, 62] as well as the optomechanically-induced transparency [54, 63, 64, 65] and has also been exploited for optical wavelength conversion in the three-mode optomechanical system [13, 14, 48, 59]. The two-mode squeezing interaction has been employed in earlier theoretical proposals for generating continuous variable entanglement between optical and mechanical modes and also between two mechanical modes [66, 67, 68, 69, 70, 71, 72, 73].

For the generation of two-mode optical entanglement, mode 1 is driven near the red sideband, at frequency $\omega_{L,1} = \omega_{c,1} - \omega_m - \Delta$, while mode 2 is driven near the blue side-band, at frequency $\omega_{L,2} = \omega_{c,2} + \omega_m + \Delta$, where Δ is the detuning from the sideband resonance, as illustrated schematically in Fig. 7.1b. The optomechanical system is assumed to be in the resolved sideband limit, with $\omega_m \gg \kappa_{1,2} \gg \gamma$ ($\omega_m \gg g_{1,2}$ is also assumed), such that a driving field near the red or blue sideband drives either the beam-splitter or two-mode squeezing interaction, respectively. Heuristically, entanglement between modes 1 and 2 in this system is generated in two steps. The two-mode squeezing interaction driven by the laser field near the blue sideband generates entanglement between phonons in the mechanical oscillator and photons in mode 2. The beam-splitter interaction driven by the laser field near the red sideband then maps the state of the entangled phonons onto photons in mode 1.

In the resolved sideband limit, the classical driving fields reach steady state on the time scale $1/\omega_m$, after which time the linearized Hamiltonian can be used. The entangling processes we considered here operate on a timescale much longer than $1/\omega_m$, thus justifying the use of the linearized Hamiltonian to describe transient behaviors.

7.3. Sørensen-Mølmer Mechanism

To gain insights into the dynamics of the coherent optomechanical interactions and to discuss the S-M mechanism for the three-mode optomechanical system, we first ignore the damping of both optical and mechanical systems and adjust the optomechanical coupling rates for the two optical modes such that $g_1 = g_2 = g$. In this limit, the interaction Hamiltonian for the entanglement generation falls into a class discussed originally by Mølmer and Sørensen and also by Milburn [56, 58, 74]. For this class, the exact propagator can be written in a form (see Appendix E)

$$U(t) = e^{-iA(x,p,t)} e^{-iF(x,p,t)x_b} e^{-iG(x,p,t)p_b}, \tag{7.2}$$

where $x = x_1 + x_2$ and $p = p_2 - p_1$ are EPR-like variables, with the dimensionless quadrature variables defined as $x_i = (a_i + a_i^\dagger)/\sqrt{2}$, $p_i = i(a_i^\dagger - a_i)/\sqrt{2}$, and similarly for the mechanical mode operators x_b and p_b. At regularly spaced time intervals $t_n = 2\pi n/\Delta$,

$$F(x, p, t_n) = G(x, p, t_n) = 0, \tag{7.3}$$

returning the mechanical degrees of freedom to their initial states. At the same time, $A(x, p, t_n)$, which is given by,

$$A(x, p, t_n) = -\frac{g^2}{2\Delta}(x^2 + p^2)t_n \tag{7.4}$$

generates entanglement between modes 1 and 2, according to

$$U^\dagger(x, p, t_n)a_{1(2)}U(x, p, t_n) = \mu a_{1(2)} + \nu a^\dagger_{2(1)}, \tag{7.5}$$

where $\mu = 1 + ir$ and $\nu = ir$, with a squeezing parameter $r = g^2 t_n/2\Delta$ (see the supplementary materials for the derivation of the propagator and for the analytical expression of the entanglement). A sideband detuning that is less than g leads to a large squeezing parameter at $t_1 = 2\pi/\Delta$. To maintain thermal robustness in the presence of damping, the detuning also needs to far exceed γ and specifically, $\Delta \gg \gamma n_{th}$.

It is remarkable that independent of the particular form of the initial state of the system, the mechanical oscillator periodically returns to its initial state, and leaves the optical modes increasingly entangled upon each return. The entanglement is generated through the mechanical motion of the system. However, the final entangled optical state contains no information of the mechanical system, and can thus be robust against thermal Brownian noise that enters the system through the mechanical oscillator. Note that in the limit that Δ far exceeds $\kappa_{1,2}$ and γ, the mechanical degrees of freedom can be adiabatically eliminated [75]. The optical entanglement generation can thus become thermally robust without satisfying the condition, $t_n = 2\pi n/\Delta$. The large detuning, however, limits the amplitude of the squeezing parameter and hence the degree of entanglement that can be achieved.

7.4. Analysis with Langevin Equations

We have used the quantum Langevin equations to analyze in detail the dynamics of the entanglement generation and especially the effects of thermal mechanical noise. We work in a rotating frame $\tilde{H} = U_R H U_R^\dagger$, where H is the Hamiltonian of Eq. (7.1), and $U_R = e^{i(\omega_m+\Delta)(a_1^\dagger a_1 - a_2^\dagger a_2 + b^\dagger b)t}$. In this frame, the quantum Langevin equations in the resolved sideband limit have the form

$$\dot{a}_1 = -\frac{\kappa_1}{2} a_1 - i g_1 b - \sqrt{\kappa_1} a_{in,1} \tag{7.6}$$

$$\dot{a}_2^\dagger = -\frac{\kappa_2}{2} a_2^\dagger + i g_2 b - \sqrt{\kappa_2} a_{in,2}^\dagger \tag{7.7}$$

$$\dot{b} = -(i\Delta + \frac{\gamma}{2}) b - i g_1 a_1 - i g_2 a_2^\dagger - \sqrt{\gamma} b_{in}, \tag{7.8}$$

where the resolved sideband limit along with the rotating wave approximation has allowed us to drop all counter-rotating terms. The input operators for the optical modes, $a_{in,i}(t)$, characterize the optical cavity coupling to the vacuum, and have correlation functions $\langle a_{in,i}(t) a_{in,i}^\dagger(t') \rangle = \delta(t - t')$. The Brownian noise that enters the system through the mechanical degree of freedom is described by the operator $b_{in}(t)$. We assume the system to have a sufficiently large mechanical quality factor $Q_m = \omega_m/\gamma$ such that the Brownian noise can be approximated to be Markovian [76], with $\langle b_{in}(t) b_{in}^\dagger(t') \rangle = (n_{th} + 1)\delta(t - t')$.

The entanglement is generated for optical driving pulses with a given duration and is quantified with the logarithmic negativity, $E_\mathcal{N}$ [77, 78] (Appendix F). We limit the duration of the optical pulse to ensure that nonlinear optomechanical interactions are negligible. For typical optomechanical systems, the mechanical damping rate can be much smaller than both the cavity linewidth and the effective optomechanical coupling rate. In the following, we first consider the intracavity entanglement in the

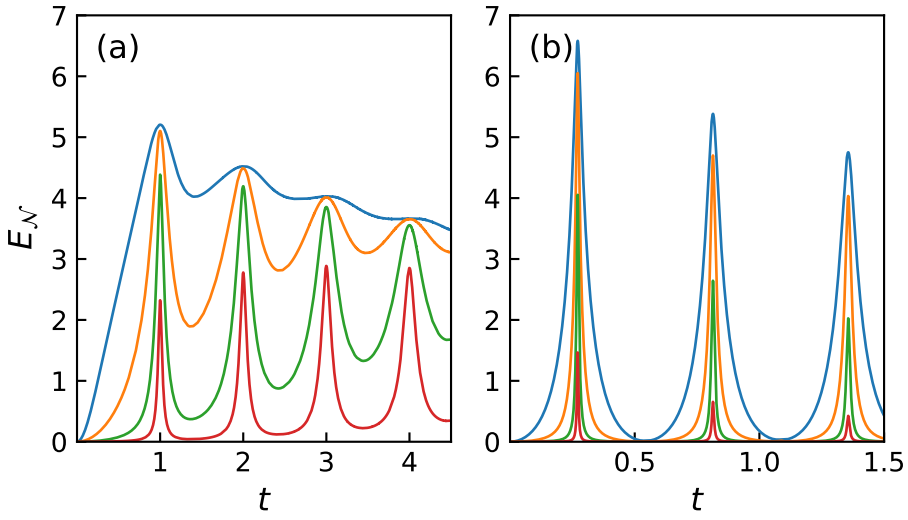

FIGURE 7.2. Intracavity entanglement versus time. (a) Sørensen-Mølmer scheme with $g/\gamma = 4 \cdot 10^3$ and $\Delta/\gamma = 10^3$. (b) Bogoliubov mode scheme with $g_1/\gamma = 4 \cdot 10^3$ and $g_2/\gamma = 3.5 \cdot 10^3$. For both (a) and (b), $\kappa_1/\gamma = \kappa_2/\gamma = 10$ and the time is in units of $2\pi/(10^3\gamma)$. From top to bottom, $n_{th} = 10, 10^2, 10^3, 10^4$.

strong coupling regime, where $g \gg \kappa_i$. We then analyze the entanglement contained in an output mode for a system in the weak coupling regime with $g \ll \kappa_i$.

7.5. Strong Coupling

Figure 7.2a plots the intracavity entanglement generated deep in the strong coupling regime. As shown in Fig. 7.2a, the negativity oscillates as a function of time, with the peaks or the maxima of the negativity located at times t_n, when the mechanical degree of freedom is returned to its initial state, as anticipated from the above theoretical treatment without the inclusion of the damping processes. With increasing thermal phonon occupation, the maxima decrease gradually, but the oscillation becomes much more pronounced, with the minima in the negativity quickly approaching zero, illustrating the importance and also the effectiveness of the S-M mechanism in circumventing the thermal mechanical noise.

For comparison, Fig. 7.2b plots the intracavity entanglement as a function of time, generated in the same system and under otherwise similar conditions by the method of the Bogoliubov mode [37]. In this case, the entanglement maxima occur when the mechanical oscillator returns to its initial state through the Rabi oscillation of the bright Bogoliubov modes that couple to the mechanical oscillator. The period of the oscillation in the negativity in Fig. 7.2b is thus determined by the effective optomechanical coupling rate of the bright modes. At low thermal phonon occupation, the Bogoliubov mode approach can generate stronger maximum entanglement. However, the entanglement is more sensitive to the timing of the optical field than that generated with the S-M mechanism (see Fig. 7.2). A small deviation from an exact optomechanical π pulse leads to appreciable mixing between the optical and mechanical excitations. For the S-M mechanism, a destructive interference occurring under the condition of $\delta_1 = -\delta_2$ and $g_1 = g_2$ reduces the mixing between the mechanical oscillator and the optical modes, even at times away from t_n [56].

For a more detailed comparison of the thermal robustness of the two entanglement schemes, we plot in Fig. 7.3 the maximum negativity obtained under the conditions of Fig. 7.2 for each entanglement scheme as a function of the initial thermal phonon occupation. As shown in Fig. 7.3, the Sørensen-Mølmer scheme becomes advantageous when n_{th} exceeds 500, which further highlights the robustness of the Sørensen-Mølmer scheme against thermal mechanical noise.

7.6. Weak Coupling

In the weak coupling regime, we solve the optical modes adiabatically and investigate the entanglement in the output of the cavity as a function of pulse

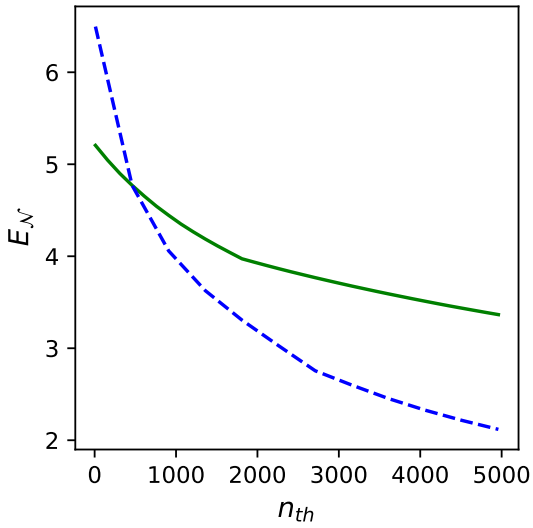

FIGURE 7.3. Maximum intracavity entanglement as a function of thermal phonon occupation n_{th}. The solid (dashed) line is for the Sørensen-Mølmer (Bogoliubov mode) scheme. The parameters used are the same as those in Fig. 7.2.

duration. The entanglement in the cavity output is more relevant to experimental implementation and to potential applications than the intracavity entanglement. Starting with Eq. (7.6), the adiabatic solutions for the optical modes are

$$a_1(t) = -\frac{2ig_1}{\kappa_1} b(t) - \frac{2}{\sqrt{\kappa_1}} a_{in,1}(t) \tag{7.9}$$

$$a_2^\dagger(t) = \frac{2ig_2}{\kappa_2} b(t) - \frac{2}{\sqrt{\kappa_2}} a_{in,2}^\dagger(t), \tag{7.10}$$

where $b(t)$ is the formal solution of the mechanical mode. Using the input-output relation $a_{out} = a_{in} + \sqrt{\kappa} a$, the cavity output is related to the input by

$$a_{out,1}(t) = -2i\sqrt{G_1} b(t) - a_{in,1}(t) \tag{7.11}$$

$$a_{out,2}^\dagger(t) = 2i\sqrt{G_2} b(t) - a_{in,2}^\dagger(t), \tag{7.12}$$

where

$$b(t) = b(0)e^{-zt} + e^{-zt}\int_0^t e^{zs}\left(2i\sqrt{G_1}a_{in,1}(s) + 2i\sqrt{G_2}a^\dagger_{in,2}(s) - \sqrt{\gamma}b_{in}(s)\right)\mathrm{d}s. \quad (7.13)$$

The complex number $z = \Gamma + i\Delta$ contains an effective damping rate $\Gamma = 2G_1 - 2G_2 + \gamma/2$, where the coupling rates $G_i = g_i^2/\kappa_i$ effectively characterize the optomechanical interaction strength in the bad cavity limit. This also leads to a modified requirement for the S-M mechanism, $G_1 = G_2$.

The output modes $a_{out,i}(t)$ are improper continuous operators, not well suited for characterizing entanglement. One may instead describe the system in a discrete mode basis by defining independent discrete bosonic operators [79]

$$A^{(k)}_{out,i} = \int \mathrm{d}t\ \phi^*_k(t)a_{out,i}(t) \quad (7.14)$$

where $i = 1, 2$ again label the two optical modes of the system, the index k labels members of a denumerably infinite set, and the mode functions $\phi_k(t)$ form a complete orthonormal basis under the inner product $\int \mathrm{d}t\ \phi^*_k(t)\phi_{k'}(t)$. The operators defined by equation (7.14) satisfy the proper commutation relations, $[A^{(j)}_{out,i}, A^{(k)\dagger}_{out,i}] = \delta_{jk}$, for characterizing the entanglement of the output modes with logarithmic negativity.

We study the entanglement between discrete modes characterized by the mode functions

$$\phi_k(t) = \frac{\theta(t) - \theta(t-\tau)}{\sqrt{\tau}}e^{i2\pi kt/\tau}, \quad (7.15)$$

where k is any integer, τ is the pulse duration, and $\theta(t)$ is the Heaviside function. Thus for every value of τ, we pick a complete set of modes for the time interval

between $t = 0$ and $t = \tau$, giving a full description of what happened in that time interval.

In terms of this choice of discrete modes, each output mode is the sum of input modes labeled by the same index k, and one additional mode,

$$A'^{(\dagger)}_{\mathrm{in},1(2)} = \sqrt{\frac{2\Gamma}{e^{2\Gamma\tau}-1}} \int_0^\tau dt\, e^{zt} a^{(\dagger)}_{\mathrm{in},1(2)}, \tag{7.16}$$

which is a superposition of all the k modes for any fixed value of τ. The exact input-output relations for mode k are then

$$\begin{aligned} A^{(k)}_{\mathrm{out},1} = \frac{2i\sqrt{G_1}}{\chi_k\sqrt{\tau}} \Bigg\{ & -(e^{\chi_k\tau}-1)\, b(0) + \sqrt{\tau}\left(2i\sqrt{G_1}A^{(k)}_{\mathrm{in},1} + 2i\sqrt{G_2}A^{(k)\dagger}_{\mathrm{in},2} - \sqrt{\gamma}B^{(k)}_{\mathrm{in}}\right) \\ & - e^{\chi_k\tau}\sqrt{\frac{e^{2\Gamma\tau}-1}{2\Gamma}}\left(2i\sqrt{G_1}A'_{\mathrm{in},1} + 2i\sqrt{G_2}A'^{\dagger}_{\mathrm{in},2} - \sqrt{\gamma}B'_{\mathrm{in}}\right) + \frac{i\chi_k\sqrt{\tau}}{2\sqrt{G_1}}A^{(k)}_{\mathrm{in},1}\Bigg\}, \end{aligned} \tag{7.17}$$

$$\begin{aligned} A^{(k)\dagger}_{\mathrm{out},2} = \frac{2i\sqrt{G_2}}{\chi_k\sqrt{\tau}} \Bigg\{ & +(e^{\chi_k\tau}-1)\, b(0) - \sqrt{\tau}\left(2i\sqrt{G_1}A^{(k)}_{\mathrm{in},1} + 2i\sqrt{G_2}A^{(k)\dagger}_{\mathrm{in},2} - \sqrt{\gamma}B^{(k)}_{\mathrm{in}}\right) \\ & + e^{\chi_k\tau}\sqrt{\frac{e^{2\Gamma\tau}-1}{2\Gamma}}\left(2i\sqrt{G_1}A'_{\mathrm{in},1} + 2i\sqrt{G_2}A'^{\dagger}_{\mathrm{in},2} - \sqrt{\gamma}B'_{\mathrm{in}}\right) + \frac{i\chi_k\sqrt{\tau}}{2\sqrt{G_2}}A^{(k)}_{\mathrm{in},1}\Bigg\}, \end{aligned} \tag{7.18}$$

where we have defined $B^{(k)}_{\mathrm{in}}$ and B'_{in} in the same manner as $A^{(k)}_{\mathrm{in},1}$ and A'_{in}, and $\chi_k = -\Gamma + i(2\pi k/\tau - \Delta)$. A mode labeled by k has central frequency $\omega_k = 2\pi k/\tau$.

The SM mechanism remains effective in the regime of weak optomechanical coupling. Figure 7.4a plots the entanglement contained in the modes defined by Eq. (7.15) with $k = 0$, as a function of the pulse duration τ, and for various thermal phonon occupations. Similar to the results obtained in the strong coupling regime shown in Fig. 7.2a, we find that the negativity oscillates with the pulse duration,

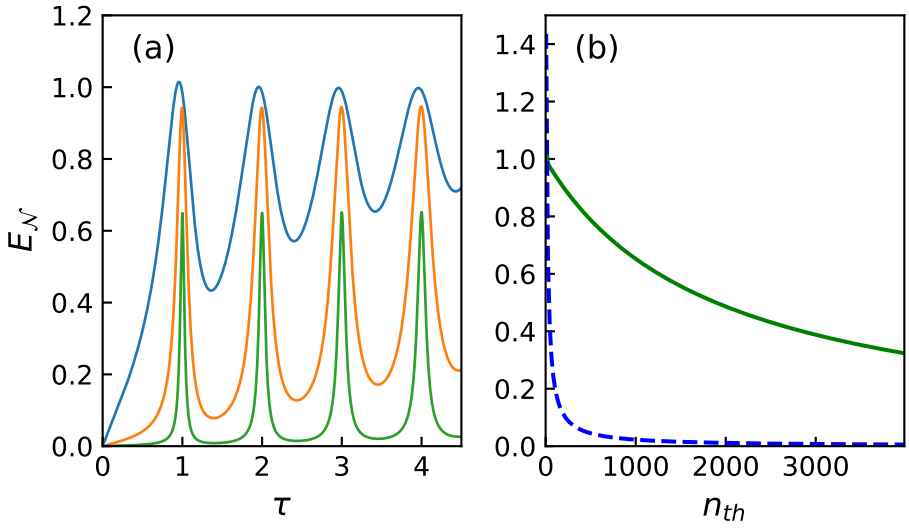

FIGURE 7.4. Entanglement of an output mode in the bad cavity limit, with $\Delta/\gamma = 10^3$ and $\kappa_1/\gamma = \kappa_2/\gamma = 6 \cdot 10^3$. (a) As a function of pulse duration τ, in units of $2\pi/(10^3\gamma)$, with $G_1/\gamma = G_2/\gamma = 667$. From top to bottom, $n_{th} = 10, 10^2, 10^3$. (b) Maximum entanglement generated as a function of thermal phonon occupation. Solid line: $G_1 = G_2$. Dashed line: $G_1/\gamma = 667$ and $G_2/\gamma = 540$.

.

with the entanglement maxima occurring at pulse durations satisfying the condition of $t_n = 2\pi n/\Delta$. With increasing thermal phonon occupation, the maxima decrease gradually, while the minima quickly approach zero. Significant entanglement can be still achieved with a thermal phonon occupation of order 1000.

The SM mechanism for the three-mode optomechanical system requires equal effective optomechanical coupling for the two optical modes. To illustrate this, we plot in Fig. 7.4b the negativity as a function of the thermal phonon occupation when the requirement of $G_1 = G_2$ is satisfied (solid), and when the requirement is not (dashed). Thermally robust entanglement can be achieved only when $G_1 = G_2$ is satisfied. Note that results similar to the dashed line in Fig. 7.4b have also been obtained with $\Delta = 0$ and in the weak coupling regime. In this case, thermally robust entanglement cannot be achieved regardless whether $G_1 = G_2$ is satisfied.

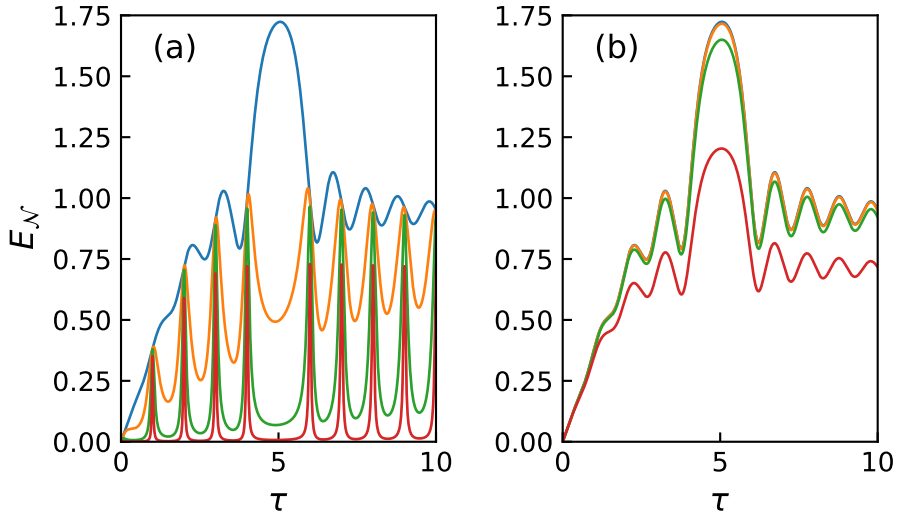

FIGURE 7.5. Entanglement of $k = 5$ output modes, with $\Delta/\gamma = 2\pi \times 10^3$, $G_1/\gamma = G_2/\gamma = 10^3$. τ has units $2\pi/\Delta$. From top to bottom, $n_{th} = 0, 10, 10^2, 10^3$. (a) Without pre-cooling, initial phonon occupation (n_0) equal to n_{th}. (b) With initial phonon occupation pre-cooled to the ground state.

For the $k \neq 0$ modes, we expect to see a resonance in the entanglement when the central frequency of the mode k matches the central frequency of the sideband generated from the detuned pump field. Thus, a resonance should occur under the condition $2\pi k/\tau = \Delta$. Figure 7.5 demonstrates such a resonance for the $k = 5$ modes. We find the resonance to degrade quickly with the increasing initial phonon occupation number, as shown in Fig. 7.5a. Experimentally, the initial phonon occupation can be suppressed by first driving only the red sideband pump. Figure 7.5b demonstrates the advantage of such pre-cooling to retain a strong entanglement resonance even at larger bath temperatures.

7.7. Conclusions

In summary, we have presented a pulsed approach, in which the optical driving fields are slightly detuned from the respective sideband resonance, for generating

optical entanglement in a three-mode optomechanical system. In this approach, the mechanical oscillator returns to its initial state and is disentangled with the optical modes upon the completion of the entanglement operation. Although schemes based on the use of the Bogoliubov modes can lead to greater entanglement when the mechanical oscillator is near the motional ground state, the Sørensen-Mølmer scheme is more robust against thermal mechanical noise. In particular, significant entanglement can still persist at relatively high thermal phonon occupation in the weak coupling regime, providing a promising avenue for generating optical entanglement, including that between optical and microwave modes in currently accessible experimental systems.

CHAPTER VIII

PHONONIC QUANTUM NETWORKS

This chapter is based on work coauthored by Hailin Wang. The manuscript is currently in the review process. A preprint is available through arXiv.org [25].

8.1. Introduction

Photons are excellent carriers of quantum information and are the ideal choice for long distance quantum communications and networks [80, 81, 82, 83, 84]. For on-chip communications and networks, there are, however, a few inherent limitations. For example, the speed of light can be too fast for communications over short distances, such as a few hundred micrometers or less. Scattering losses of electromagnetic waves into vacuum can be excessive even with state-of-the-are nanofabrication technologies, which severely limits the photon lifetime in nano-optical systems such as photonic crystal optical resonators.

In comparison, phonons, which are the quanta of mechanical waves, feature several distinct advantages for on-chip communications [85, 86, 87]. The speed of sound is about five orders of magnitude slower than the speed of light. Mechanical waves cannot propagate in vacuum and thus are not subject to scattering or radiation losses into vacuum. The relatively long acoustic wavelength also makes it easier to fabricate phononic nanostructures for confining and guiding acoustic waves on a chip.

The primary function of a quantum network is to enable high-fidelity quantum state transfer between two neighboring quantum nodes. This can take place in a cascaded network [88], for which the coupling between neighboring quantum nodes is unidirectional [89]. Quantum state transfer protocols that are robust against

thermal noise in the communication channel have been proposed recently for cascaded networks [90, 91]. Cascaded optical quantum networks can be realized with chiral optical interactions [92, 93], as demonstrated with atoms and quantum dots [94, 95]. The lack of easily accessible chiral acoustic processes, however, makes it difficult to implement cascaded phononic quantum networks [85, 96].

Furthermore, there are two inherent obstacles in scaling up a phononic network. First of all, the spin-mechanical coupling rate at the single-phonon level scales with the zero-point fluctuation of the mechanical system, which is proportional to $1/m$ with m being the mass of the mechanical system. The larger the network is, the smaller the single-phonon coupling rate usually becomes. Secondly, nearest neighbor coupling of a large number of mechanical resonators can lead to the formation of spectrally-dense mechanical modes, causing crosstalk between the collective mechanical modes. These problems are well known in ion trap quantum computers [97], for which phonon-mediated interactions play an essential role. A solution to these problems is to build phononic networks using *closed mechanical subsystems*. An apparent difficulty is to enable quantum state transfer between the seemingly closed subsystems.

In this chapter, we propose a general and conceptually-simple architecture for quantum networks that feature closed subsystems. This architecture employs at least two frequencies for communications and exploits alternating, frequency-selective waveguides. As illustrated schematically in Fig. 8.1a, each quantum node couples to two waveguides, A and B, which allow signal propagation at frequencies near ω_A and ω_B, but forbid signal propagation at frequencies near ω_B and ω_A, respectively. This special frequency selectivity of the alternating waveguides can make any two neighboring nodes and the waveguide between them a closed subsystem, as highlighted in Fig. 8.1a. For a phononic quantum network of solid state spins, this architecture

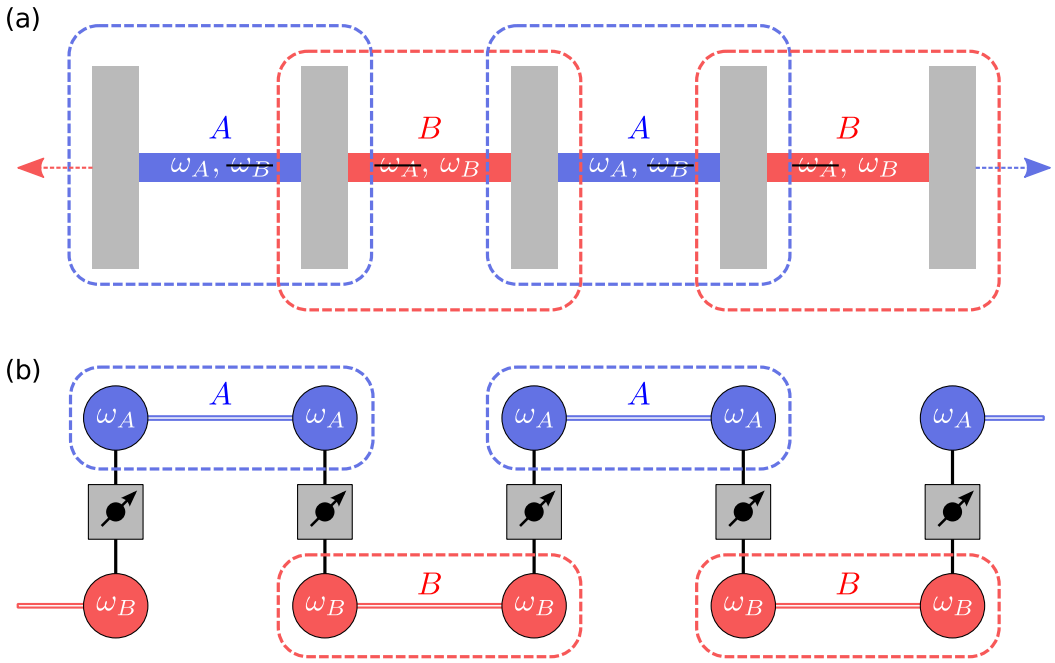

FIGURE 8.1. Concept of the network. (a) Schematic of a quantum network with alternating and frequency-selective waveguides, in which each quantum node couples to two different waveguides, A and B. Propagation near frequencies ω_A and ω_B are allowed, but frequencies near ω_B and ω_A are forbidden, for waveguides A and B respectively. As indicated by the dashed-line boxes, any two neighboring quantum nodes and the waveguide between them can form a closed subsystem. (b) An implementation using solid state spins and mechanical resonators. In each quantum node, a spin system couples selectively to two resonator modes with frequency ω_A and ω_B. The network consists of closed mechanical subsystems coupled together via the spins.

can be implemented with quantum nodes, in which a spin system couples selectively to two mechanical resonator modes with frequency ω_B and ω_A. This phononic quantum network can be viewed as closed mechanical subsystems coupled together via the spins, as shown in Fig. 8.1b. In this network, high-fidelity quantum state transfer between the neighboring spin systems can take place via the closed mechanical subsystems.

We describe an implementation of this architecture employing diamond color centers, nanomechanical resonators, and phononic crystal waveguides. In this

implementation, color centers featuring robust spin qubits couple to vibrations of nanomechanical resonators through sideband (i.e. phonon-assisted) transitions driven by external optical or microwave fields [98]. Communications between these spin-mechanical resonators take place via alternating phononic crystal waveguides [99]. A key feature of the network is specially-designed band gaps in the phononic crystal waveguides, which enable frequency-selective coupling. In addition, the entire network can be embedded in a phononic crystal lattice, which isolates and protects the network from the surrounding mechanical environment. Note that diamond photonic crystals and optomechanical crystals, which are technically more demanding than diamond phononic crystals in terms of nanofabrication, have already been successfully realized [100, 101, 102].

We also outline two schemes for quantum state transfer between spin systems in neighboring resonators. One scheme relies on strong spin-mechanical coupling of a single spin. The other employs spin ensembles for the quantum state transfer and approximates the spin ensemble as a bosonic oscillator [90, 91]. Both schemes can be robust against thermal phonons in the phononic waveguide.

Solid state spin systems such as negatively-charged nitrogen vacancy (NV) centers in diamond have emerged as a promising qubit system for quantum information processing [103, 104, 105]. High fidelity quantum control of individual spin qubits via microwave or optical transitions has been well established [106, 107, 108, 109, 110, 111, 112]. Photonic networks of NV centers have also been proposed [113, 114, 115]. The phononic quantum network described in this paper can potentially enable a scalable, chip-based experimental platform for developing quantum computers using robust solid-state spin qubits.

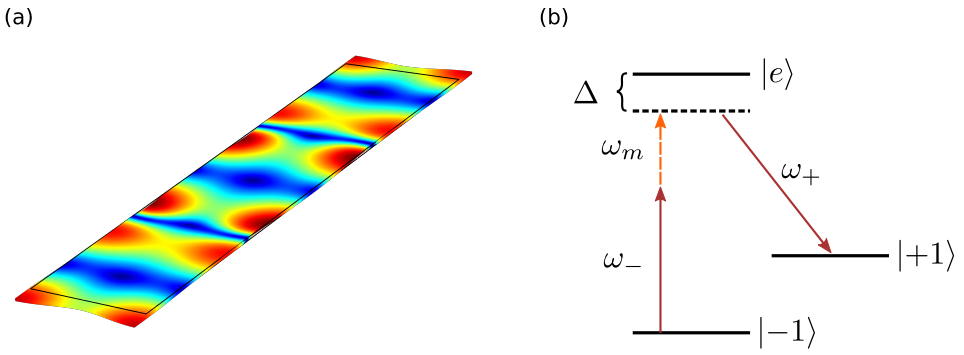

FIGURE 8.2. Concet of spin qubit coupling to phonons. (a) Displacement pattern of a fifth order compression mode in a thin rectangular diamond plate with dimension (27, 8, 0.3) μm. (b) Schematic of a spin qubit coupling to a mechanical mode with frequency ω_m through a resonant Raman process, driven by two external optical fields with frequency ω_+ and ω_-. We can couple the spin qubit to a given mechanical mode by choosing a suitable detuning between ω_+ and ω_-.

8.2. Phononic Quantum Networks

The proposed phononic network consists of diamond-based spin-mechanical resonators that couple spin qubits in diamond to relevant mechanical modes, phononic crystal waveguides with suitable energy gaps and waveguide modes, and a two-dimensional (2D) phononic crystal lattice that protects the mechanical modes involved in the phononic network. For numerical calculations, we assume that the phononic network is fabricated from a diamond membrane with a thickness of 300 nm. In addition to NV centers, other color centers in diamond, such as silicon vacancy (SiV) or germanium vacancy (GeV) centers [116, 117, 118, 119], can also be used in the phononic network. High quality NV, SiV, and GeV centers can be created in diamond through ion implantation, followed by elaborate thermal annealing and surface treatment [120, 121].

8.2.1. Spin-Mechanical resonators

The elementary unit or node in our quantum network is a spin-mechanical resonator, in which spin qubits couple to mechanical resonator modes in a thin, rectangular diamond plate. Calculations of mechanical normal modes in the diamond plate are discussed in detail in Appendix G. We are interested in mechanical compression modes that are symmetric with respect to the median plane of the plate (the so-called symmetric modes). Figure 8.2a shows, as an example, the displacement pattern of a fifth order compression mode.

Coherent interactions between electron spin states of a NV center and long-wavelength mechanical vibrations of the diamond lattice have been experimentally explored via either ground-state or excited-state strain coupling [35, 98, 122, 123, 124, 125, 126, 127, 128, 129, 130, 131]. The orbital degrees of freedom of a NV center can couple strongly to the long-wavelength mechanical vibrations via the excited states. As a result, the excited-state strain coupling for a NV center is about five orders of magnitude stronger than the ground-state strain coupling [131, 132, 133]. For defect centers such as SiV and GeV centers, strong coupling between the orbital degrees of freedom and the mechanical vibrations can also take place through the ground states [134].

As illustrated in Fig. 8.2b, we control the coupling between the ground spin states of the NV center and the relevant mechanical mode through a resonant Raman process that consists of a sideband (or phonon-assisted) optical transition as well as a direct dipole optical transition. The Raman process is driven and controlled by two external optical fields. The interaction Hamiltonian (Appendix H) is given by [130]

$$V = \hbar\frac{\Omega_-}{2}\frac{g_s}{\omega_m}\left(\hat{a}e^{i(\Delta_- - \omega_m)t}\left|e\right\rangle\left\langle -\right| + \text{H.c.}\right) + \hbar\frac{\Omega_+}{2}\left(e^{i\Delta_+ t}\left|e\right\rangle\left\langle +\right| + \text{H.c.}\right), \tag{8.1}$$

where $g_s = Dk_m x_{\mathrm{zpf}}$, D is the deformation potential, x_{zpf} is the zero-point fluctuation, k_m is the phonon wavevector, Ω_+ and Ω_- are the optical Rabi frequencies and Δ_+ and Δ_- are the effective dipole detunings for the two respective optical transitions, and $\hat{a}$ is the annihilation operator for a mechanical mode with frequency ω_m. For a NV center, the $m_s = \pm 1$ ground spin states can serve as states $|\pm\rangle$ and the A_2 state can serve as state $|e\rangle$ [135].

The use of the sideband transitions, instead of resonant transitions, enables the selective coupling of an electron spin to any relevant mechanical mode, which is an essential requirement for the implementation of the proposed network architecture. Specifically, we can couple the electron spin states to a mechanical mode with frequency ω_m by setting the detuning between the two optical driving fields according to the Raman resonant condition, $\Delta_- - \omega_m = \Delta_+$. To avoid the population of the excited state, we can also exploit a combination of techniques, such as dark states, shortcuts to adiabatic passage [136, 137], Magnus expansions [138], as well as large dipole detuning. Excited-state mediated spin-mechanical coupling via a dark state has already been demonstrated in an earlier experimental study [130].

Note that for negatively charged SiV or GeV centers that feature strong ground-state strain coupling, the spin-mechanical coupling can also be driven by microwave sideband transitions between the ground spin states. In addition, the coupling schemes discussed in [96] can also be adopted.

8.2.2. Phononic crystal waveguides and alternating, frequency-selective coupling

We use phononic crystal waveguides, which are one-dimensional (1D) phononic crystals consisting of a periodic array of holes in a beam (see Fig. 8.3a), to network

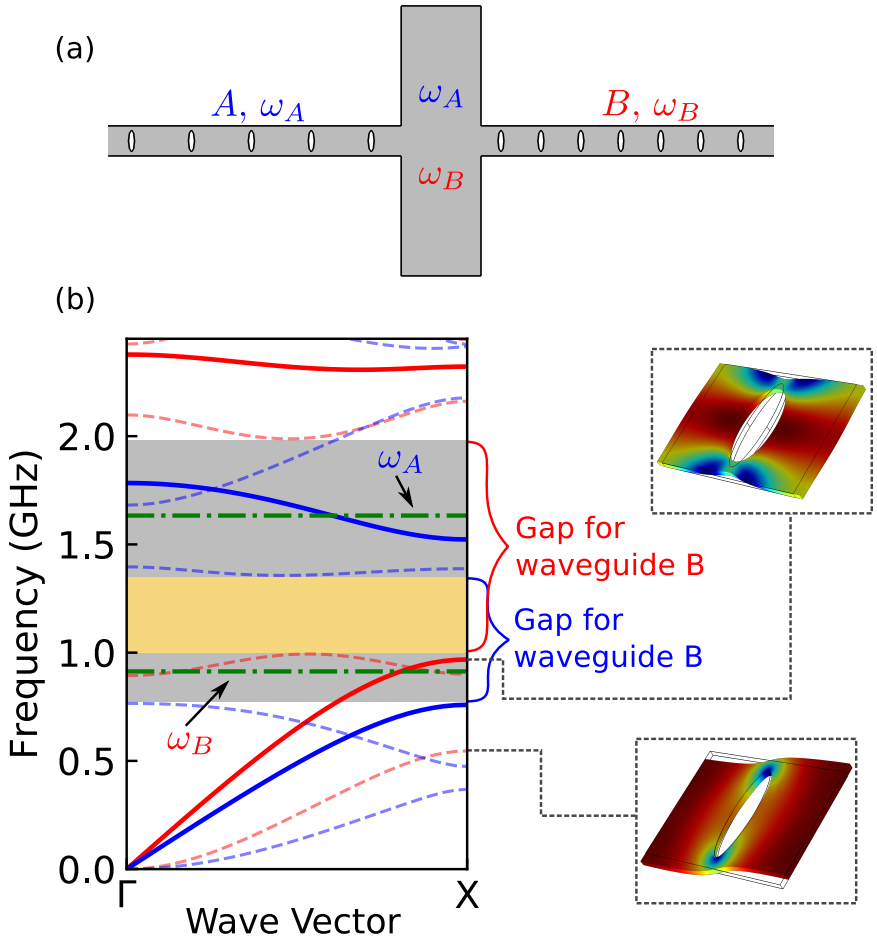

FIGURE 8.3. Waveguide design and band structure. (a) A mechanical resonator couples to two phononic crystal waveguides with a width of 3 μm (waveguide A) and 4 μm (waveguide B). For the elliptical holes in the waveguides, the minor (major) axes are 0.6 (2.2) μm. (b) Phononic band structures of the two waveguides. Each features a band gap. Blue lines: Waveguide A. Red lines: Waveguide B. The grey shaded areas show non-overlapping regions of the two band gaps. The yellow shaded area shows the overlapping region. Solid (dashed) lines are for modes with displacement patterns that are symmetric (antisymmetric) about the plane that bisects and is normal to both the waveguide and the resonators. Dot-dashed lines indicate the frequencies of the two resonator modes, ω_A and ω_B, used to couple to the respective waveguide modes.

together a series of spin-mechanical resonators. In a simple picture, mechanical vibrations in a resonator excite propagating mechanical waves in the adjacent phononic waveguides [99]. Conversely, mechanical waves in the phononic waveguide also excite vibrations in the adjacent mechanical resonators.

A suitable design of the phononic crystal waveguides can enable alternating, frequency-selective coupling for the phononic network. As shown in Fig. 8.3a, a spin-mechanical resonator couples to two phononic waveguides, A and B, that feature an array of elliptical holes with different periods. The phononic band structure of each waveguide shows a sizable band gap for the symmetric mechanical modes (see Fig. 8.3b). The center of the band gap for waveguide B, which features a shorter period, is higher in frequency than that for waveguide A, which features a longer period. For this design, the two band gaps feature two non-overlapping spectral regions, as highlighted by the grey shaded areas in Fig. 8.3b. We use waveguide modes and resonator modes in these non-overlapping regions for quantum state transfer between spin systems in neighboring quantum nodes.

Specifically, for the resonator-waveguide design shown in Fig. 8.3a, a higher frequency resonator mode with $\omega_A/2\pi = 1.6332$ GHz, which is a fifth order compression mode of the resonator and is in the band gap of waveguide B (see Fig. 8.3b), couples resonantly to a mode in waveguide A. A lower frequency resonator mode with $\omega_B/2\pi = 0.9133$ GHz, which is a third order compression mode and is in the band gap of waveguide A (see Fig. 8.3b), couples resonantly to a mode in waveguide B. This design effectively realizes the network architecture shown in Fig. 8.1b.

Because of the alternating, frequency-selective coupling, any two neighboring resonators and the waveguide between them can form a closed subsystem. The

relevant waveguide modes are thus discrete standing wave modes. For a relatively short waveguide, the frequency spacing of these modes can be large compared with other relevant frequency scales and the waveguide can thus behave like a single-mode mechanical oscillator. In this limit, we can treat the closed mechanical subsystem as a three-mode system. Appendix G discusses in detail numerical calculations of the normal modes of the three-mode subsystem and, in particular, the coupling rate, g, between the resonator and the waveguide modes. Depending on the specific design of the waveguide and resonators, $g/2\pi$ can range from a few kHz to more than 10 MHz. Note that we can engineer the coupling rate by tailoring or shaping the contact area between the weaveguide and the resonator.

8.2.3. Isolating intra-node spin-mechanical coupling from the waveguides

We separate the spin qubits in a spin-mechanical resonator into logic qubits and communication qubits, which are used exclusively for quantum state transfer between neighboring quantum nodes. Ideally, intra-node interactions should be decoupled from the phononic waveguides, since residual coupling of the logic qubits to the adjacent waveguides leads to additional decoherence.

The band gaps of the phononic crystal waveguides can be exploited to isolate the intra-node spin-mechanical coupling from the waveguides. Specifically, the logic qubits can couple to each other and to the communication qubits through a resonator mode with a frequency that is in the band gap of both phononic crystal waveguides, i.e. in the overlapping spectral region of the two phononic band gaps, as highlighted by the yellow shaded area in Fig. 8.3b. In this case, the phonon-mediated coupling among the logic qubits and the communication qubits within a spin-mechanical resonator or a quantum node is decoupled from the adjacent waveguides. For the resonator-

waveguide design shown in Fig. 8.3a, the fourth order compressional mode of the resonator, with $\omega_R/2\pi = 1.3258$ GHz, falls in the band gap of both phononic crystal waveguides and can thus serve as a mechanical mode for intra-node spin-mechanical coupling. Other resonator modes in the overlapping region of the two band gaps can also be used for this purpose, providing flexibility in the physical location of the logic qubits.

8.2.4. Protecting phononic networks with a 2D phononic crystal lattice

To protect the relevant mechanical modes from the surrounding mechanical environment, we embed the entire phononic network in a 2D phononic crystal lattice, as illustrated in Fig. 8.4. 2D phononic crystal lattices have been used extensively in earlier studies to isolate mechanical systems such as optomechanical crystals, membranes, and single-mode phononic wires from the surrounding environment [139, 140, 141]. The use of 2D phononic crystal shields has led to the experimental realization of ultrahigh mechanical Q-factors, with $\omega Q_m/2\pi$ approaching or even exceeding 10^17 [2, 142].

Figure 8.4b plots the phononic band structure of the symmetric mechanical modes in the 2D phononic crystal lattice shown in Fig. 8.4a. The band structure of the 2D lattice features a band gap between 0.85 and 2.25 GHz, spanning the phononic band gaps of both phononic crystal waveguides A and B and thus protecting all the mechanical modes relevant to the phononic quantum network. For the design shown in Fig. 8.4a, only waveguide B is attached to the 2D lattice, because this waveguide and the 2D square lattice have the same period. In this case, mechanical modes with frequencies near ω_A are isolated from the environment by the band gap in the 2D

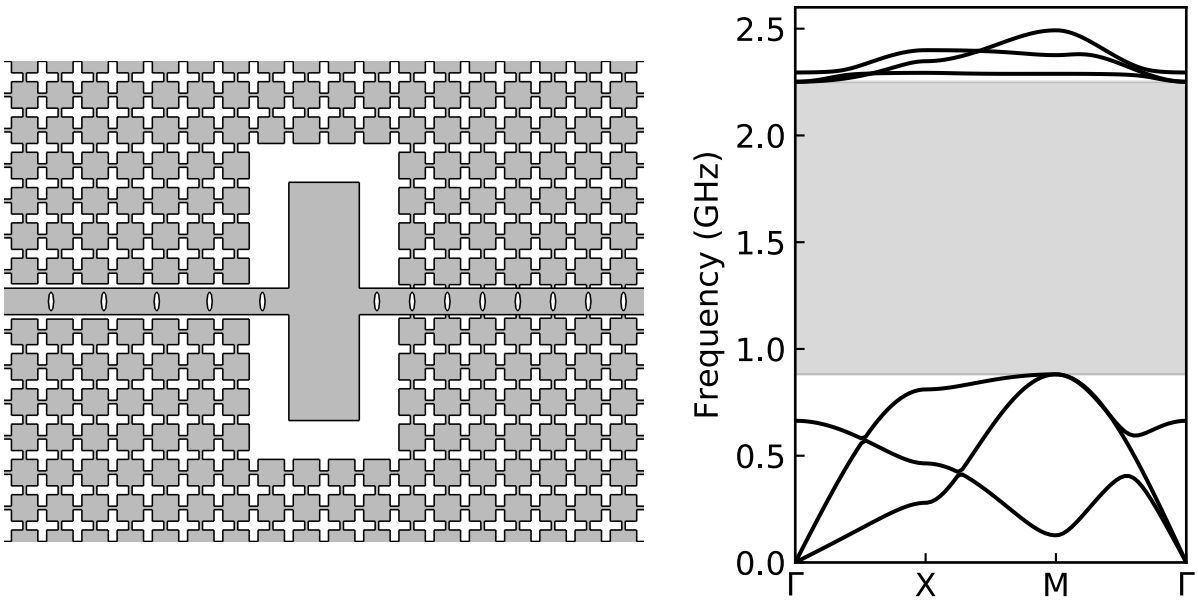

FIGURE 8.4. Phononic shield design and band structure. Left: A phononic network embedded in a square photonic crystal lattice with a period of 4 μm. The side length of the squares is 3 μm. The connecting bridges have a length of 1 μm and width of 0.4 μm. Right: Phononic band structure of the 2D lattice. Only symmetric modes are shown.

lattice as well as the band gap in waveguide B, which also relaxes the requirement that the band gap of the 2D lattice spans both ω_A and ω_B.

The specific design for the mechanical resonators, phononic crystal waveguides, and 2D phononic crystal shields discussed in this section is by no means optimal. The design serves as an example for implementing the proposed network architecture in a phononic network.

8.3. Quantum State Transfers

Mechanically-mediated quantum state transfers have been investigated theoretically for optomechanical transducers that can interface hybrid quantum systems [29, 51, 143, 144, 145, 146]. State transfer processes that can be robust against thermal mechanical noise have also been proposed. One approach is based on the use of dark

modes, which are decoupled from the relevant mechanical system through destructive interference [27, 28]. Dark modes in multimode optomechanical and electromechanical systems have been realized experimentally [13, 23, 41]. Another approach returns the mediating mechanical mode to its initial state, disentangling the mechanical mode from the rest of the system [24, 147].

The closed mechanical subsystem discussed in Section 8.2 (also see Fig. 8.1b) consists of three mechanical modes, including two resonator modes in the respective mechanical resonators, described by annihilation operators, $\hat{a}_1$and $\hat{a}_2$, and a waveguide mode, described by $\hat{b}$. For simplicity, we assume that the two resonator modes couple to the waveguide mode with equal coupling rate g and all three mechanical modes have the same resonance frequency, unless otherwise specified. Each resonator mode couples to either a single spin or an ensemble of spins. For the quantum state transfer between the two spin systems in the respective resonators, the interaction Hamiltonian is given by (Appendix H)

$$H_{\text{int}} = \hbar g \hat{b}^\dagger (\hat{a}_1 + \hat{a}_2) + \hbar \left[G_1(t) \hat{S}_1 \hat{a}_1^\dagger + G_2(t) \hat{S}_2 \hat{a}_2^\dagger \right] + \text{H.c.}, \tag{8.2}$$

where $\hat{S}_1$ and $\hat{S}_2$ describe the spin systems, as will be discussed in more detail later, and $G_1(t)$ and $G_2(t)$ are the corresponding spin-mechanical coupling rates. Note that spin qubits in a given resonator can couple to various mechanical modes of the resonator. As discussed in Section 8.2.1 II.A, the mode selection for the spin-mechanical coupling is set by the detuning between the external laser driving fields or by the frequency of the microwave driving field.

We assume that the relevant mechanical modes in the two resonators are cooled to their motional ground state. This can be achieved via resolved sideband cooling using a phonon-assisted optical transition [132], along with cryogenic cooling. Because

of the protection provided by the 2D phononic crystal shield, the mechanical damping rate, γ, can in principle be much smaller than the relevant coupling rate such that mechanical losses can be ignored during the transfer process. With $G \ll k_B T/\hbar Q_m$, the effects of thermal heating during the transfer process can also be negligible. For $T = 1$ K and G on the order of 0.1 MHz, this requires $Q_m \gg 10^5$, a regime readily achievable in state-of-the-art phononic nanostructures.

We consider two quantum state transfer schemes based on the use of single spins and spin ensembles, respectively. Both schemes return the waveguide mode to its initial state and are thus independent of the initial state of the waveguide. Since the effects of heating are assumed to be negligible and the schemes are independent of the initial state of the waveguide, we calculate the transfer fidelity at zero temperature and examine other relevant limiting factors.

8.3.1. Quantum state transfer between single spins

For the single-spin based transfer scheme, we assume $(G_1, G_2) \gg g$. The spin operator in Eq. 8.2 corresponds to the lowering operator for a single spin, with $\hat{S} = \hat{\sigma} = |-\rangle\langle+|$. The single spin, which servers as a communication qubit, can be positioned near the node of the resonator mode, where the spin-mechanical coupling reaches its maximum value. For the resonant Raman process shown in Fig. 8.2b, the effective spin-mechanical coupling rate for a single spin is given by $G = g_s \Omega_+ \Omega_- / (4|\Delta_+|\omega_m)$ [130]. With estimated $D = 5$ eV and $x_{\mathrm{zpf}} = 0.75 \times 10^{-15}$ m, we have $G/2\pi = 0.1$ MHz, where we take $\Omega_+/2\pi = \Omega_-/2\pi = 0.6$ GHz, $\Delta_+/2\pi = 3$ GHz, and $\omega_m/2\pi = 1$ GHz.

As shown in Fig. 8.5, the state transfer between the two spin systems can take place in a simple triple-swap process. For the first swap, we set $G_2 = 0$ and turn

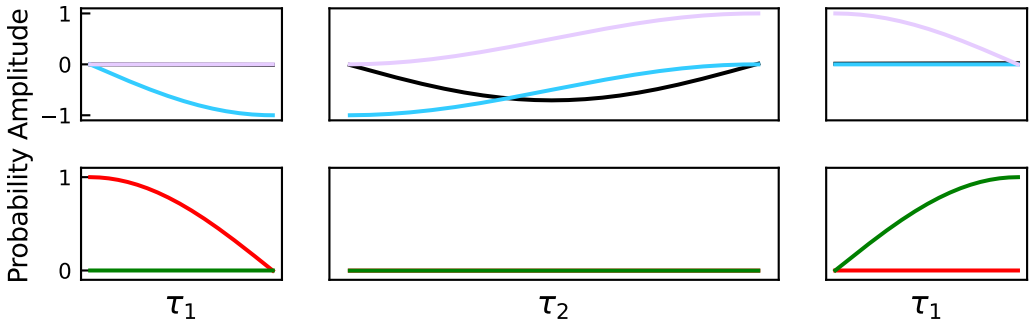

FIGURE 8.5. Time evolution of the mechanical and spin systems with $G/g = 100$ during the three successive swaps, with the same peak value G for both G_1 and G_2. Top: resonator mode 1 (blue), resonator mode 2 (purple), and waveguide mode (black). Bottom: spin 1 (red) and spin 2 (green).

on G_1 for a duration $\tau_1 = \pi/2G_1$, mapping the spin state for $\hat{S}_1$ to the state for $\hat{a}_1$. For the second swap, we set $G_1 = G_2 = 0$. After a duration $\tau_2 = \pi/\sqrt{2}g$, the state of $\hat{a}_1$ is effectively mapped to that of $\hat{a}_2$ [147]. This waveguide-mediated mapping between the two mechanical resonators leaves the state in the waveguide unchanged, as shown in Fig. 8.5. For the third swap, we set $G_1 = 0$ and turn on G_2 for a duration $\tau_3 = \pi/2G_2$, mapping the state from $\hat{a}_2$ to $\hat{S}_2$.

The unavoidable coupling to the waveguide mode during the swaps between the single spin and the resonator modes (i.e. the first and the third swap) limits the fidelity of the overall quantum state transfer, which is defined as $\mathcal{F} = \mathrm{Tr}\left[\left(\sqrt{\rho(t_i)}\rho(t_f)\sqrt{\rho(t_i)}\right)^{1/2}\right]^2$ [148]. Figure 8.6a shows the fidelity, with the initial state given by $|\psi(t_i)\rangle = |+\rangle\,|-\rangle\,|0,0,0\rangle$,as a function of G/g where G is the peak value for both G_1 and G_2. High fidelity can be achieved only when $G/g \gg 1$, which is difficult to achieve experimentally. Figure 8.6b also plots the fidelity when the duration of the $\pi/2$ pulses deviates from the ideal value. For relatively small G/g, the maximum fidelity actually occurs away from the zero deviation, $\epsilon = 0$. This is because for the phononic network, g is a constant. The mechanical resonators remain coupled to the waveguide in the first and the third swap of the state transfer process.

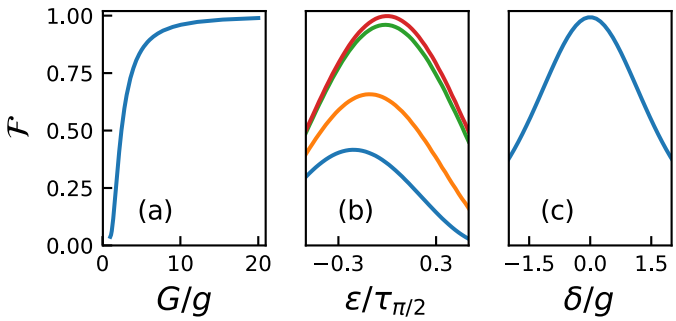

FIGURE 8.6. Fidelity for the triple-swap quantum state transfer with an initial state $|+\rangle|-\rangle|0,0,0\rangle$. (a) As a function of G/g. (b) As a function of the deviation from the $\pi/2$ pulses. From top to bottom, $G/g = 50$, 10, 3, 2. (c) As a function of the detuning between the waveguide and the two resonator modes, with $G/g = 25$. Ideal pulse duration and detuning are used unless otherwise specified. No other decoherence processes are included.

In the limit that $G/g \gg 1$, the maximum fidelity occurs at $\epsilon = 0$, as shown in Fig. 8.6b.

Detuning between the individual mechanical modes can also limit the fidelity of the state transfer. Here we can assume that the single spin couples resonantly to the respective resonator mode since the corresponding detuning is set by the frequency of the driving lasers. Figure 8.6c shows the fidelity as a function of the detuning, δ, between the waveguide and the two resonator modes (which are assumed to have equal frequency). As expected, high fidelity is achieved when the detuning is small compared with g.

8.3.2. Quantum state transfer between spin ensembles

For the spin-ensemble based transfer scheme, the spin operator in Eq. 8.2 corresponds to the collective lowering operator for a spin ensemble, with

$$\hat{S} = \frac{1}{\sqrt{\langle \sum_m \left(|-\rangle\langle -| - |+\rangle\langle -|\right)_m \rangle}} \sum_m \hat{\sigma}_m. \tag{8.3}$$

Ground-state spin-strain coupling of SiV or GeV centers can be used to avoid large optical inhomogeneous broadening of the NV centers. Alternatively, a relatively large optical dipole detuning, Δ, can be used for the ensemble NV centers. For sufficiently weak coupling of the individual spins, we can approximate $\hat{S}$ as a bosonic operator, with $\left[\hat{S}, \hat{S}^{\dagger}\right] = 1$. Similar approximations for spin ensembles have also been used for thermally-robust quantum state transfer in an optical network [90, 91]. In this limit, the overall system can be approximated as a set of linearly coupled harmonic oscillators.

With $G_1 = G_2 = G$, the interaction Hamiltonian can be written in terms of super modes, with $\hat{a}_{\pm} = \left(\hat{a}_1 \pm \hat{a}_2\right)/\sqrt{2}$ and $\hat{S}_{\pm} = \left(\hat{S}_1 \pm \hat{S}_2\right)/\sqrt{2}$, and with the form

$$H_{\text{int}} = \sqrt{2}\hbar g \hat{b}^{\dagger}\hat{a}_{+} + \hbar G\left(\hat{S}_{+}^{\dagger}\hat{a}_{+} + \hat{S}_{-}^{\dagger}\hat{a}_{-}\right) + \text{H.c.}. \tag{8.4}$$

The corresponding Heisenberg equations can be solved analytically. The time evolution of $\hat{S}_1$ is given by

$$\begin{aligned}\hat{S}_1(t) = \frac{gG}{\Gamma^2}\left[\cos\left(\Gamma t\right) - 1\right]\hat{b} - \frac{iG}{\sqrt{2}\Gamma}\sin\left(\Gamma t\right)\hat{a}_{+} - \frac{i}{\sqrt{2}}\sin\left(Gt\right)\hat{a}_{-} \\ + \frac{1}{\sqrt{2}}\left[1 + \frac{G^2}{\Gamma^2}\left(\cos\left(\Gamma t\right) - 1\right)\right]\hat{S}_{+} + \frac{1}{\sqrt{2}}\cos\left(Gt\right)\hat{S}_{-},\end{aligned} \tag{8.5}$$

where $\Gamma = \sqrt{2g^2 + G^2}$.

For the case that $\Gamma = 2nG$, where n is a positive integer, $\hat{S}\left(t = \pi/G\right) = \hat{S}_2$, as can be seen from Eq.8.5, which enables a perfect state transfer between the two spin systems, provided that $\hat{S}$ can be approximated as a bosonic operator. This state transfer process is independent of the initial states of the two mechanical resonators as well as the initial state of the phononic crystal waveguide.

To gain further physical insights into the quantum state transfer process, we plot in Fig. 8.7 the dynamics of the constituent mechanical and spin-ensemble systems under a constant spin-mechanical coupling. For simplicity, we assume that at $t = 0$, the occupation in $\hat{S}_1$, $\hat{a}_1$, and $\hat{b}$ is 1 and that in $\hat{S}_2$ and $\hat{a}_2$ is 0. As shown in Figs. 8.7a (with $\Gamma = 2G$) and 8.7b (with $\Gamma = 4G$), an effective π-pulse (with duration $\tau = \pi/G$) swaps the quantum states of the two spin systems as well as those of the two mechanical resonator modes and returns the waveguide mode to its initial state. Because of the bosonic approximation of the spin ensembles, the dynamics of the constituent mechanical and spin ensembles occurs simultaneously with that between the two mechanical resonator modes. This state swapping process, which arises from the special periodic dynamics of the system, is independent of the phonon occupation or distribution in the individual mechanical modes (waveguide or resonator modes) and keeps the mechanical and the spin systems disentangled. In this regard, the state transfer is robust against the overall thermal environment.

The above state transfer scheme requires a careful tuning of the spin-mechanical coupling rate, G, to satisfy the condition $\Gamma = 2nG$. Nevertheless, the quantum state transfer process can tolerate considerable deviations of G from its targeted or optimal value. As shown in Fig. 8.8a, even with a deviation as large as 6%, the fidelity of the state transfer calculated with the effective Hamiltonian given in Eq. 8.4 can still exceed 0.99 (see the shaded area in Fig. 8.8a).

In the limit that $\Gamma \gg G$ (which implies $G \ll g$), the fast dynamics of the "+" super-modes interacting with mode $\hat{b}$ effectively average to zero. As a result, the time evolution of mode $\hat{b}$ has negligible effects on the dynamics of the spin system, as shown in Fig. 8.7c. In this case, the time evolution can be described by the effective

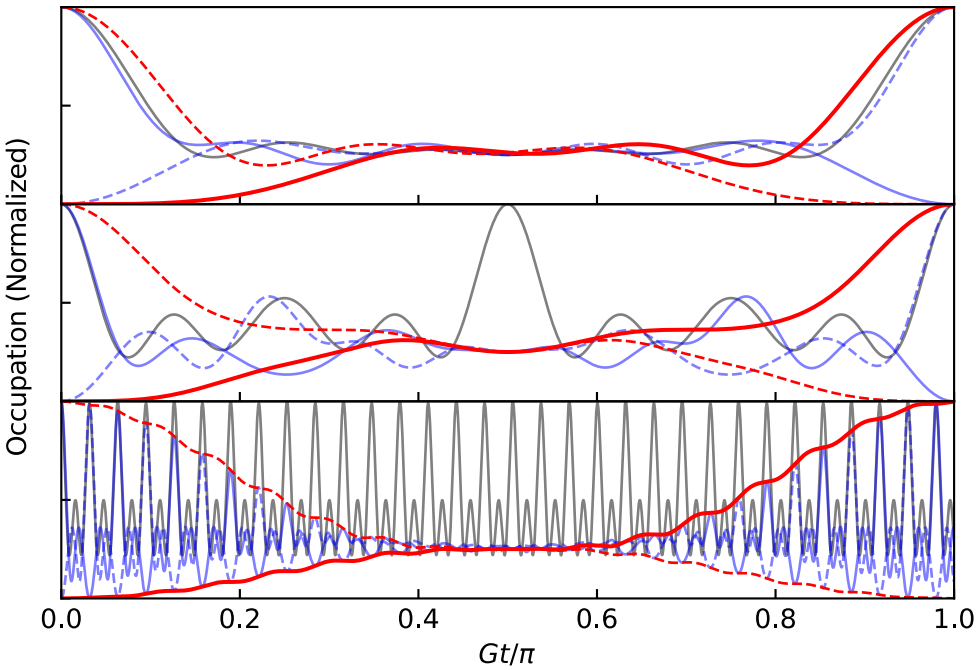

FIGURE 8.7. Time evolution of the mechanical and spin-ensemble systems under a constant spin-mechanical coupling, with the initial states specified in the text. Red lines: two spin ensembles. Blue lines: two resonator modes. Grey line: the waveguide mode. Top panel: $\Gamma/G = 2$. Middle panel: $\Gamma/G = 4$. Bottom panel: $\Gamma/G = \sqrt{1001}$. For both the top and middle panels, the complete state swap between the spin ensembles is accompanied by that between the resonator modes.

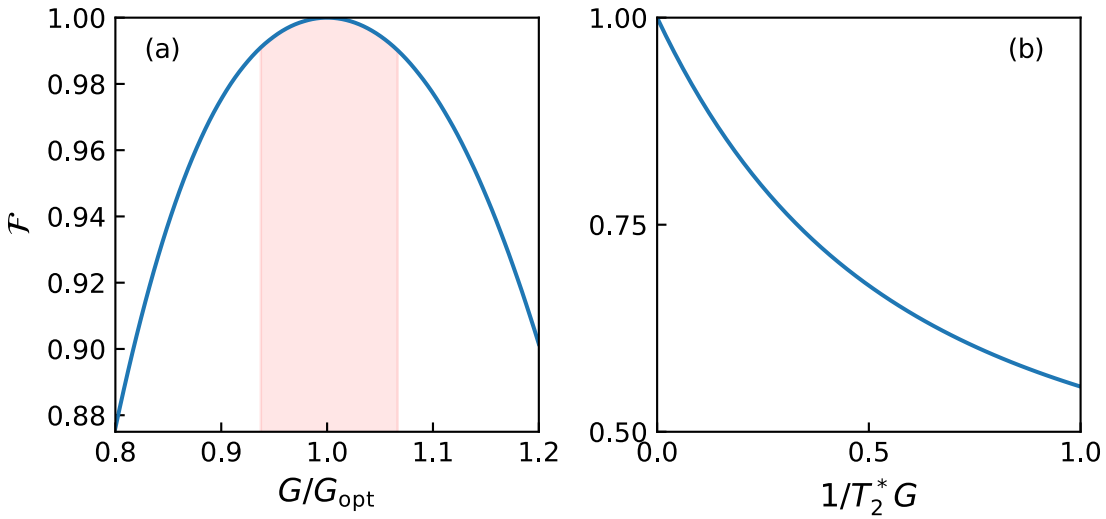

FIGURE 8.8. (a) Fidelity of spin-ensemble based quantum state transfer as a function of G, with $\Gamma/G_{\text{opt}} = 4$ and with the initial states being the same as those used for Fig. 8.7. No decoherence processes are included. (b) Fidelity of the spin-ensemble based quantum state transfer as a function of the spin dephasing rate, with $G \ll g$ and spin lifetime $= 10000/G$. The fidelity is averaged over all possible initial states. No other decoherence processes are included.

Hamiltonian

$$H_{\text{eff}} = \hbar G \left(\hat{S}_-^\dagger \hat{a}_- + \hat{S}_- \hat{a}_-^\dagger \right). \tag{8.6}$$

The complete state swap between the two spin systems can now occur to the zeroth order of the small parameter G/g, with $\hat{S}(t = \pi/G) = \hat{S}_2$ and without the requirement that $\Gamma = 2nG$.

In the regime of $G \ll g$, spin dephasing induced by the nuclear spin bath becomes a major limiting factor for the quantum state transfer process. Figure 8.8b shows the fidelity for the state transfer as a function of the spin dephasing time, T_2^*, calculated with the effective Hamiltonian given in Eq. 8.6 and the corresponding density matrix equations. As expected, high fidelity can only be achieved when $1/T_2^*$ is small compared with G. In addition to the use of isotopically purified diamond

[149], spin dephasing can also be greatly suppressed with the use of dressed, instead of bare, spin states [150, 151].

8.4. Summary and Outlook

In summary, we have developed theoretically a phononic network of solid state spins, in which a given spin-mechanical resonator is coupled to two distinct phononic crystal waveguides. The specially designed band gaps in the alternating waveguides enable bidirectional, but frequency-selective coupling, leading to a new architecture for quantum networks. In this architecture, any two neighboring nodes and the waveguide between them can form a closed subsystem. This conceptually-simple architecture overcomes the inherent obstacles in scaling up phononic quantum networks and avoids the technical difficulty of employing chiral spin-phonon interactions. The proposed phononic quantum network thus provides a promising route for developing quantum computers that can take advantage of robust spin qubits.

We have considered two specific approaches for quantum state transfer between spin systems in neighboring quantum nodes, using single spins and spin ensembles, respectively. An ensemble-spin based protocol, which requires a special ratio between the spin-mechanical and waveguide-resonator coupling rates, can be independent of the initial states of all the mechanical modes involved and thus be robust against the thermal environment. Note that these schemes are intended to illustrate examples of spin-mechanical interactions that can be used for the proposed phononic quantum networks. By using closed subsystems as building blocks, the phononic network can exploit and adopt a variety of quantum state transfer schemes.

While the discussions in this paper use, as a specific example, color centers in diamond, the implementation can be applied or extended to other defect centers or solid-state spin systems such as SiC-based systems [152]. Furthermore, the general architecture and the specific approach of alternating, frequency-selective coupling can be extended to microwave networks of superconducting circuits as well as to photonic networks, and also to 2D quantum networks, for which the implementation of surface codes becomes possible [153].

CHAPTER IX

CONCLUSIONS AND OUTLOOK

9.1. Conclusions

We have studied thermally robust multimode optomechanical interactions in several configurations. Thermal robustness is achieved with one of two methods - the generation of a dark state, or the use of stroboscopic system evolution.

In chapter V, we experimentally demonstrated the formation of a mechanically dark optical mode. The presence of such a dark mode results in a thermally robust state transfer between the two optical modes. However, with the relatively low cooperativities in our experiment, the transfer efficiency is low. In chapter VI, we experimentally demonstrate the formation of an optically dark mechanical mode. The mechanical modes are turned dark by controlling the relative phase of the driving fields, and provides a new avenue for controlling optomechanical interactions in multimode systems.

The theoretical analysis of Chapter VII demonstrates the feasibility of generating two-mode optical entanglement through a noisy, thermally driven mechanical mode. The robustness of the entanglement is a consequence of the stroboscopic evolution of the mechanical mode. The ability to generate entanglement in an optomechanical cavity can serve as an important resource for on-chip quantum circuits.

In Chapter VIII, we propose a new architecture for a quantum network. The nodes of the network are spin-mechanical resonators, and the communication channels are mechanical waveguides. Using mechanical modes for the network has several advantages over optics, but has the additional technical challenge of thermal noise.

Again, in this truly multimode system, we are able to overcome the issues of a thermally excited waveguide using a stroboscopic system evolution.

9.2. Future Work

Our experimental demonstrations of dark modes were done with low cooperativity systems. Such systems are sufficient for observing the dark modes, but to make use of them requires higher cooperativity systems. There is a clear path forward, using micromechanical resonators with phononic shields instead of the breathing or acoustic modes of the fused silica microspheres. The boost in cooperativity that is possible with these mechanical resonators will enable high-fidelity state-transfer through the formation of dark modes, and provides a path for realizing other interesting processes, for example Landau-Zener adiabatic transfer.

The spin-mechanical network discussed in Chapter VIII marries concepts from optomechanics with the budding field of spin-mechanics. High-impact experimental demonstrations are likely right around the corner. The potential for spin-mechanical systems to provide a new architecture for quantum computations makes this line of research very exciting. In the short term, demonstrating an interaction between spins and a mechanical resonator is within reach. A system with observable spin-mechanical interactions also provides the fastest route for characterizing the mechanical properties of the system. Once such interactions can be observed, designing and measuring small networks will be possible.

APPENDIX A

MATHEMATICAL DEFINITIONS AND CONVENTIONS

The Fourier transform of a function $x(t)$ is defined here as

$$x(\omega) = \int_{-\infty}^{\infty} \mathrm{d}t\, e^{i\omega t} x(t), \tag{A.1}$$

where $\omega = 2\pi f$ is the angular frequency. The inverse equation is then

$$x(t) = \frac{1}{2\pi} \int_{-\infty}^{\infty} d\omega\, e^{-i\omega t} x(\omega). \tag{A.2}$$

From equation A.1, it can be seen that

$$[x(\omega)]^* = x^*(-\omega). \tag{A.3}$$

In terms of the Fourier transform, the Dirac delta function is

$$\delta(\omega) = \frac{1}{2\pi} \int_{-\infty}^{\infty} dt\, e^{i\omega t} \tag{A.4}$$

Noisy signals are characterized by their statistical properties. For a stationary process (one in which the statistical properties are time-translation invariant), the autocorrelation function is denoted

$$G_{xx}(\tau) = \langle x(t+\tau) x(t) \rangle. \tag{A.5}$$

The power spectral density (PSD) is a measure of the power at each frequency component in the signal, and is given by the Fourier transform of the autocorrelation

function

$$S_{xx}(\omega) = \int_{-\infty}^{\infty} dt\, e^{i\omega t} G_{xx}(t). \tag{A.6}$$

Using equations A.2, A.5, and A.4, one finds the alternate form

$$S_{xx}(\omega) = \int_{-\infty}^{\infty} \frac{d\omega'}{2\pi} \langle x(\omega) x(\omega') \rangle. \tag{A.7}$$

Under the assumption that $G_{xx}(t)$ is stationary, we may also write

$$\langle x(\omega) x(\omega') \rangle = 2\pi S_{xx}(\omega) \delta(\omega + \omega'), \tag{A.8}$$

which leads to

$$S_{xx}(\omega) = \langle x(\omega) x(-\omega) \rangle = \langle |x(\omega)|^2 \rangle. \tag{A.9}$$

The inverse of equation A.6 gives the autocorrelation function in terms of the PSD

$$G_{xx}(t) = \frac{1}{2\pi} \int_{-\infty}^{\infty} d\omega\, e^{-i\omega t} S_{xx}(\omega). \tag{A.10}$$

From equation A.6, one finds

$$\langle x^2 \rangle = \frac{1}{2\pi} \int_{-\infty}^{\infty} d\omega\, S_{xx}(\omega). \tag{A.11}$$

APPENDIX B

DAMPED OSCILLATOR EQUATIONS OF MOTION

A damped quantum harmonic oscillator obeys the equations of motion

$$\dot{\hat{p}} = F - m\omega_m \hat{x} - \gamma \hat{p} \tag{B.1a}$$

$$\dot{\hat{x}} = \hat{p}/m \tag{B.1b}$$

Using equations 2.28 allows us to write corresponding equations for $\hat{b}$ and $\hat{b}^\dagger$, which have the form

$$\dot{\hat{b}} = -i\omega_m \hat{b} - \frac{\gamma}{2}\hat{b} + \frac{\gamma}{2}\hat{b}^\dagger + \frac{i}{2m\omega_m x_{zpf}} F \tag{B.2a}$$

$$\dot{\hat{b}}^\dagger = i\omega_m \hat{b}^\dagger - \frac{\gamma}{2}\hat{b}^\dagger + \frac{\gamma}{2}\hat{b} - \frac{i}{2m\omega_m x_{zpf}} F \tag{B.2b}$$

Equations B.2 show that $\hat{b}$ has a resonance at at $+\omega_m$, while $\hat{b}^\dagger$ has a resonance at $-\omega_m$. The two couple to each other at a rate $\gamma/2$. Since the coupled equations are linear, we may consider the case of a monochromatic drive $F = -2im\omega_m x_{zpf}\sqrt{\gamma}(b_{in}e^{-i\omega_D t} - b_{in}^\dagger e^{i\omega_D t})$. An appreciable response occurs when $\omega_D \approx \omega_m$. If we take $\omega_D = \omega_m$, the equations of motion become

$$\dot{\hat{b}} = -\frac{\gamma}{2}\hat{b} + \frac{\gamma}{2}\hat{b}^\dagger e^{2i\omega_m t} + \sqrt{\gamma}\left(b_{in} - b_{in}^\dagger e^{2i\omega_m t}\right) \tag{B.3a}$$

$$\dot{\hat{b}}^\dagger = -\frac{\gamma}{2}\hat{b}^\dagger + \frac{\gamma}{2}\hat{b}e^{-2\omega_m t} - \sqrt{\gamma}\left(b_{in}e^{-2i\omega_m t} - b_{in}^\dagger\right) \tag{B.3b}$$

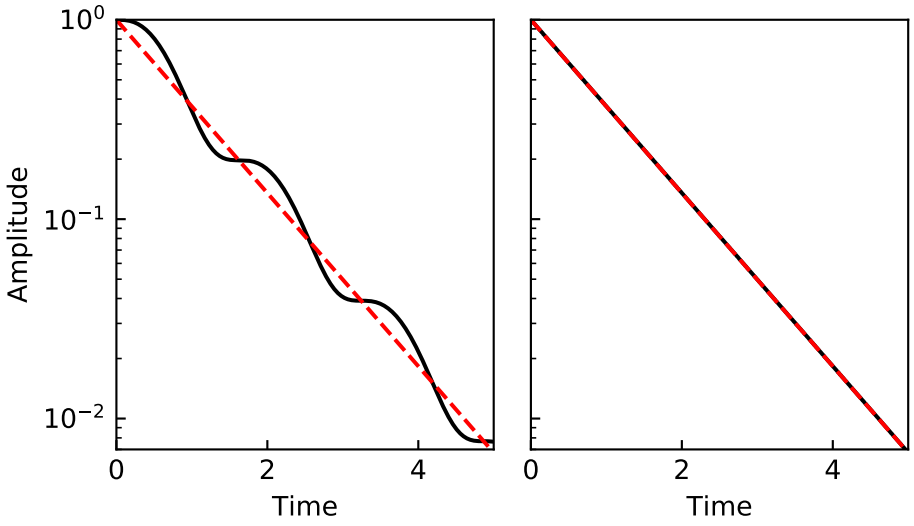

FIGURE B.1. Comparison of the exact time evolution of equation B.3 (solid lines) to the approximate evolution of equation B.4 (dashed lines). The solution is shown for $b(t)$, with $b(0) = 1$ and $F = 0$. In the left panel, $Q = 2$, while the right panel has $Q = 200$. Experimental systems we study have $Q > 10^4$, and certain systems have achieved $Q > 10^{10}$.

in a frame defined by $\hat{b} \rightarrow \hat{b}e^{-i\omega_m t}$. When $\gamma \ll \omega_m$, we make a rotating wave approximation, and the resulting equations of motion in the lab frame are

$$\dot{\hat{b}} = -i\omega_m \hat{b} - \frac{\gamma}{2}\hat{b} + \sqrt{\gamma} b_{in} \tag{B.4a}$$

$$\dot{\hat{b}}^\dagger = i\omega_m \hat{b}^\dagger - \frac{\gamma}{2}\hat{b}^\dagger + \sqrt{\gamma} b_{in}^\dagger. \tag{B.4b}$$

The experimental systems we study have mechanical quality factors $Q > 10^4$. As a result, equations B.4 are a very good approximation to the exact equations of motion.

APPENDIX C

OSCILLATING CAVITY EXACT SOLUTION

For completeness, we show here the exact solution for an optical cavity where the end mirror oscillates as

$$x(t) = x_0 \cos(\omega_m t). \tag{C.1}$$

If the cavity is driven by a laser input $a_{in}(t) = a_{in} e^{-i\omega_L t}$, then in a frame rotating at ω_L, the equation of motion for the cavity is

$$\dot{a} = \left(i\Delta - iGx_0 \cos(\omega_m t) - \frac{\kappa}{2} \right) a + \sqrt{\kappa_{ex}} a_{in}. \tag{C.2}$$

This is an inhomogeneous linear first-order differential equation, which can be solved exactly via integration factor. The general solution is

$$a(t) = a(t_0) e^{\mu(t;t_0)} + e^{\mu(t)} \int_{t_0}^{t} dt' \, \sqrt{\kappa_{ex}} a_{in} e^{-\mu(t')}, \tag{C.3}$$

where $\mu(t)$ is the indefinite integral

$$\mu(t) = \int dt \, \left(i\Delta - iGx_0 \cos(\omega_m t) - \frac{\kappa}{2} \right) \tag{C.4}$$

$$= \left(i\Delta - \frac{\kappa}{2} \right) t - i\beta \sin(\omega_m t), \tag{C.5}$$

and $\mu(t; t_0)$ is the definite integral

$$\mu(t; t_0) = \int_{t_0}^{t} dt \, \left(i\Delta - iGx_0 \cos(\omega_m t) - \frac{\kappa}{2} \right) \tag{C.6}$$

$$= \left(i\Delta - \frac{\kappa}{2} \right) (t - t_0) - i\beta \left(\sin(\omega_m t) - \sin(\omega_m t_0) \right), \tag{C.7}$$

where $\beta = Gx_0/\omega_m$. We are interested in the steady-state behavior or the system, and so we consider the case $t_0 \to -\infty$. Under this assumption, the term $a(t_0)e^{\mu(t;t_0)}$ can be dropped. To integrate the remaining term, we make use of the Bessel function property

$$e^{\frac{x}{2}\left(t-\frac{1}{t}\right)} = \sum_{n=-\infty}^{\infty} J_n(x)t^n. \tag{C.8}$$

By writing $\sin(\omega_m t) = i\frac{1}{2}\left(e^{-i\omega_m t} - e^{i\omega_m t}\right)$ and making the associations $\beta = x$ and $t = e^{i\omega_m t}$, we find

$$e^{i\beta\sin(\omega_m t)} = \sum_{n=-\infty}^{\infty} J_n\left(\beta\right) e^{in\omega_m t}. \tag{C.9}$$

Performing the integral in equation C.3 then leads to the solution

$$a(t) = \sqrt{\kappa_{ex}}a_{in} \sum_{n=-\infty}^{\infty} \frac{J_n\left(\beta\right)}{-i\Delta + \frac{\kappa}{2} + in\omega_m} e^{i[n\omega_m t - \beta\sin(\omega_m t)]}. \tag{C.10}$$

For $\beta \ll 1$, $J_0(\beta) \approx 1$ and $J_{\pm 1}(\beta) \approx \pm\beta/2$, and we arrive at the intracavity field to first order in β

$$a(t) \approx \sqrt{\kappa_{ex}}a_{in}\mathcal{L}(0)\left(1 - \frac{i\beta\omega_m\mathcal{L}(\omega_m)}{2}e^{-i\omega_m t} - \frac{i\beta\omega_m\mathcal{L}(-\omega_m)}{2}e^{i\omega_m t}\right), \tag{C.11}$$

with

$$\mathcal{L}(\omega) = \frac{1}{-i\left(\Delta + \omega\right) + \kappa/2}, \tag{C.12}$$

which is equation 2.41. The cavity output, given by the input-output relation of equation 2.7, is written as

$$a_{\text{out}} = a_{\text{in}}\left\{\mathcal{R}(0) + \frac{i\beta\omega_m\kappa_{\text{ext}}}{2}\mathcal{L}(0)\left[\mathcal{L}(\omega_m)e^{-i\omega_m t} + \mathcal{L}(-\omega_m)e^{i\omega_m t}\right]\right\}, \tag{C.13}$$

where

$$\mathcal{R}(0) = \frac{\kappa/2 - \kappa_{\text{ext}} - i\Delta}{\kappa/2 - i\Delta}. \tag{C.14}$$

APPENDIX D

TRANSDUCTION FUNCTIONS

Here we calculate the transduction functions for direct detection of breathing and SAW mechanical modes. In general, the resonance frequency depends on the amplitude of the mechanical mode. We always assume the mechanical mode induces only a small shift in the resonance frequency, so that we may write the shift as a first order Taylor expansion

$$\omega_c(x) = \omega_c + Gx(t). \tag{D.1}$$

We are interested in the fluctuations of the resonance frequency around its average, which we define as

$$\delta\omega = Gx(t). \tag{D.2}$$

By equation A.9, the PSD for the cavity resonance is proportional to the PSD of the mechanical mode,

$$S_{\delta\omega\delta\omega} = G^2 S_{xx}. \tag{D.3}$$

Fluctuations in the cavity resonance induce fluctuations in the phase of the output field, which can be detected with any phase-dependent measurement scheme.

The phase-dependent measurement scheme we use is direct detection, which, as the name implies, involves directly measuring the power at the output of the cavity. To see how direct detection of a cavity oscillating as $x(t) = x_0 \cos(\omega t)$ works, we write the output of the optical cavity, in a frame rotating at the laser frequency, as

$$a_{\text{out}}(t) = a_{\text{in}} \left(A_0 + \psi A_+ e^{-i\omega t} + \psi A_- e^{i\omega t} \right), \tag{D.4}$$

with $\psi = Gx_0/\omega$ (see, for example, equation C.13). The power at the output is $P_{\text{out}} = \hbar\omega_L|a_{\text{out}}|^2$, and we measure only the component of P_{out} that oscillates at frequency ω, which is

$$P_{\text{out}}^{(\omega)} = P_{\text{in}}\psi\left(A_0^* A_+ + A_0 A_-^*\right)e^{-i\omega t} + \text{c.c.} \tag{D.5}$$

Writing $A_0^* A_+ + A_0 A_-^* = Re^{i\Phi}$ leads to the alternative form

$$P_{\text{out}}^{(\omega)} = \frac{2P_{\text{in}}GR}{\omega}x_0\cos(\omega t + \Phi), \tag{D.6}$$

where $R = |A_0^* A_+ + A_0 A_-^*|$ and $\Phi = \text{Arg}[A_0^* A_+ + A_0 A_-^*]$. The power spectral density of the output power, S_{PP}, as measured by the spectrum analyzer, is then

$$S_{PP}(\omega) = 4\frac{P_{\text{in}}^2 G^2}{\omega^2}|A_0^* A_+ + A_0 A_-^*|^2 S_{xx}(\omega) \tag{D.7}$$

$$= \frac{P_{\text{in}}^2 G^2}{\omega^2}K(\omega)S_{xx}(\omega). \tag{D.8}$$

The function $K(\omega)$ is the transduction function, a unitless function which depends on the properties of the cavity, as well as the detuning of the laser and frequency ω.

D.1. Breathing Mode Transduction Function

From equation C.13, we identify

$$A_0 = \mathcal{R}(0) \tag{D.9}$$

$$A_\pm = \frac{i\omega\kappa_{\text{ext}}\mathcal{L}(0)\mathcal{L}(\pm\omega)}{2}. \tag{D.10}$$

The lineshape and reflection functions, repeated here for convenience, are

$$\mathcal{L}(\omega) = \frac{1}{-i(\Delta+\omega)+\kappa/2} \tag{D.11}$$

and

$$\mathcal{R}(\omega) = \frac{\kappa/2-\kappa_{\text{ext}}-i(\Delta+\omega)}{\kappa/2-i(\Delta+\omega)}. \tag{D.12}$$

After some algebra, one finds

$$A_0^* A_+ + A_0 A_-^* = \frac{i\omega\kappa_{\text{ext}}\Delta\left[\omega+i(\kappa-\kappa_{\text{ext}})\right]}{\left(\left(\frac{\kappa}{2}\right)+i(\Delta+\omega)\right)\left(\left(\frac{\kappa}{2}\right)^2+i(\Delta-\omega)\right)\left(\left(\frac{\kappa}{2}\right)^2+\Delta^2\right)}, \tag{D.13}$$

leading to the transduction function for breathing modes

$$K_D(\omega) = \frac{4\omega^2\kappa_{\text{ext}}^2\Delta^2\left[\omega^2+(\kappa-\kappa_{\text{ext}})^2\right]}{\left(\left(\frac{\kappa}{2}\right)^2+(\Delta+\omega)^2\right)\left(\left(\frac{\kappa}{2}\right)^2+(\Delta-\omega)^2\right)\left(\left(\frac{\kappa}{2}\right)^2+\Delta^2\right)^2}. \tag{D.14}$$

D.2. Brillouin Mode Transduction Function

For the Brillouin scattering case, we assume the laser is detuned near the lower of the two optical modes, which we call the pump mode. The pump mode has linewidth κ_L and external coupling $\kappa_{\text{ex},L}$. The two optical modes are separated in frequency by $\delta\omega$. If the pump laser is detuned by Δ_L from the pump mode, then it is detuned by $\Delta = \Delta_L - \delta\omega$ from the upper mode, referred to as the scattered mode. For such an

arrangement, the A_i are given by

$$A_- = 0 \tag{D.15}$$

$$A_0 = \frac{\kappa_L/2 - \kappa_{\mathrm{ex,L}} - i\Delta_L}{\kappa_L/2 - i\Delta_L} \tag{D.16}$$

$$A_+ = \frac{i\sqrt{\kappa_{\mathrm{ext}}\kappa_{\mathrm{ex,L}}}\omega}{\left(\frac{\kappa_L}{2} - i\Delta_L\right)\left(\frac{\kappa}{2} - i(\omega+\Delta)\right)}. \tag{D.17}$$

In terms of $\mathcal{R}$ and $\mathcal{L}$, these functions are simply $A_0 = \mathcal{R}_L(0)$ and $A_+ = i\omega\sqrt{\kappa_{\mathrm{ext}}\kappa_{\mathrm{ex,L}}}\mathcal{L}_L(0)\mathcal{L}(\omega)$. The transduction function for Brillouin scattering is therefore

$$K_B(\omega) = 4\omega^2\kappa_{\mathrm{ext}}\kappa_{\mathrm{ex,L}}|\mathcal{R}_L(0)\mathcal{L}_L(0)\mathcal{L}(\omega)|^2, \tag{D.18}$$

or, expanding $\mathcal{R}$ and $\mathcal{L}$,

$$K_B(\omega) = \frac{4\kappa_{\mathrm{ext}}\kappa_{\mathrm{ex,L}}\omega^2\left[\Delta_L^2 + \left(\frac{\kappa_L}{2} - \kappa_{\mathrm{ex,L}}\right)^2\right]}{\left(\left(\frac{\kappa_L}{2}\right)^2 + \Delta_L^2\right)^2\left(\left(\frac{\kappa}{2}\right)^2 + (\Delta+\omega)^2\right)}. \tag{D.19}$$

APPENDIX E

SØRENSEN-MØLMER UNITARY EVOLUTION

Here, we derive the unitary evolution for the system of Chapter VII. The interaction Hamiltonian for the system is

$$H_I = (g_1 a_1 + g_2 a_2^\dagger) b^\dagger e^{i\Delta t} + \text{H.c.} \tag{E.1}$$

We assume from now on that the optomechanical coupling rates for the two optical modes are set equal, $g_1 = g_2 \equiv g$. We define dimensionless quadrature variables $x_i = (a_i + a_i^\dagger)/\sqrt{2}$, $x_b = (b + b^\dagger)/\sqrt{2}$, $p_i = i(a_i^\dagger - a_i)/\sqrt{2}$, and $p_b = i(b^\dagger - b)/\sqrt{2}$. From the optical field quadratures, we define two EPR variables $x \equiv x_1 + x_2$, and $p \equiv p_2 - p_1$, which satisfy $[x, p] = 0$ and can therefore be treated as numbers for the current treatment. In terms of these variables, the interaction Hamiltonian can be written in the form

$$H_I = f(t) x_b + g(t) p_b. \tag{E.2}$$

The time-dependent coeffecients of the mechanical degrees of freedom are

$$f(t) = g[x \cos(\Delta t) + p \sin(\Delta t)] \tag{E.3}$$

$$g(t) = g[x \sin(\Delta t) - p \cos(\Delta t)]. \tag{E.4}$$

We write the exact propagator by ansatz, assuming the form

$$U(t) = e^{-iA(t)} e^{-iF(t)x_b} e^{-iG(t)p_b}, \tag{E.5}$$

and solve for the functions $A(t), F(t)$, and $G(t)$ by enforcing that $U(t)$ satisfy the equation

$$i\frac{d}{dt}U(t) = H_I U(t). \tag{E.6}$$

In doing so, one finds the the solutions

$$\begin{aligned} F(t) &= \int_0^t \mathrm{d}t' f(t') \\ G(t) &= \int_0^t \mathrm{d}t' g(t') \\ A(t) &= -\int_0^t \mathrm{d}t' F(t') g(t') \end{aligned} \tag{E.7}$$

Following through the integration yields

$$\begin{aligned} F(t) &= \frac{g}{\Delta}[x\sin(\Delta t) - p\cos(\Delta t) + p] \\ G(t) &= \frac{g}{\Delta}[x - x\cos(\Delta t) - p\sin(\Delta t)] \end{aligned} \tag{E.8}$$

and

$$\begin{aligned} A(t) = -\frac{g^2}{\Delta^2}\Big(&\frac{t\Delta}{2}(x^2+p^2) \\ &+ \frac{1}{4}\sin(2\Delta t)(p^2-x^2) + \frac{px}{2}[\cos(2\Delta t) - 1] \\ &- px[\cos(\Delta t) - 1] - p^2\sin(\Delta t)\Big). \end{aligned} \tag{E.9}$$

The coefficients of the mechanical degrees of freedom oscillate in time, simultaneously returning to zero whenever the timing condition $t_n = 2\pi n/\Delta$ for integer n is satisfied. At those times, the remaining part of the propagator entangles the optical modes

with the operation of

$$A(t_n) = -\frac{g^2}{\Delta^2}\pi n(x^2 + p^2). \tag{E.10}$$

For optical states initially in the vacuum, the covariance matrix of the optical modes can be constructed, and a detailed calculation gives the logarithmic negativity

$$E_{\mathcal{N}} = -\frac{1}{2}\log_2\left(2r^2 - \sqrt{4r^8 + 8r^6 + 5r^4 + r^2} + 2r^4 + \frac{1}{4}\right) - 1 \tag{E.11}$$

where $r = \pi n g^2/\Delta^2$.

One may also consider the situation where 2-photon resonance is broken by detuning each laser drive to the same side of the respective sideband, i.e. $\Delta_1 = \Delta_2 = \Delta$. In this case, one finds the form of the Hamiltonian to still satisfy the Sørensen-Mølmer condition. However, the resulting Hamiltonian does not generate entanglement, and worse yet the system exhibits instability.

APPENDIX F

LOGARITHMIC NEGATIVITY

To quantify the entanglement between the optical modes of the system in Chapter VII, we use the logarithmic negativity. For two-mode Gaussian states described by annihilation operators a_i $(i = 1, 2)$ that satisfy the bosonic commutation relations $[a_i, a_j^\dagger] = \delta_{ij}$, the logarithmic negativity can be calculated from the expression

$$E_{\mathcal{N}} = \max\left(0, -\log_2 2\eta^-\right), \tag{F.1}$$

where

$$\eta^- = \frac{1}{\sqrt{2}}\sqrt{\Sigma - \sqrt{\Sigma^2 - 4\mathrm{det}V}}, \tag{F.2}$$

and

$$\Sigma = \mathrm{det}A + \mathrm{det}B - 2\mathrm{det}C. \tag{F.3}$$

The matrices A, B, and C are 2×2 blocks of the covariance matrix

$$V = \begin{pmatrix} A & C \\ C^{\mathrm{T}} & B \end{pmatrix}. \tag{F.4}$$

The components of the covariance matrix have the usual form

$$V_{ij} = \frac{1}{2}\langle \Delta\xi_i \Delta\xi_j + \Delta\xi_j \Delta\xi_i \rangle, \tag{F.5}$$

where $\Delta\xi_i = \xi_i - \langle\xi_i\rangle$, and $\vec{\xi} = [x_1, p_1, x_2, p_2]^{\mathrm{T}}$. The dimensionless quadrature variables x_i and p_i are constructed from the annihilation operators according to $x_i = (a_i + a_i^\dagger)/\sqrt{2}$ and $p_i = i(a_i^\dagger - a_i)/\sqrt{2}$.

From Eq. (F.1), one finds that the system becomes entangled when $\eta^- < 1/2$. In terms of the covariance matrix, the requirement for entanglement is $4 \det V < \Sigma - 1/4$, which is equivalent to Simon's partial transpose criterion [154].

APPENDIX G

PHONONIC NETWORK STRUCTURE DESIGN

G.1. Calculations of Normal Modes

We determine the frequencies and field patterns of the normal modes of the spin-mechanical resonators of Chapter VIII by solving the eigenvalue equation 2.16 using finite element numerical calculations. The material properties of diamond used are $E = 1050$ GPa, $\nu = 0.2$, and $\rho = 3539$ kg/m^3. All structures under study have mirror symmetries, as illustrated in Fig. G.1 The solutions of the wave equations will thus be eigenmodes of the symmetry operations. We organize the solutions as even or odd under reflection R_j about a plane perpendicular to the coordinate axis $j = x, y, z$. The specific symmetries of the structure are R_y and R_z. All modes considered in this work have even symmetry under R_z. Figure G.1 shows the displacement patterns of the third and fourth order compression modes of the thin diamond plate discussed in Fig. 8.2 of the main text.

G.2. Determination of Resonator-Waveguide Coupling Rates

We describe the coupling between the plate resonators and the phononic crystal waveguides by using a standard coupled-mode theory. The Hamiltonian for a pair of single-mode resonators connected by a waveguide is taken to be

$$H = \sum_n \left\{ \Delta_n \hat{b}_n^\dagger \hat{b}_n + \left[g_n \hat{b}_n^\dagger \left(\hat{a}_1 + (-1)^n \hat{a}_2 \right) + \text{H.c.} \right] \right\}, \tag{G.1}$$

written in a frame rotating at the resonator frequency, where $\hat{a}_1$ and $\hat{a}_2$ describe the two resonator modes with the same frequency, $\hat{b}_n$ describes the waveguide modes, g_n

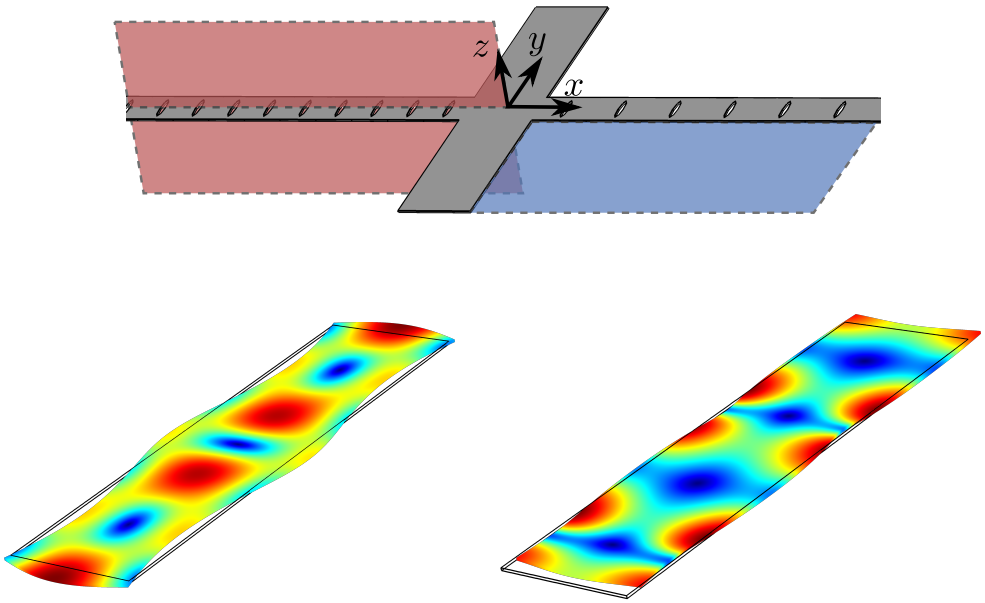

FIGURE G.1. Top: The reflection symmetry planes of the phononic network structure. The blue and red planes correspond to R_z and R_y, respectively. Bottom: Displacement patterns of the third order compression mode (left), with even R_y symmetry, and fourth order compression mode (right), with odd R_y symmetry.

is the resonator-waveguide coupling rate, and Δ_n is the frequency difference between the waveguide and the resonator modes. The sign difference on alternating modes reflects alternating symmetry of the eigenmodes in the waveguide. For a waveguide of length $L = 120$ μm, numerical simulations of the diamond waveguide structure used in this study give a mode spaceing of about 30 MHz. In the limit that g is much less than the mode spacing, only the resonant or nearly resonant waveguide mode $\hat{b}_0$ needs to be considered.

In the limit of a single waveguide mode, the (unnormalized) eigenmodes are $\psi_0 = a_1 - a_2$ and $\psi_\pm = 4gb_0 + (\Delta_0 \pm \Lambda)(a_1 + a_2)$, with corresponding eigenvalues $\lambda_0 = 0$, $\lambda_\pm = \frac{1}{2}(\Delta_0 \pm \Lambda)$, where $\Lambda = \sqrt{\Delta_0^2 + 8g^2}$. To determine the relevant resonator-waveguide coupling rates for the phononic network structure, we first calculate numerically the relevant eigenmodes of the full structure. As show in Fig. G.2 the eigenmodes occur

as triplets, which arise from the coupling between the unperturbed resonator and waveguide modes. From the frequencies of the given triplet, we can then determine both g and Δ_0, with

$$\Delta_0 = \lambda_+ + \lambda_- - 2\lambda_0, \tag{G.2}$$

and

$$g = \sqrt{\frac{(\lambda_+ - \lambda_-)^2}{8}}. \tag{G.3}$$

For the dimensions of the phononic network used in this work, the third order compression mode was determined to have $g = 9.0$ MHz and $\Delta_0 = -3.4$ MHz, while the fifth order compression mode has $g = 3.1$ MHz and $\Delta_0 = -1.9$ MHz. Further fine tuning of the resonator dimensions can reduce Δ_0 to be much smaller than g. The coupling rate can also be tuned or tailored by shaping the contact area between the plate resonator and the phononic crystal waveguide.

In the single-waveguide-mode limit, the eigenmode ψ_0 should have no contribution from the waveguide mode. As can been seen from the displacement patterns shown in Fig. G.2 there are still discernible contributions from the waveguide, which arise from the coupling of the resonators to the adjacent waveguide modes such as $b_{\pm 1}$. In order to avoid the coupling to multiple waveguide modes, the waveguide mode spacing needs to far exceed the waveguide-resonator coupling rate, which puts a limit on both the magnitude of g and the length of the waveguide. In the limit of long waveguides with g much greater than the mode spacing, quantum state transfer schemes similar to those proposed for optical networks can be used [90, 91]. For diamond-based phononic network, relatively short waveguides are preferred.

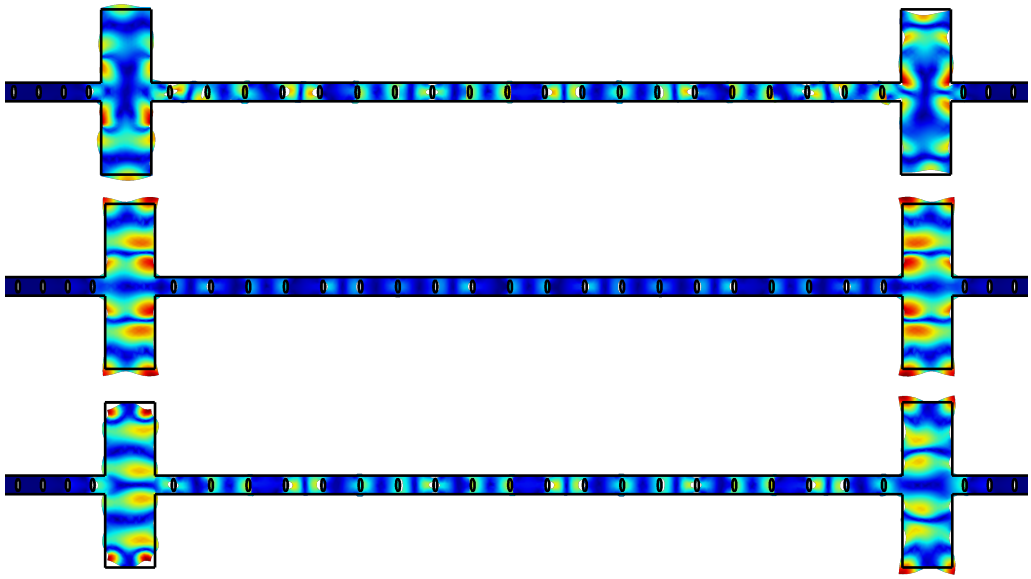

FIGURE G.2. Displacement patterns of three eigenmodes of the phononic network structure shown in Fig. 8.3 of the main text. The frequencies are (1.6737, 1.6791, 1.6826) GHz from top to bottom. The triplet arises from the coupling between the fifth order compression modes in the two neighboring plate resonators and the nearly resonant waveguide mode. The array of holes in the waveguide has a period of 6 μm.

APPENDIX H

DERIVATION OF SPIN-MECHANICAL HAMILTONIAN

We start with a 3-level lambda system with two laser drives, as depicted in Figure 8.2b. The component of the strain along the axis of the NV preserves the symmetry of the NV, and as a result, can only shift the energy levels (as opposed to causing mixing). The Hamiltonian for the i$^{\text{th}}$ laser-driven spin-mechanical node is

$$H_i = \omega_m a_i^\dagger a_i - \nu_- \left|-\right\rangle \left\langle -\right| - \nu_+ \left|+\right\rangle \left\langle +\right| + g_s \left(a_i^\dagger + a_i\right) \left|e\right\rangle \left\langle e\right| + \frac{\Omega_-}{2} \left[e^{-i\omega_- t} \left|e\right\rangle \left\langle -\right| + \text{H.c.}\right] + \frac{\Omega_+}{2} \left[e^{-i\omega_+ t} \left|e\right\rangle \left\langle +\right| + \text{H.c.}\right]. \quad \text{(H.1)}$$

To the node Hamiltonian, we apply a Schrieffer-Wolff transformation, with the form

$$U = \exp\left[-\frac{g_s}{\omega_m}(a_i^\dagger - a_i) \left|e\right\rangle \left\langle e\right|\right]. \quad \text{(H.2)}$$

Note that U is a displacement operator for a_i, meaning $U^\dagger a_i^{(\dagger)} U = a_i^{(\dagger)} - \frac{g_s}{\omega_m} \left|e\right\rangle \left\langle e\right|$. Under the Schrieffer-Wolff transformation, the Hamiltonian transforms to

$$H = \omega_m a_i^\dagger a_i - \nu_- \left|-\right\rangle \left\langle -\right| - \nu_+ \left|+\right\rangle \left\langle +\right| - \frac{g_s}{\omega_m} \left|e\right\rangle \left\langle e\right| + \sum_{n=\pm} \frac{\Omega_n}{2} \left[e^{-i\omega_m t + \frac{g_s}{\omega_m}(a_i^\dagger - a_i)} \left|e\right\rangle \left\langle n\right| + \text{H.c.}\right]. \quad \text{(H.3)}$$

The intrinsic strain coupling rate, g_s, is very small compared to the mechanical mode frequencies ω_m. Thus, the term $\frac{g_s}{\omega_m} \left|e\right\rangle \left\langle e\right|$ can be dropped, and the exponentials can be Taylor expanded to first order in the parameter g_s/ω_m. Then, for appropriate detunings for a resonant Raman process, one arrives at Equation 8.1.

When the spin-mechanical systems are connected to form a network, each node couples to a waveguide, which introduces the additional terms in Equation H.1

$$H_{\text{wg}} = \omega_b b^\dagger b + g\left(a_i b^\dagger + a_i^\dagger b\right). \tag{H.4}$$

Applying the Schrieffer-Wolff transformation leaves these new terms unchanged, but introduces an additional term $-\frac{gg_s}{\omega_m}(b^\dagger + b)\left|e\right\rangle\left\langle e\right|$. This additional term is a direct coupling between the spin and the waveguide that takes place in the transformed picture. For the designed network, $g_s \sim 3$ MHz, $g \sim 1$ MHz, and $\omega_m \sim 1$ GHz, leading to a coupling rate between the spin and the waveguide that is roughly 100 times slower than the coupling between the spin and the node mechanical mode. As a result, we drop this additional term.

REFERENCES CITED

[1] M. Rossi, D. Mason, J. Chen, Y. Tsaturyan, and A. Schliesser, "Measurement-based quantum control of mechanical motion," *arXiv preprint arXiv:1805.05087*, 2018.

[2] S. M. Meenehan, J. D. Cohen, G. S. MacCabe, F. Marsili, M. D. Shaw, and O. Painter, "Pulsed excitation dynamics of an optomechanical crystal resonator near its quantum ground state of motion," *Physical Review X*, vol. 5, no. 4, p. 041002, 2015.

[3] J. Teufel, T. Donner, D. Li, J. Harlow, M. Allman, K. Cicak, A. Sirois, J. D. Whittaker, K. Lehnert, and R. W. Simmonds, "Sideband cooling of micromechanical motion to the quantum ground state," *Nature*, vol. 475, no. 7356, p. 359, 2011.

[4] T. Purdy, K. Grutter, K. Srinivasan, and J. Taylor, "Quantum correlations from a room-temperature optomechanical cavity," *Science*, vol. 356, no. 6344, pp. 1265–1268, 2017.

[5] V. Sudhir, R. Schilling, S. A. Fedorov, H. Schuetz, D. J. Wilson, and T. J. Kippenberg, "Quantum correlations of light from a room-temperature mechanical oscillator," *Physical Review X*, vol. 7, no. 3, p. 031055, 2017.

[6] A. H. Safavi-Naeini, S. Gröblacher, J. T. Hill, J. Chan, M. Aspelmeyer, and O. Painter, "Squeezed light from a silicon micromechanical resonator," *Nature*, vol. 500, no. 7461, p. 185, 2013.

[7] T. Palomaki, J. Teufel, R. Simmonds, and K. Lehnert, "Entangling mechanical motion with microwave fields," *Science*, p. 1244563, 2013.

[8] H. Xu, D. Mason, L. Jiang, and J. Harris, "Topological energy transfer in an optomechanical system with exceptional points," *Nature*, vol. 537, no. 7618, p. 80, 2016.

[9] J. Hertzberg, T. Rocheleau, T. Ndukum, M. Savva, A. Clerk, and K. Schwab, "Back-action-evading measurements of nanomechanical motion," *Nature Physics*, vol. 6, no. 3, p. 213, 2010.

[10] C. Ockeloen-Korppi, E. Damskägg, J.-M. Pirkkalainen, A. Clerk, M. Woolley, and M. Sillanpää, "Quantum backaction evading measurement of collective mechanical modes," *Physical review letters*, vol. 117, no. 14, p. 140401, 2016.

[11] C. Dong, J. Zhang, V. Fiore, and H. Wang, "Optomechanically induced transparency and self-induced oscillations with bogoliubov mechanical modes," *Optica*, vol. 1, no. 6, pp. 425–428, 2014.

[12] A. Pontin, M. Bonaldi, A. Borrielli, L. Marconi, F. Marino, G. Pandraud, G. Prodi, P. Sarro, E. Serra, and F. Marin, "Dynamical two-mode squeezing of thermal fluctuations in a cavity optomechanical system," *Physical review letters*, vol. 116, no. 10, p. 103601, 2016.

[13] C. Dong, V. Fiore, M. C. Kuzyk, and H. Wang, "Optomechanical dark mode," *Science*, vol. 338, no. 6114, pp. 1609–1613, 2012.

[14] J. T. Hill, A. H. Safavi-Naeini, J. Chan, and O. Painter, "Coherent optical wavelength conversion via cavity optomechanics," *Nature communications*, vol. 3, p. 1196, 2012.

[15] Y. Liu, M. Davanço, V. Aksyuk, and K. Srinivasan, "Electromagnetically induced transparency and wideband wavelength conversion in silicon nitride microdisk optomechanical resonators," *Physical review letters*, vol. 110, no. 22, p. 223603, 2013.

[16] J. Bochmann, A. Vainsencher, D. D. Awschalom, and A. N. Cleland, "Nanomechanical coupling between microwave and optical photons," *Nature Physics*, vol. 9, no. 11, p. 712, 2013.

[17] R. W. Andrews, R. W. Peterson, T. P. Purdy, K. Cicak, R. W. Simmonds, C. A. Regal, and K. W. Lehnert, "Bidirectional and efficient conversion between microwave and optical light," *Nature Physics*, vol. 10, no. 4, p. 321, 2014.

[18] A. Shkarin, N. Flowers-Jacobs, S. Hoch, A. Kashkanova, C. Deutsch, J. Reichel, and J. Harris, "Optically mediated hybridization between two mechanical modes," *Physical review letters*, vol. 112, no. 1, p. 013602, 2014.

[19] R. Andrews, A. Reed, K. Cicak, J. Teufel, and K. Lehnert, "Quantum-enabled temporal and spectral mode conversion of microwave signals," *Nature communications*, vol. 6, p. 10021, 2015.

[20] F. Lecocq, J. B. Clark, R. W. Simmonds, J. Aumentado, and J. D. Teufel, "Mechanically mediated microwave frequency conversion in the quantum regime," *Physical review letters*, vol. 116, no. 4, p. 043601, 2016.

[21] K. C. Balram, M. I. Davanço, J. D. Song, and K. Srinivasan, "Coherent coupling between radiofrequency, optical and acoustic waves in piezo-optomechanical circuits," *Nature photonics*, vol. 10, no. 5, p. 346, 2016.

[22] M. J. Weaver, F. Buters, F. Luna, H. Eerkens, K. Heeck, S. Man, and D. Bouwmeester, "Coherent optomechanical state transfer between disparate mechanical resonators," *Nature communications*, vol. 8, no. 1, p. 824, 2017.

[23] M. C. Kuzyk and H. Wang, "Controlling multimode optomechanical interactions via interference," *Physical Review A*, vol. 96, no. 2, p. 023860, 2017.

[24] M. C. Kuzyk, S. J. van Enk, and H. Wang, "Generating robust optical entanglement in weak-coupling optomechanical systems," *Physical Review A*, vol. 88, no. 6, p. 062341, 2013.

[25] M. C. Kuzyk and H. Wang, "Phononic quantum networks of solid-state spins with alternating and frequency-selective waveguides," *arXiv preprint arXiv:1804.07862*, 2018.

[26] Y.-S. Park and H. Wang, "Resolved-sideband and cryogenic cooling of an optomechanical resonator," *Nature Physics*, vol. 5, no. 7, p. 489, 2009.

[27] Y.-D. Wang and A. A. Clerk, "Using interference for high fidelity quantum state transfer in optomechanics," *Physical review letters*, vol. 108, no. 15, p. 153603, 2012.

[28] L. Tian, "Adiabatic state conversion and pulse transmission in optomechanical systems," *Physical review letters*, vol. 108, no. 15, p. 153604, 2012.

[29] A. H. Safavi-Naeini and O. Painter, "Proposal for an optomechanical traveling wave phonon–photon translator," *New Journal of Physics*, vol. 13, no. 1, p. 013017, 2011.

[30] D. Chang, A. H. Safavi-Naeini, M. Hafezi, and O. Painter, "Slowing and stopping light using an optomechanical crystal array," *New Journal of Physics*, vol. 13, no. 2, p. 023003, 2011.

[31] J. Thompson, B. Zwickl, A. Jayich, F. Marquardt, S. Girvin, and J. Harris, "Strong dispersive coupling of a high-finesse cavity to a micromechanical membrane," *Nature*, vol. 452, no. 7183, p. 72, 2008.

[32] G. Anetsberger, O. Arcizet, Q. P. Unterreithmeier, R. Rivière, A. Schliesser, E. M. Weig, J. P. Kotthaus, and T. J. Kippenberg, "Near-field cavity optomechanics with nanomechanical oscillators," *Nature Physics*, vol. 5, no. 12, p. 909, 2009.

[33] P. Rabl, S. J. Kolkowitz, F. H. L. Koppens, J. G. E. Harris, P. Zoller, and M. D. Lukin, "A quantum spin transducer based on nanoelectromechanical resonator arrays," *NATURE PHYSICS*, vol. 6, pp. 602–608, AUG 2010.

[34] P. Treutlein, D. Hunger, S. Camerer, T. W. Haensch, and J. Reichel, "Bose-Einstein condensate coupled to a nanomechanical resonator on an atom chip," *PHYSICAL REVIEW LETTERS*, vol. 99, OCT 5 2007.

[35] S. Kolkowitz, A. C. B. Jayich, Q. P. Unterreithmeier, S. D. Bennett, P. Rabl, J. G. E. Harris, and M. D. Lukin, "Coherent Sensing of a Mechanical Resonator with a Single-Spin Qubit," *SCIENCE*, vol. 335, pp. 1603–1606, MAR 30 2012.

[36] H. Seok, L. Buchmann, E. Wright, and P. Meystre, "Multimode strong-coupling quantum optomechanics," *Physical Review A*, vol. 88, no. 6, p. 063850, 2013.

[37] L. Tian, "Robust photon entanglement via quantum interference in optomechanical interfaces," *Physical review letters*, vol. 110, no. 23, p. 233602, 2013.

[38] Y.-D. Wang and A. A. Clerk, "Reservoir-engineered entanglement in optomechanical systems," *Physical review letters*, vol. 110, no. 25, p. 253601, 2013.

[39] Y. Yanay, J. C. Sankey, and A. A. Clerk, "Quantum backaction and noise interference in asymmetric two-cavity optomechanical systems," *Physical Review A*, vol. 93, no. 6, p. 063809, 2016.

[40] Q. Lin, J. Rosenberg, D. Chang, R. Camacho, M. Eichenfield, K. J. Vahala, and O. Painter, "Coherent mixing of mechanical excitations in nano-optomechanical structures," *Nature Photonics*, vol. 4, no. 4, p. 236, 2010.

[41] F. Massel, S. U. Cho, J.-M. Pirkkalainen, P. J. Hakonen, T. T. Heikkilä, and M. A. Sillanpää, "Multimode circuit optomechanics near the quantum limit," *Nature communications*, vol. 3, p. 987, 2012.

[42] N. Spethmann, J. Kohler, S. Schreppler, L. Buchmann, and D. M. Stamper-Kurn, "Cavity-mediated coupling of mechanical oscillators limited by quantum back-action," *Nature Physics*, vol. 12, no. 1, p. 27, 2016.

[43] G. Bahl, M. Tomes, F. Marquardt, and T. Carmon, "Observation of spontaneous brillouin cooling," *Nature Physics*, vol. 8, no. 3, p. 203, 2012.

[44] J. Kim, M. C. Kuzyk, K. Han, H. Wang, and G. Bahl, "Non-reciprocal brillouin scattering induced transparency," *Nature Physics*, vol. 11, no. 3, p. 275, 2015.

[45] C.-H. Dong, Z. Shen, C.-L. Zou, Y.-L. Zhang, W. Fu, and G.-C. Guo, "Brillouin-scattering-induced transparency and non-reciprocal light storage," *Nature communications*, vol. 6, p. 6193, 2015.

[46] J. Zhang, K. Peng, and S. L. Braunstein, "Quantum-state transfer from light to macroscopic oscillators," *Physical Review A*, vol. 68, no. 1, p. 013808, 2003.

[47] V. Fiore, Y. Yang, M. C. Kuzyk, R. Barbour, L. Tian, and H. Wang, "Storing optical information as a mechanical excitation in a silica optomechanical resonator," *Physical review letters*, vol. 107, no. 13, p. 133601, 2011.

[48] C. Dong, V. Fiore, M. C. Kuzyk, and H. Wang, "Transient optomechanically induced transparency in a silica microsphere," *Physical Review A*, vol. 87, no. 5, p. 055802, 2013.

[49] G. Agarwal and S. Huang, "Electromagnetically induced transparency in mechanical effects of light," *Physical Review A*, vol. 81, no. 4, p. 041803, 2010.

[50] M. Aspelmeyer, T. J. Kippenberg, and F. Marquardt, "Cavity optomechanics," *Reviews of Modern Physics*, vol. 86, no. 4, p. 1391, 2014.

[51] S. Barzanjeh, M. Abdi, G. J. Milburn, P. Tombesi, and D. Vitali, "Reversible optical-to-microwave quantum interface," *Physical Review Letters*, vol. 109, no. 13, p. 130503, 2012.

[52] S. Barzanjeh, D. Vitali, P. Tombesi, and G. Milburn, "Entangling optical and microwave cavity modes by means of a nanomechanical resonator," *Physical Review A*, vol. 84, no. 4, p. 042342, 2011.

[53] S. Gröblacher, K. Hammerer, M. R. Vanner, and M. Aspelmeyer, "Observation of strong coupling between a micromechanical resonator and an optical cavity field," *Nature*, vol. 460, no. 7256, pp. 724–727, 2009.

[54] J. Teufel, D. Li, M. Allman, K. Cicak, A. Sirois, J. Whittaker, and R. Simmonds, "Circuit cavity electromechanics in the strong-coupling regime," *Nature*, vol. 471, no. 7337, pp. 204–208, 2011.

[55] E. Verhagen, S. Deléglise, S. Weis, A. Schliesser, and T. J. Kippenberg, "Quantum-coherent coupling of a mechanical oscillator to an optical cavity mode," *Nature*, vol. 482, no. 7383, pp. 63–67, 2012.

[56] A. Sørensen and K. Mølmer, "Quantum computation with ions in thermal motion," *Physical Review Letters*, vol. 82, no. 9, pp. 1971–1974, 1999.

[57] C. Sackett, D. Kielpinski, B. King, C. Langer, V. Meyer, C. Myatt, M. Rowe, Q. Turchette, W. Itano, D. Wineland, *et al.*, "Experimental entanglement of four particles," *Nature*, vol. 404, no. 6775, pp. 256–259, 2000.

[58] A. Sørensen and K. Mølmer, "Entanglement and quantum computation with ions in thermal motion," *Physical Review A*, vol. 62, no. 2, p. 22311, 2000.

[59] Y. Liu, M. Davanço, V. Aksyuk, and K. Srinivasan, "Electromagnetically induced transparency and wideband wavelength conversion in silicon nitride microdisk optomechanical resonators," *Physical Review Letters*, vol. 110, p. 223603, May 2013.

[60] E. Verhagen, S. Deléglise, S. Weis, A. Schliesser, and T. J. Kippenberg, "Quantum-coherent coupling of a mechanical oscillator to an optical cavity mode," *Nature*, vol. 482, no. 7383, p. 63, 2012.

[61] V. Fiore, C. Dong, M. C. Kuzyk, and H. Wang, "Optomechanical light storage in a silica microresonator," *Physical Review A*, vol. 87, no. 2, p. 023812, 2013.

[62] T. Palomaki, J. Harlow, J. Teufel, R. Simmonds, and K. Lehnert, "Coherent state transfer between itinerant microwave fields and a mechanical oscillator," *Nature*, vol. 495, no. 7440, pp. 210–214, 2013.

[63] S. Weis, R. Rivière, S. Deléglise, E. Gavartin, O. Arcizet, A. Schliesser, and T. J. Kippenberg, "Optomechanically induced transparency," *Science*, vol. 330, no. 6010, pp. 1520–1523, 2010.

[64] A. H. Safavi-Naeini, T. M. Alegre, J. Chan, M. Eichenfield, M. Winger, Q. Lin, J. T. Hill, D. Chang, and O. Painter, "Electromagnetically induced transparency and slow light with optomechanics," *Nature*, vol. 472, no. 7341, pp. 69–73, 2011.

[65] M. Karuza, C. Biancofiore, M. Bawaj, C. Molinelli, M. Galassi, R. Natali, P. Tombesi, G. Di Giuseppe, and D. Vitali, "Optomechanically induced transparency in a membrane-in-the-middle setup at room temperature," *Physical Review A*, vol. 88, no. 1, p. 013804, 2013.

[66] S. Mancini, V. Giovannetti, D. Vitali, and P. Tombesi, "Entangling macroscopic oscillators exploiting radiation pressure," *Physical Review Letters*, vol. 88, no. 12, p. 120401, 2002.

[67] M. Paternostro, D. Vitali, S. Gigan, M. Kim, C. Brukner, J. Eisert, and M. Aspelmeyer, "Creating and probing multipartite macroscopic entanglement with light," *Physical Review Letters*, vol. 99, no. 25, p. 250401, 2007.

[68] S. G. Hofer, W. Wieczorek, M. Aspelmeyer, and K. Hammerer, "Quantum entanglement and teleportation in pulsed cavity optomechanics," *Physical Review A*, vol. 84, no. 5, p. 052327, 2011.

[69] H. Tan, G. Li, and P. Meystre, "Dissipation-driven two-mode mechanical squeezed states in optomechanical systems," *Physical Review A*, vol. 87, p. 033829, 2013.

[70] M. J. Woolley and C. A. A, "Two-mode back-action-evading measurements in cavity optomechanics," *Physical Review A*, vol. 87, no. 6, p. 063846, 2013.

[71] A. Furusawa, J. L. Sørensen, S. L. Braunstein, C. A. Fuchs, H. J. Kimble, and E. S. Polzik, "Unconditional quantum teleportation," *Science*, vol. 282, no. 5389, pp. 706–709, 1998.

[72] S. Pirandola, D. Vitali, P. Tombesi, and S. Lloyd, "Macroscopic entanglement by entanglement swapping," *arXiv preprint quant-ph/0509119*, 2005.

[73] K. Børkje, A. Nunnenkamp, and S. Girvin, "Proposal for entangling remote micromechanical oscillators via optical measurements," *Physical review letters*, vol. 107, no. 12, p. 123601, 2011.

[74] G. J. Milburn, "Simulating nonlinear spin models in an ion trap," *arXiv preprint quant-ph/9908037*, 1999.

[75] H.-K. Li, X.-X. Ren, Y.-C. Liu, and Y.-F. Xiao, "Effective photon-photon interactions in largely detuned optomechanics," *arXiv preprint arXiv:1306.1035*, 2013.

[76] C. Genes, A. Mari, P. Tombesi, and D. Vitali, "Robust entanglement of a micromechanical resonator with output optical fields," *Physical Review A*, vol. 78, no. 3, p. 032316, 2008.

[77] M. B. Plenio, "Logarithmic negativity: A full entanglement monotone that is not convex," *Physical Review Letters*, vol. 95, no. 9, p. 090503, 2005.

[78] G. Vidal and R. F. Werner, "A computable measure of entanglement," *arXiv preprint quant-ph/0102117*, 2001.

[79] K. Blow, R. Loudon, S. J. Phoenix, and T. Shepherd, "Continuum fields in quantum optics," *Physical Review A*, vol. 42, no. 7, p. 4102, 1990.

[80] H. J. Kimble, "The quantum internet," *Nature*, vol. 453, no. 7198, p. 1023, 2008.

[81] K. Hammerer, A. S. Sørensen, and E. S. Polzik, "Quantum interface between light and atomic ensembles," *Reviews of Modern Physics*, vol. 82, no. 2, p. 1041, 2010.

[82] L.-M. Duan and C. Monroe, "Colloquium: Quantum networks with trapped ions," *Reviews of Modern Physics*, vol. 82, no. 2, p. 1209, 2010.

[83] T. Northup and R. Blatt, "Quantum information transfer using photons," *Nature Photonics*, vol. 8, no. 5, p. 356, 2014.

[84] A. Reiserer and G. Rempe, "Cavity-based quantum networks with single atoms and optical photons," *Reviews of Modern Physics*, vol. 87, no. 4, p. 1379, 2015.

[85] S. Habraken, K. Stannigel, M. D. Lukin, P. Zoller, and P. Rabl, "Continuous mode cooling and phonon routers for phononic quantum networks," *New Journal of Physics*, vol. 14, no. 11, p. 115004, 2012.

[86] M. V. Gustafsson, T. Aref, A. F. Kockum, M. K. Ekström, G. Johansson, and P. Delsing, "Propagating phonons coupled to an artificial atom," *Science*, vol. 346, no. 6206, pp. 207–211, 2014.

[87] M. J. Schütz, "Universal quantum transducers based on surface acoustic waves," in *Quantum Dots for Quantum Information Processing: Controlling and Exploiting the Quantum Dot Environment*, pp. 143–196, Springer, 2017.

[88] J. I. Cirac, P. Zoller, H. J. Kimble, and H. Mabuchi, "Quantum state transfer and entanglement distribution among distant nodes in a quantum network," *Physical Review Letters*, vol. 78, no. 16, p. 3221, 1997.

[89] H. Carmichael, "Quantum trajectory theory for cascaded open systems," *Physical review letters*, vol. 70, no. 15, p. 2273, 1993.

[90] B. Vermersch, P.-O. Guimond, H. Pichler, and P. Zoller, "Quantum state transfer via noisy photonic and phononic waveguides," *Physical review letters*, vol. 118, no. 13, p. 133601, 2017.

[91] Z.-L. Xiang, M. Zhang, L. Jiang, and P. Rabl, "Intracity quantum communication via thermal microwave networks," *Physical Review X*, vol. 7, no. 1, p. 011035, 2017.

[92] K. Y. Bliokh, F. Rodríguez-Fortuño, F. Nori, and A. V. Zayats, "Spin–orbit interactions of light," *Nature Photonics*, vol. 9, no. 12, p. 796, 2015.

[93] P. Lodahl, S. Mahmoodian, S. Stobbe, A. Rauschenbeutel, P. Schneeweiss, J. Volz, H. Pichler, and P. Zoller, "Chiral quantum optics," *Nature*, vol. 541, no. 7638, p. 473, 2017.

[94] R. Mitsch, C. Sayrin, B. Albrecht, P. Schneeweiss, and A. Rauschenbeutel, "Quantum state-controlled directional spontaneous emission of photons into a nanophotonic waveguide," *Nature communications*, vol. 5, p. 5713, 2014.

[95] I. Söllner, S. Mahmoodian, S. L. Hansen, L. Midolo, A. Javadi, G. Kiršanskė, T. Pregnolato, H. El-Ella, E. H. Lee, J. D. Song, *et al.*, "Deterministic photon–emitter coupling in chiral photonic circuits," *Nature nanotechnology*, vol. 10, no. 9, pp. nnano–2015, 2015.

[96] M.-A. Lemonde, S. Meesala, A. Sipahigil, M. Schuetz, M. Lukin, M. Loncar, and P. Rabl, "Phonon networks with siv centers in diamond waveguides," *arXiv preprint arXiv:1801.01904*, 2018.

[97] C. Monroe and J. Kim, "Scaling the ion trap quantum processor," *Science*, vol. 339, no. 6124, pp. 1164–1169, 2013.

[98] D. A. Golter, T. Oo, M. Amezcua, K. A. Stewart, and H. Wang, "Optomechanical quantum control of a nitrogen-vacancy center in diamond," *Physical review letters*, vol. 116, no. 14, p. 143602, 2016.

[99] D. Hatanaka, I. Mahboob, K. Onomitsu, and H. Yamaguchi, "Phonon waveguides for electromechanical circuits," *Nature nanotechnology*, vol. 9, no. 7, p. 520, 2014.

[100] A. Sipahigil, R. Evans, D. Sukachev, M. Burek, J. Borregaard, M. Bhaskar, C. Nguyen, J. Pacheco, H. Atikian, C. Meuwly, *et al.*, "An integrated diamond nanophotonics platform for quantum optical networks," *Science*, p. aah6875, 2016.

[101] M. J. Burek, J. D. Cohen, S. M. Meenehan, N. El-Sawah, C. Chia, T. Ruelle, S. Meesala, J. Rochman, H. A. Atikian, M. Markham, *et al.*, "Diamond optomechanical crystals," *Optica*, vol. 3, no. 12, pp. 1404–1411, 2016.

[102] N. H. Wan, S. Mouradian, and D. Englund, "Two-dimensional photonic crystal slab nanocavities on bulk single-crystal diamond," *Applied Physics Letters*, vol. 112, no. 14, p. 141102, 2018.

[103] M. W. Doherty, N. B. Manson, P. Delaney, F. Jelezko, J. Wrachtrup, and L. C. Hollenberg, "The nitrogen-vacancy colour centre in diamond," *Physics Reports*, vol. 528, no. 1, pp. 1–45, 2013.

[104] D. D. Awschalom, L. C. Bassett, A. S. Dzurak, E. L. Hu, and J. R. Petta, "Quantum spintronics: engineering and manipulating atom-like spins in semiconductors," *Science*, vol. 339, no. 6124, pp. 1174–1179, 2013.

[105] L. Childress, R. Walsworth, and M. Lukin, "Atom-like crystal defects," *Physics Today*, vol. 67, no. 10, p. 38, 2014.

[106] F. Jelezko, T. Gaebel, I. Popa, A. Gruber, and J. Wrachtrup, "Observation of coherent oscillations in a single electron spin," *Physical review letters*, vol. 92, no. 7, p. 076401, 2004.

[107] L. Childress, M. G. Dutt, J. Taylor, A. Zibrov, F. Jelezko, J. Wrachtrup, P. Hemmer, and M. Lukin, "Coherent dynamics of coupled electron and nuclear spin qubits in diamond," *Science*, vol. 314, no. 5797, pp. 281–285, 2006.

[108] G. Fuchs, V. Dobrovitski, D. Toyli, F. Heremans, and D. Awschalom, "Gigahertz dynamics of a strongly driven single quantum spin," *Science*, vol. 326, no. 5959, pp. 1520–1522, 2009.

[109] G. De Lange, Z. Wang, D. Riste, V. Dobrovitski, and R. Hanson, "Universal dynamical decoupling of a single solid-state spin from a spin bath," *Science*, vol. 330, no. 6000, pp. 60–63, 2010.

[110] C. G. Yale, B. B. Buckley, D. J. Christle, G. Burkard, F. J. Heremans, L. C. Bassett, and D. D. Awschalom, "All-optical control of a solid-state spin using coherent dark states," *Proceedings of the National Academy of Sciences*, vol. 110, no. 19, pp. 7595–7600, 2013.

[111] D. A. Golter and H. Wang, "Optically driven rabi oscillations and adiabatic passage of single electron spins in diamond," *Physical review letters*, vol. 112, no. 11, p. 116403, 2014.

[112] L. C. Bassett, F. J. Heremans, D. J. Christle, C. G. Yale, G. Burkard, B. B. Buckley, and D. D. Awschalom, "Ultrafast optical control of orbital and spin dynamics in a solid-state defect," *Science*, vol. 345, no. 6202, pp. 1333–1337, 2014.

[113] S. D. Barrett and P. Kok, "Efficient high-fidelity quantum computation using matter qubits and linear optics," *Physical Review A*, vol. 71, no. 6, p. 060310, 2005.

[114] Q. Chen, W. Yang, M. Feng, and J. Du, "Entangling separate nitrogen-vacancy centers in a scalable fashion via coupling to microtoroidal resonators," *Physical Review A*, vol. 83, no. 5, p. 054305, 2011.

[115] K. Nemoto, M. Trupke, S. J. Devitt, A. M. Stephens, B. Scharfenberger, K. Buczak, T. Nöbauer, M. S. Everitt, J. Schmiedmayer, and W. J. Munro, "Photonic architecture for scalable quantum information processing in diamond," *Physical Review X*, vol. 4, no. 3, p. 031022, 2014.

[116] A. Sipahigil, K. D. Jahnke, L. J. Rogers, T. Teraji, J. Isoya, A. S. Zibrov, F. Jelezko, and M. D. Lukin, "Indistinguishable photons from separated silicon-vacancy centers in diamond," *Physical review letters*, vol. 113, no. 11, p. 113602, 2014.

[117] L. J. Rogers, K. D. Jahnke, T. Teraji, L. Marseglia, C. Müller, B. Naydenov, H. Schauffert, C. Kranz, J. Isoya, L. P. McGuinness, *et al.*, "Multiple intrinsically identical single-photon emitters in the solid state," *Nature communications*, vol. 5, p. 4739, 2014.

[118] M. K. Bhaskar, D. D. Sukachev, A. Sipahigil, R. E. Evans, M. J. Burek, C. T. Nguyen, L. J. Rogers, P. Siyushev, M. H. Metsch, H. Park, *et al.*, "Quantum nonlinear optics with a germanium-vacancy color center in a nanoscale diamond waveguide," *Physical review letters*, vol. 118, no. 22, p. 223603, 2017.

[119] P. Siyushev, M. H. Metsch, A. Ijaz, J. M. Binder, M. K. Bhaskar, D. D. Sukachev, A. Sipahigil, R. E. Evans, C. T. Nguyen, M. D. Lukin, *et al.*, "Optical and microwave control of germanium-vacancy center spins in diamond," *Physical Review B*, vol. 96, no. 8, p. 081201, 2017.

[120] Y. Chu, N. P. de Leon, B. J. Shields, B. Hausmann, R. Evans, E. Togan, M. J. Burek, M. Markham, A. Stacey, A. S. Zibrov, *et al.*, "Coherent optical transitions in implanted nitrogen vacancy centers," *Nano letters*, vol. 14, no. 4, pp. 1982–1986, 2014.

[121] R. E. Evans, A. Sipahigil, D. D. Sukachev, A. S. Zibrov, and M. D. Lukin, "Narrow-linewidth homogeneous optical emitters in diamond nanostructures via silicon ion implantation," *Physical Review Applied*, vol. 5, no. 4, p. 044010, 2016.

[122] O. Arcizet, V. Jacques, A. Siria, P. Poncharal, P. Vincent, and S. Seidelin, "A single nitrogen-vacancy defect coupled to a nanomechanical oscillator," *Nature Physics*, vol. 7, no. 11, p. 879, 2011.

[123] E. MacQuarrie, T. Gosavi, N. Jungwirth, S. Bhave, and G. Fuchs, "Mechanical spin control of nitrogen-vacancy centers in diamond," *Physical review letters*, vol. 111, no. 22, p. 227602, 2013.

[124] J. Teissier, A. Barfuss, P. Appel, E. Neu, and P. Maletinsky, "Strain coupling of a nitrogen-vacancy center spin to a diamond mechanical oscillator," *Phys. Rev. Lett.*, vol. 113, p. 020503, 2014.

[125] P. Ovartchaiyapong, K. W. Lee, B. A. Myers, and A. C. B. Jayich, "Dynamic strain-mediated coupling of a single diamond spin to a mechanical resonator," *Nature communications*, vol. 5, p. 4429, 2014.

[126] E. MacQuarrie, T. Gosavi, S. Bhave, and G. Fuchs, "Continuous dynamical decoupling of a single diamond nitrogen-vacancy center spin with a mechanical resonator," *Physical Review B*, vol. 92, no. 22, p. 224419, 2015.

[127] A. Barfuss, J. Teissier, E. Neu, A. Nunnenkamp, and P. Maletinsky, "Strong mechanical driving of a single electron spin," *Nature Physics*, vol. 11, no. 10, p. 820, 2015.

[128] E. MacQuarrie, T. Gosavi, A. Moehle, N. Jungwirth, S. Bhave, and G. Fuchs, "Coherent control of a nitrogen-vacancy center spin ensemble with a diamond mechanical resonator," *Optica*, vol. 2, no. 3, pp. 233–238, 2015.

[129] S. Meesala, Y.-I. Sohn, H. A. Atikian, S. Kim, M. J. Burek, J. T. Choy, and M. Lončar, "Enhanced strain coupling of nitrogen-vacancy spins to nanoscale diamond cantilevers," *Physical Review Applied*, vol. 5, no. 3, p. 034010, 2016.

[130] D. A. Golter, T. Oo, M. Amezcua, I. Lekavicius, K. A. Stewart, and H. Wang, "Coupling a surface acoustic wave to an electron spin in diamond via a dark state," *Physical Review X*, vol. 6, no. 4, p. 041060, 2016.

[131] K. W. Lee, D. Lee, P. Ovartchaiyapong, J. Minguzzi, J. R. Maze, and A. C. B. Jayich, "Strain coupling of a mechanical resonator to a single quantum emitter in diamond," *Physical Review Applied*, vol. 6, no. 3, p. 034005, 2016.

[132] K. Kepesidis, S. Bennett, S. Portolan, M. D. Lukin, and P. Rabl, "Phonon cooling and lasing with nitrogen-vacancy centers in diamond," *Physical Review B*, vol. 88, no. 6, p. 064105, 2013.

[133] A. Albrecht, A. Retzker, F. Jelezko, and M. B. Plenio, "Coupling of nitrogen vacancy centres in nanodiamonds by means of phonons," *New Journal of Physics*, vol. 15, no. 8, p. 083014, 2013.

[134] S. Meesala, Y.-I. Sohn, B. Pingault, L. Shao, H. A. Atikian, J. Holzgrafe, M. Gundogan, C. Stavrakas, A. Sipahigil, C. Chia, *et al.*, "Strain engineering of the silicon-vacancy center in diamond," *arXiv preprint arXiv:1801.09833*, 2018.

[135] E. Togan, Y. Chu, A. Trifonov, L. Jiang, J. Maze, L. Childress, M. G. Dutt, A. S. Sørensen, P. Hemmer, A. S. Zibrov, *et al.*, "Quantum entanglement between an optical photon and a solid-state spin qubit," *Nature*, vol. 466, no. 7307, p. 730, 2010.

[136] X. Chen, I. Lizuain, A. Ruschhaupt, D. Guéry-Odelin, and J. Muga, "Shortcut to adiabatic passage in two-and three-level atoms," *Physical review letters*, vol. 105, no. 12, p. 123003, 2010.

[137] B. B. Zhou, A. Baksic, H. Ribeiro, C. G. Yale, F. J. Heremans, P. C. Jerger, A. Auer, G. Burkard, A. A. Clerk, and D. D. Awschalom, "Accelerated quantum control using superadiabatic dynamics in a solid-state lambda system," *Nature Physics*, vol. 13, no. 4, p. 330, 2017.

[138] H. Ribeiro, A. Baksic, and A. A. Clerk, "Systematic magnus-based approach for suppressing leakage and nonadiabatic errors in quantum dynamics," *Physical Review X*, vol. 7, no. 1, p. 011021, 2017.

[139] J. Chan, T. M. Alegre, A. H. Safavi-Naeini, J. T. Hill, A. Krause, S. Gröblacher, M. Aspelmeyer, and O. Painter, "Laser cooling of a nanomechanical oscillator into its quantum ground state," *Nature*, vol. 478, no. 7367, p. 89, 2011.

[140] P.-L. Yu, K. Cicak, N. Kampel, Y. Tsaturyan, T. Purdy, R. Simmonds, and C. Regal, "A phononic bandgap shield for high-q membrane microresonators," *Applied Physics Letters*, vol. 104, no. 2, p. 023510, 2014.

[141] R. N. Patel, Z. Wang, W. Jiang, C. J. Sarabalis, J. T. Hill, and A. H. Safavi-Naeini, "A single-mode phononic wire," *arXiv preprint arXiv:1711.00847*, 2017.

[142] Y. Tsaturyan, A. Barg, E. S. Polzik, and A. Schliesser, "Ultracoherent nanomechanical resonators via soft clamping and dissipation dilution," *Nature nanotechnology*, vol. 12, no. 8, p. 776, 2017.

[143] K. Stannigel, P. Rabl, A. S. Sørensen, P. Zoller, and M. D. Lukin, "Optomechanical transducers for long-distance quantum communication," *Physical review letters*, vol. 105, no. 22, p. 220501, 2010.

[144] L. Tian and H. Wang, "Optical wavelength conversion of quantum states with optomechanics," *Physical Review A*, vol. 82, no. 5, p. 053806, 2010.

[145] C. Regal and K. Lehnert, "From cavity electromechanics to cavity optomechanics," in *Journal of Physics: Conference Series*, vol. 264, p. 012025, IOP Publishing, 2011.

[146] C. Dong, Y. Wang, and H. Wang, "Optomechanical interfaces for hybrid quantum networks," *National Science Review*, vol. 2, no. 4, pp. 510–519, 2015.

[147] Y.-D. Wang and A. A. Clerk, "Using dark modes for high-fidelity optomechanical quantum state transfer," *New Journal of Physics*, vol. 14, no. 10, p. 105010, 2012.

[148] A. Uhlmann, "The transition probability in the state space of a-algebra," *Reports on Mathematical Physics*, vol. 9, no. 2, pp. 273–279, 1976.

[149] G. Balasubramanian, P. Neumann, D. Twitchen, M. Markham, R. Kolesov, N. Mizuochi, J. Isoya, J. Achard, J. Beck, J. Tissler, *et al.*, "Ultralong spin coherence time in isotopically engineered diamond," *Nature materials*, vol. 8, no. 5, p. 383, 2009.

[150] D. A. Golter, T. K. Baldwin, and H. Wang, "Protecting a solid-state spin from decoherence using dressed spin states," *Physical review letters*, vol. 113, no. 23, p. 237601, 2014.

[151] X. Xu, Z. Wang, C. Duan, P. Huang, P. Wang, Y. Wang, N. Xu, X. Kong, F. Shi, X. Rong, *et al.*, "Coherence-protected quantum gate by continuous dynamical decoupling in diamond," *Physical review letters*, vol. 109, no. 7, p. 070502, 2012.

[152] W. F. Koehl, B. B. Buckley, F. J. Heremans, G. Calusine, and D. D. Awschalom, "Room temperature coherent control of defect spin qubits in silicon carbide," *Nature*, vol. 479, no. 7371, p. 84, 2011.

[153] A. G. Fowler, A. M. Stephens, and P. Groszkowski, "High-threshold universal quantum computation on the surface code," *Physical Review A*, vol. 80, no. 5, p. 052312, 2009.

[154] R. Simon, "Peres-horodecki separability criterion for continuous variable systems," *Physical Review Letters*, vol. 84, no. 12, p. 2726, 2000.